Adaptive Control of Electronic Excitation Utilizing Ultrafast Laser Pulses

Dissertation zur Erlangung des
naturwissenschaftlichen Doktorgrades
der Bayerischen Julius-Maximilians-Universität
Würzburg

vorgelegt von
Evangelos Papastathopoulos
aus Athen

Würzburg 2005

Eingereicht am:
bei der Fakultät für Physik und Astronomie

1. Gutachter: Prof. Dr. G. Gerber
2. Gutachter: Prof. Dr. V. Engel
der Dissertation

1. Prüfer: Prof. Dr. G. Gerber
2. Prüfer: Prof. Dr. H. Hinrichsen
3. Prüfer: Prof. Dr. V. Engel
der mündlichen Prüfung

Tag der mündlichen Prüfung: 10.03.2005

Σ΄ ένα χωριό γεννήθηκα οπως γεννιόνται όλοι
και δάσκαλος με βάφτισε και μ΄ έβγαλε Μανώλη.
Η Παναγιά που βρέθηκε σ ενα κτήμα μεγάλο
και το χωριό που κάθομαι ελέγεται Μουντάδο.

Το 1822 η ευσεβής καλόγρια, αγία Πελαγία
είδε σπουδαίο όνειρο στον ύπνο της την Παναγία.
Οπως και της υπέδειξε στου Δοξαρά το κτήμα
εκεί εικόνα της να βρεί, να χτίσει εκκλησία.
Όπου πραγματοποιήθηκαν και θαύματα μεγάλα
και έρχονται και προσκυνούν απ΄ όλη την Ελλάδα.

Και τώρα αγαπητοί μου μάθετε για το ποίημα της Έλλης
που το βγάλαμε 15 χρονών παιδιά.

Κλάψτε το Έλληνες κλάψτε το, το Έλλη το καράβι
στην Τήνο το τορπίλισαν έξω απο το λιμάνι.
Της Παναγίας το πρωί έφτασε στα νερά της Τήνου
όμως αμέσως σήκωσε σημαία του κινδύνου.
Οι ναύτες ετοιμάζονταν να βάλουν την στολή τους
να βγούνε εις την τελετή για μιαν εκτιμησή τους.
Κι άν η τορπίλη έπεσε μες στα πετρέλαιά του
μεγάλο φόβο είχανε τα πυρομαχικά του.
Φοβήθηκαν την έκρηξη που θα ΄καμε το Έλλη
κι αμέσως πήραν τα βουνά οι Τηνιακοί και ξένοι.
Το Έλλη θα ξαναγενεί χαρούμενη η μέρα
θα στήσει στο κατάρτι του Ελληνική σημαία.

Ο Χίτλερ πονηρεύτηκε τον κόσμο να πατήσει
μα μόνος τιμωρήθηκε να παει ν΄αυτοκτονήσει.
Ο Μουσολίνι νόμισε πως είναι μακαρόνια
γι΄ αυτό τον κυνηγήσαμε στο Μπόγραδετς ακόμα.

Μουντάδος, Σεπτέμβρης 2004

dedicated to my sister Joanna

List of Publications

Parts of this work have been published in the following references:

T. Brixner, C. Dietl, G. Kramper, P.Niklaus, E. Papastathopoulos, T. Pfeifer, R. Selle, G. Vogt, D. Walter, C. Winterfeldt and G. Gerber,
Adaptive Femtosecond Quantum Control,
Ultrafast Optics IV, Springer-Verlag Eds. F. Krausz, G. Korn and P. Corkum (2003).

C. Dietl, E. Papastathopoulos and G. Gerber,
Femtosecond Photoelectron Spectroscopy of Trans -Stilbene,
Femtochemistry and Femtobiology Elsevier B.V., Eds. M.M. Martin and J.T. Hynes 41–44 (2004).

R. Improta,F. Santoro,C. Dietl,E. Papastathopoulos, G. Gerber,
Time dependent DFT investigation on the two lowest B-1(u) states of the trans isomer of stilbene and stiff-stilbenes,
Chem. Phys. Lett. **387**, 509–516 (2004).

C. Dietl, E. Papastathopoulos, P. Niklaus, R. Improta, F. Santoro and G. Gerber,
Femtosecond photoelectron spectroscopy of trans-stilbene above the reaction barrier,
accepted by Chem. Phys.

E. Papastathopoulos, M. Strehle and G. Gerber,
Optimal control of femtosecond electronic excitation in the atomic continuum,
submitted to Chem. Phys. Lett.

E. Papastathopoulos, M. Strehle and G. Gerber,
Adaptive optimization of multiphoton ionization: Towards solving the problem of inversion,
submitted to App. Phys.B

Contents

1 Introduction

The subject of this thesis is the interaction of isolated atoms and molecules with pulses of laser radiation. The original idea of using pulsed light sources to study dynamical molecular processes was first experimentally realized by R. Norrish and G. Porter in 1950 [1]. They used flash lamps in order to study molecules with lifetimes in the mili- and microsecond timescale that had never been experimentally studied before. In the years that followed, the technological "Holy Grail" has been the development of light sources of even shorter pulse duration which would eventually offer better resolution in this kind of time-resolved measurements. In this quest, a great breakthrough has been the development of the CPM-Laser (1981) [2] and the Ti:Sa-Laser (1991) [3]. These technologies offered a handy system to the disposal of the scientific community which made possible to expand the time resolution of the spectroscopic studies to the femtosecond (10^{-15} seconds) timescale [4–6]. With the emerging technique of femtosecond spectroscopy experiments can be performed in the time scale where molecular processes, like intramolecular vibrations, isomerization reactions, cleavage and forming of molecular bonds, actually take place. The so-called field of Femtochemistry [7, 8] reached a high point in 1999 with the nomination of the Nobel Prize in Chemistry to Ahmed H. Zewail "For his studies of the transition states of chemical reactions using femtosecond spectroscopy". To a great extent in femtosecond experiments the "Pump-Probe" scheme is being used, where the atomic or molecular system of interest is first excited by a laser pulse (pump pulse) to an intermediate non stationary (transition) quantum state, the dynamic of which is to be investigated. The corresponding time evolution of this state is then followed by means of a second laser pulse (probe pulse), the time delay of which can be varied in respect to the pump pulse. The detection of the intermediate state, as well of products, can be realized by means of a wide variety of spectroscopical techniques. The pump-probe scheme can be viewed as an ultrafast analog of the stroboscopic method established by H. E. Edgerton [9] in 1931.

These femtosecond techniques can be used not only to analyse chemical reactions,

but also to control reactions and competing processes. It is possible to selectively excite
and prepare a desired quantum state by appropriately choosing the delay time between
the pump- and probe- pulses. Such a two-pulse control scheme was experimentally real-
ized in 1991 by G. Gerber and T. Baumert [10] in the femtosecond laser excitation of
sodium dimers, where by appropriately delaying the probe- with respect to the pump-
pulse, the molecular fragmentation could be selectively enhanced or suppressed in a
multi-photon ionization scheme. The dream of using laser radiation to control chemical
reaction goes back to more than half a century ago, when among others the idea of
selective bond breaking by tuning the laser frequency was introduced. The major prob-
lem that limited the success of this method was that the energy that initially excites
the desired reaction mode is very fast redistributed into other modes (Intramolecular-
Vibrational-Redistribution [11] IVR) of the system. With the prior laser technologies,
which delivered relatively long laser pulses, the excitation of a specific mode could not
be selective enough. From the experimental point of view the development of femtosec-
ond laser systems offered a unique solution to this problem, since their pulse duration
overpasses the speed at which IVR takes place.

In the pump-probe scheme, the laser fields, used to control, are generally a sequence
of laser pulses with a simple gaussian-like time profile. Thinking in terms of finding a
laser field that could most effectively serve the purpose of selective quantum control, the
use of such pulse sequences is probably a rather limited choice. The idea of controlling
a quantum system ranges beyond than just influencing the excitation between only two
quantum states. It often requires the precise intervention in complex excitation schemes,
involving a wide diversity of quantum states. This purpose is rather served by using laser
fields with considerably more complex structure than gaussian-like pulses. In the mean
time, the generation of such complex laser fields was made possible by means of mod-
ern pulse shaping techniques [12]. The possibility of manipulating the amplitude and
phase as well as the polarization [13] of the laser pulses and hence generating arbitrarily
shaped laser pulses has opened up new prospects in the field of "femtoscience". This
technological development has been accompanied by the elaboration of appropriate sim-
ulation methods which in some cases can provide a theoretical calculation of the required
control laser fields [14]. However, it is often the case that these calculated laser fields
comprise just approximations of the complex modulated laser fields actually required
in the control experiments. It is nevertheless possible to define these complex control
laser pulses with an experimental method. It involves the shaping of the femtosecond
pulses by an optimization algorithm in a *closed loop* configuration. The algorithm can

optimize a given photoreaction pathway in an iterative manner by using direct feedback from the experiment [15, 16]. In the past years this adaptive optimization scheme was employed in our group [17, 18] among others to control the light-induced dissociation of organometallic compounds [19, 20]. Other experiments in this direction prove the applicability of this novel scheme in technical [21, 22] as well as in physical [23, 24] applications. In the present work, the method of adaptive femtosecond laser control has been applied to control experiments that involve a diversity of quantum systems, starting from a relatively simple atomic system and eventually advancing to more complex molecular systems. The order at which the scientific results are to be presented follows the increasing size as well as the complexity of the investigated systems. The outline of this thesis is then given as follows.

In Chapter 2, the theoretical background of femtosecond laser pulses is described, as well as the basic phenomena governing their interaction with atomic and molecular systems. Also, a short survey over elementary schemes of laser quantum control is presented. After that, the experimental realization of these concepts is described in chapter 3, where particular interest is given to the setups for generating and characterizing modulated laser pulses in the ultraviolet spectral region as well as to the "magnetic bottle" electron spectrometer. Both setups have been developed especially for the purposes of the experiments of this thesis and constitute part of the up-to-the-minute technological development in our lab.

In Chapter 4, the method of adaptive optimization is applied to the study of multi-photon ionization of atomic calcium. In many optimization experiments, especially the ones involving large molecules, the control has been realized eventhough the lack of knowledge, concerning the microscopic processes involved. The information about the photo induced interactions is encoded inside the optimal pulse shape. Therefore, a major issue in the field of optimal control is how to retrieve physical information directly from the optimally shaped laser pulse. This so-called "problem of inversion" [26] has not been solved yet. In this concept an atomic system constitutes a promising candidate for optimization experiments, which would provide information involving the dynamics and structure of the quantum system. On the basis of the results found in the optimization experiments performed on the ion and photoelectron signals, new spectroscopic information involving the femtosecond dynamic of double ionization of atomic calcium is presented.

In Chapter 5, a transition into studying larger molecular systems is carried out. The isomerization reactions involving double bonds are the subject of interest there. This

kind of reactions has been the topic of intense research in the past years in order to understand how light can be converted into mechanical motion on a molecular scale. Absorption of an ultraviolet photon leads to a transition from the bonding π to the anti bonding $\pi^\star$ orbital of the ethylene double bond ($\pi\pi^\star$ excitation) which then in a simplified picture allows the molecule to freely rotate and isomerize. In Chapter 5, a spectroscopic study using the pump-probe scheme as well as an adaptive control experiment using photoelectrons signal as feedback are presented. The implementation of photoelectron spectroscopy into adaptive femtosecond experiments is a totally new perspective which has been hardly exploited up to now (only one example is found in the literature [25]).The experiments in Chapters 3 and 4 constitute an attempt towards this goal.

In Chapter 6, adaptive quantum control is applied to a molecular Metallocene catalyst, the electronic structure of which was practically not available. Metallocenes are organometallic catalysts, particularly interesting in the polymer science for their unique properties in polymerization reactions of ethene and propane. They belong to the family of *Ziegler-Natta* catalysts, discovered in 1953 by Karl Ziegler. The goal of the control experiments was the activation of the catalyst by means of femtosecond laser radiation. This was accomplished by selective cleavage of specific ligands of the molecule. This study was performed on the request of the chemical industry concern BASF. Finally the thesis is summarized in Chapter 7 and the bibliographic references are listed.

2 Theoretical background

In this chapter, a number of theoretical aspects, concerning the interactions of femtosecond laser raditation with atomic and molecular systems, are addressed. First, the formalism employed to describe femtosecond laser radiation is discussed, where special terms like "the chirp" or the instantaneous frequency of a laser pulse are introduced, as well as graphical methods to represent complex laser pulses. The second and third sections are dedicated to femtosecond laser excitation of atoms and molecules. There, the dynamics following electronic excitation of the systems are discussed, as well as aspects of their quantum mechanical structure. In the last section, different schemes of laser control are presented. They serve as a brief introduction to the possibility of utilizing the coherent properties of laser radiation to influence the outcome of photoexcitation in the quantum systems.

2.1 Mathematical description of femtosecond laser pulses

A femtosecond laser pulse is a temporally localized electromagnetic wave. To describe the time evolution of the associated electric field $E(\vec{r}, t)$ at a fixed geometrical point, the complex representation shown in Eq. 2.1 can be employed.

$$E(t) = E^+(t) + E^-(t) = 2\ Re E^+(t) \qquad ; \qquad E^+(t) = (E^-(t))^* \qquad (2.1)$$

As long as the oscillation period of the electromagnetic wave is shorter that the total pulse duration, the $E^+(t)$ function can be expressed as a product of an amplitude and a phase term.

$$E^+(t) = A(t)\exp(\Phi(t)) \qquad (2.2)$$

The phase function $\Phi(t)$ can be further developed into a Taylor-series, the so-called temporal *chirp*-development.

$$\Phi(t) = a_\circ + a_1(t - t_\circ) + \frac{1}{2}a_2(t - t_\circ)^2 + \ldots \tag{2.3}$$

The term $a_\circ = \Phi(t_\circ)$ is the absolute phase, which determines the exact position of the electric field oscillation in respect to the pulse envelope $A(t)$. The quantity $a_1 = \Phi'(t)|_{t_\circ}$ is defined as the *carrier frequency* $\omega_\circ$ of the electric field. The higher order terms $a_n(n \geq 2)$ are denoted as temporal $(n-1)^{th}$ order "Chirp". When $a_2 = \Phi''(t)|_{t_\circ} > 0$, the instantaneous frequency $d\Phi(t)/dt$ of the laser pulse increases in course of the pulse propagation. This is described as an "Up-Chirp". Accordingly, the opposite case $a_2 = \Phi''(t)|_{t_\circ} < 0$ is described as a "Down-Chirp".

In the frequency domain, an equivalent representation of the electric field is possible via the function $E(\omega)$, related to $E(t)$ by:

$$E(t) = \mathcal{FT}\left\{E(\omega)\right\} = \frac{1}{\sqrt{2\pi}}\int\limits_{-\infty}^{\infty} E(\omega)e^{i\omega t}dt \tag{2.4}$$

$$E(\omega) = \mathcal{FT}^{-1}\left\{E(t)\right\} = \frac{1}{\sqrt{2\pi}}\int\limits_{-\infty}^{\infty} E(t)e^{-i\omega t}dt \tag{2.5}$$

$E(\omega)$ can also be expressed as the sum of two complex conjugate components $E^+(\omega)$ and $E^-(\omega)$. Analogous to Eq. 2.2, $E^+(\omega)$ is dismantled into a real spectral amplitude $A(\omega)$ and a spectral phase $\Phi(\omega)$ term.

$$E^+(\omega) = A(\omega)\exp(\Phi(\omega)) \tag{2.6}$$

Also, the spectral phase function is analyzed into the Taylor-series:

$$\Phi(\omega) = b_\circ + b_1(\omega - \omega_\circ) + \frac{1}{2}b_2(\omega - \omega_\circ)^2 + \ldots \tag{2.7}$$

The components $b_n = d^n\Phi(\omega)/d\omega^n|_{\omega=\omega_\circ}$ are defined as the $(n-1)^{th}$ order "Chirp" in the frequency space. In this case, the zero order term $b_\circ$ has no particular physical meaning, while b_1 term corresponds to the temporal delay of the laser pulse in respect to reference time $t = t_\circ$. When all other terms are equal to zero ($b_n = 0 \ (n > 1)$), the laser pulse is denoted as "Unchirped".

The temporal profile of a femtosecond laser pulse can be described by the function:

$$I(t) = \varepsilon_\circ c_\circ n\frac{1}{T}\int\limits_{t-\frac{T}{2}}^{t+\frac{T}{2}} E^2(t')dt' = \frac{1}{2}\varepsilon_\circ c_\circ nA^2(t) \tag{2.8}$$

known as the temporal intensity function. In the above expression, $T = 2\pi/\omega(t)$ is the oscillation period of the electric field and $\varepsilon_\circ$ is the dielectric constant in vacuum. Accordingly, in the frequency domain, the spectral intensity function $I(\omega)$ is defined.

$$I(\omega) = 2\varepsilon_\circ c_\circ n |E^+(\omega)|^2 \tag{2.9}$$

The pulse duration τ_p and the bandwidth $\Delta\omega_p$ of the laser field are usually characterized by the width of the $I(t)$ and $I(\omega)$ functions, respectively, measured at the half of their maximal values (*Full Width at Half Max*-FWHM). It has to be noted that these quantities are representative only when the structure of the laser pulse is not very complex. In the opposite case, the complete information from the complex functions $E^+(t)$ and $E^-(t)$ is required.

The mathematical description of femtosecond laser pulses in the frequency domain has the advantage that effects, like the broadening of the laser pulse that propagates through a dispersing material, can be easily addressed. After the laser pulse passes through a material of length L and a refractive index $n(\omega)$ it's spectral phase is shifted by:

$$\Phi(\omega) \rightarrow \Phi(\omega) + \Delta\Phi(\omega) = \Phi(\omega) + \frac{\omega n(\omega) L}{c_\circ} \tag{2.10}$$

Where $c_\circ$ is the speed of light in vacuum. A modulation of the spectral phase has a direct influence on the temporal profile of the pulse. This is illustrated in Fig. 2.1. The temporal amplitudes $A(t)$ of pulses with spectral chirp: $b_1 = 0$ fs, $b_2 = 5 \cdot 10^3$ fs^2, $b_3 = 1 \cdot 10^6$ fs^3 and $b_4 = 1 \cdot 10^8$ fs^4 are depicted in graphs a, b, c and d, respectively. In graphs e, f, g and h the corresponding spectral phase $\Phi(\omega)$ (dashed curves), and the spectral intensity functions $A(\omega)$ (solid curves) are shown. The spectral phase function is limited within a range from $-\pi$ to π (phase wrapping). For all pulses the spectral intensity is a Gaussian function centered at 800 nm with a bandwidth $\Delta\omega_p$=10 nm. The first pulse ($b_1 = 0$ fs) is unchirped (bandwidth limited) with a duration of τ_p=95 fs and a Gaussian profile. Then, a quadratic ($b_2 = 5 \cdot 10^3$ fs^2) chirp is added to the spectral phase (Fig. 2.1f). The pulse duration increases to 180 fs (Fig. 2.1b). However, the temporal profile of the pulse is still a Gaussian function. The shape of the laser pulse changed dramatically when the spectral phase acquires a second order spectral chirp $b_3 = 1 \cdot 10^6$ fs^3 (Fig. 2.1g). Now, the laser pulse is completely asymmetric, and a complex after-pulses sequence is visible on the right side of the pulse (Fig. 2.1c). The FWHM of $I(t)$ amounts 150 fs. However, this is not indicative of the actual (over 400 fs)
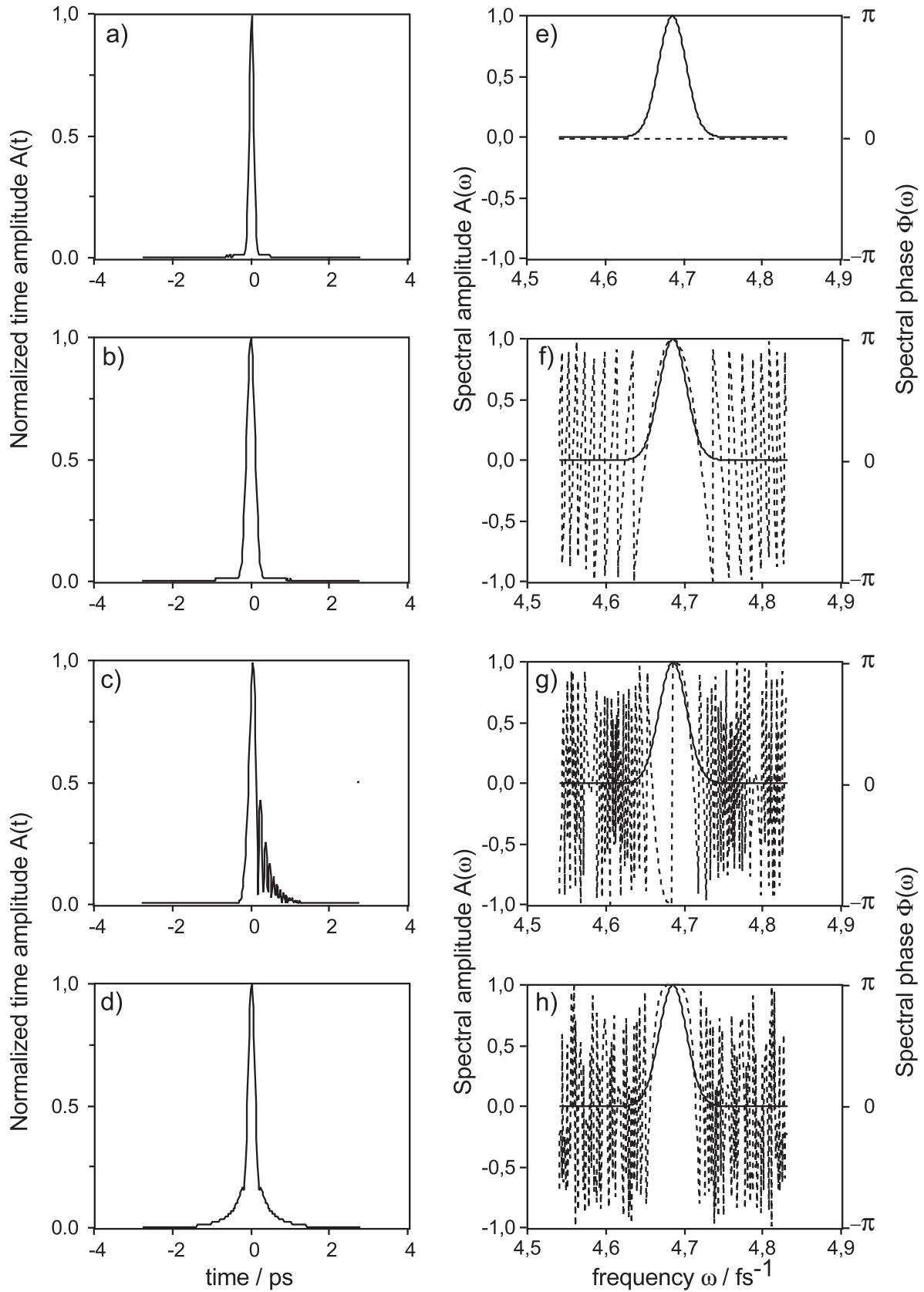
Figure 2.1: Modulation of the spectral phase. In figures a...d the temporal amplitude function $A(t)$ is simulated for 800 nm femtosecond laser pulses and 10 nm spectral width. The corresponding spectral chirp used for the simulation was: $b_1 = 0$ fs, $b_2 = 5 \cdot 10^3$ fs^2, $b_3 = 1 \cdot 10^6$ fs^3 and $b_4 = 1 \cdot 10^8$ fs^4, which is depicted in graphs e...h (dashed curves), together with the spectral amplitude $A(\omega)$ (solid curves).

spreading of the pulse. A symmetric broad profile is acquired with a third order chirp $b_4 = 1 \cdot 10^8$ fs^4 (Fig. 2.1d)). In a similar manner, even more complex pulse structures are possible when functions, like periodic or step-functions, are applied to the spectral phase.

The graphical representation of complex pulses can be a tedious task. A fast varying spectral and temporal phase function is hard to interpret and provides no intuitive understanding of the pulse's properties. This purpose is rather served by the so-called Wigner-Distribution function [27, 28], which is defined by [29, 30]:

$$W(E^+, \omega, t) = \int\limits_{-\infty}^{+\infty} E^+(\omega + \Omega)[E^+(\omega - \Omega)]^* e^{i2\Omega t} d\Omega \qquad (2.11)$$

or the equivalent expression in the time domain:

$$W(E^+, \omega, t) = \int\limits_{-\infty}^{+\infty} E^+(t + \tau)[E^+(t - \tau)]^* e^{i2\Omega \tau} d\tau \qquad (2.12)$$

This mathematical formalism was introduced in 1932 by E. Wigner [31] in the context of a phase-space quantum mechanics. The Wigner function displays both the spectral as well as temporal properties of the laser pulse. It allows for the intuitive representation of the timing at which the different frequency components of the laser spectrum are incident within the femtosecond pulse duration. The Wigner trace of two chirped laser pulses are shown in Fig. 2.2. In a) a linear up-chirp $b_2 = 1 \cdot 10^4$ fs^2 is applied to the spectral phase function of the laser pulse. It clearly shows how the low frequency components (red part) of the laser spectrum are incident in the leading edge of the pulse. Then, the instantaneous frequency increases linearly with the propagation time. In the trailing edge of the pulses the higher frequency components (blue part) of the laser spectrum are dominant. In the second example b), a quadratic chirp $b_3 = 1 \cdot 10^6$ fs^3 is employed. The parabolic pattern there indicates the second order modulation of the spectral phase. A similar analysis of the instantaneous frequency variations can be conducted as before. The values of the Wigner function are always real numbers with positive (black area in Fig. 2.2b) or negative values (the white area). The values at a specific point upon the distribution has no measurable physical meaning. The exact and simultaneous measurement of both the time at which a photon is incident at a given geometrical point, and the frequency of the photon is not possible, due to the uncertainty principle of Heisenberg. To acquire physical information about the instantaneous frequency of the laser pulse, a small area of the Wigner distribution has
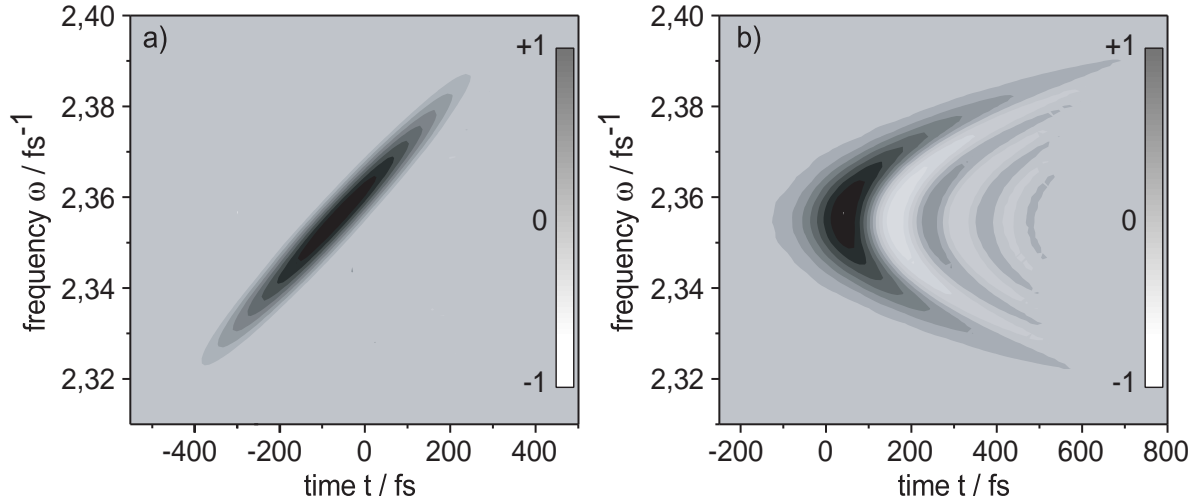
Figure 2.2: Wigner representation of simulated chirped 800 nm femtosecond laser pulses. The spectral phase function exhibits a) a linear chirp $b_2 = 1 \cdot 10^4$ fs^2 and b) a quadratic chirp $b_3 = 1 \cdot 10^6$ fs^3

to be integrated along the time and frequency intervals σ_t and σ_ω, the product of which must exceed the uncertainty limit $\hbar$. The values of this integral are always positive. The exact temporal profile of the femtosecond laser pulse can be acquired by the infinite integral along the frequency axis ($\sigma_t \to 0$):

$$I(t) = 2\varepsilon_\circ cn \int\limits_{-\infty}^{+\infty} W(E^+, \omega, t)d\omega \tag{2.13}$$

Accordingly, the laser spectrum ($\sigma_\omega \to 0$) is given by:

$$I(\omega) = 2\varepsilon_\circ cn \int\limits_{-\infty}^{+\infty} W(E^+, \omega, t)dt \tag{2.14}$$

2.2   Photo-ionization in intense laser fields

One characteristic of femtosecond laser pulses is the extreme field peak-intensity due to their high temporal localization. When a laser pulse of 100 fs duration and 1 mJ energy is focused onto an area of diameter 100 μm, the resulting field reaches a peak intensity of the order of 10^{15} W/cm^2. The electric field associated to this intensity is only one order of magnitude lower than the Coulomb binding field that an electron experiences in the 1st Bohr orbital of hydrogen. Therefore, it is plausible that the first order perturbation theory cannot describe the interaction phenomena of such laser fields with an atom or molecule. For instance, the AC-Stark effect discussed in Section 2.2.2, often plays an important role in femtosecond photo-ionization. As the intensity of the laser field increases, the energy levels of the atom or molecule can be shifted. This brings them in or out of resonance with the laser photon energies employed. And if the laser intensity is high enough, electrons can absorb more photons than those required to reach the ionization threshold. Then, the phenomenon denoted as *Above-Threshold-Ionization* (ATI) is observed. The mechanisms of photo-ionization are summarized under two basic concepts, namely the *Resonant-Multiphoton-Ionization* (REMPI) and the *Tunnel-Ionization* (TI). In REMPI the exact energy of the excited state can be reached by absorption of an integer number of photons. In this way absorption of N photons excites the system to an intermediate state, from which by further photon-absorption ionization can occur. In TI, the Coulomb binding potential of the atom is distorted due to the high laser field, and electrons can escape. By increasing laser intensity the dominant ionization process shifts from multiphoton ionization to tunnel ionization. The transition from one mechanism to the other is defined by the so-called *Keldysh parameter* which is discussed in Section 2.2.4.

2.2.1   Multiphoton ionization

Due the high photon flux induced by focusing a laser pulse, it is possible that more than one photon are engaged in a laser-matter interaction process. This allows for excitation to electronic states that are not accessible by one photon absorption, where the coupled states have to be of opposite symmetry. Given that the energy-sum $N\hbar\omega$ of the absorbed photons matches the energy difference between the ground and the excited electronic state, the system can be resonantly excited to the upper state and ionize by further absorption of photons. Besides this *Resonant-Multiphoton-Ionization* (REMPI), the system can also be directly ionized by absorption of N photons without an intermediate

resonance being involved. Such a process is described as *non-resonant Multiphoton-Ionization* and was investigated for the first time more than 70 years ago by Maria Göppert-Mayer [32]. Within the perturbation theory formalism the probability that multiphoton ionization occurs depends on the photon flux following the so-called "power law" [33]. It testifies that the ionization probability R_N of a N-photon photoprocess scales with the Nth power of the photon flux Φ:

$$R_N = \sigma_N \Phi^N \qquad (2.15)$$

where σ_N represents a generalized cross-section of the interaction. Nevertheless, attention has to be paid to interpret the experimental data. For laser multiphoton ionization that takes place at higher field intensities strong deviations from the power law can arise due to saturation of the transition. In a saturated electronic transition, the entire population of the ground state is transferred to the excited electronic state with a single pulse. As a result, further increase of the excitation field does not affect the ionization rate. However, under realistic experimental conditions the non-uniformity of the intensity along the laser focus has to be taken into account. Saturation affects mainly the central and more intense part of the laser focus. In the outer parts, the intensity of the laser field is lower and the power law still holds. In this case, the total ionization signal still increases with the laser intensity but scales with a power $N_{sat} < N$. A similar effect is induced due the gradual temporal increase of the laser pulse. The depletion of the ground state can be realized within the leading edge of the laser pulse and the maximum field intensity, reached at the high point of the laser pulses, has not effect on the transition.

2.2.2 Dynamical shifting resonances

Every laser pulse is associated with the build-up and subsequent drop of an intense laser field. This induces a time-dependent disturbance of the electronic states of the atom that interacts with the laser field. On the other hand, intermediate resonant states play a very important role in multiphoton-ionization. It is therefore helpful to clarify the behaviour of these states in connection to the intense laser fields. At first, consider free electrons that find themselves inside a homogeneous, high-frequency electromagnetic laser field. Such electrons can be considered as classic charged particle that oscillate around an equilibrium position in a manner similar to the harmonic oscillator. The

average oscillation kinetic energy of a single electron is given by [34, 35]:

$$U_P = \frac{e^2 E_\circ^2}{4m_e\omega^2} = \frac{e^2}{4m_e c e_\circ \omega^2} I \tag{2.16}$$

where $E_\circ$ is the amplitude, ω the optical frequency and I the intensity of the electric field. The quantity U_P is denoted as *the ponderomotive potential* or, relevant to the oscillatory motion of the electrons, as *quiver energy*. With the increasing quantum number n the probability of a Rydberg-electron to be found in the close-area of the nucleus decreases rapidly as $1/n^3$. In a rough approximation, the most distant Rydberg-electron can also be treated as classic charged particles. The potential energy of the Rydberg state will then be approximately shifted by the same amount as the quiver energy. To acquire a more precise picture of the behaviour of the electrons in a laser field a quantum mechanical treatment is necessary. In the work of P. Avan [36] from 1976, the behaviour of the bound states of an atom inside a high-frequency electromagnetic field is discussed. It is shown that all Rydberg states are subsequent to a uniform shift to higher energies. However, when the photon energy is smaller than the energy distance between the ground and the first excited state, the energy of the first is lowered. This so-called AC-Stark-Effect can be easily explained within the first order perturbation theory. Suppose E_i is the energy of the unperturbed quantum state and ΔE_i the shift due to the interaction with the laser field. The following formula holds:

$$\Delta E_i \propto \sum_{i \neq j} \frac{|V_{i,j}|^2 (E_i - E_j)}{(E_i - E_j)^2 - (\hbar\omega)^2} \tag{2.17}$$

where $V_{i,j}$ is the matrix element of the coupling between the two i and j states. If the photon energy is larger than the energy distance between the ground and the first excited state ($\hbar\omega > E_1 - E_g$), the denominator in Eq. 2.17 is negative and the ground state is energetically shifted upwards. In the opposite case ($\hbar\omega < E_1 - E_g$) the ground state is shifted downwards.

Compared to excited states, the energy shift of the ground state is relatively small [37] and hardly becomes plausible with a classical model. Nevertheless, the approach of the quiver motion of the electrons and the ponderomotive potential provide, can well describe the behaviour of the Rydberg states located close to the ionization threshold [34]. These states are shifted parallel and linear with the laser intensity (Eq. 2.16). In the experiments described in Chapter 4, such states serve as intermediate resonances for excitation to the double ionization threshold of calcium atom. To excite a specific electronic state of the system the appropriate intensity has to be chosen in such a way,
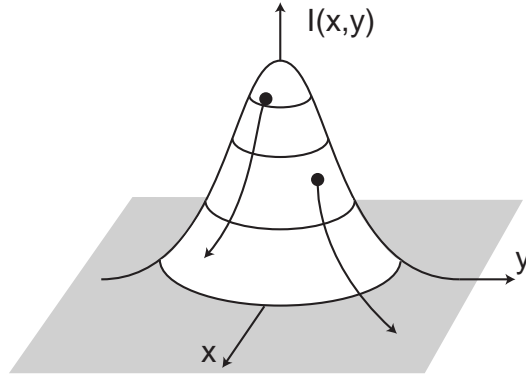
Figure 2.3: Schematic representation of the motion of photoelectrons inside the laser focus. When the laser pulse duration is long enough, the electrons are accelerated due to the gradient of the ponderomotive potential and exit the laser interaction region.

that the sum of the energy of the unperturbed state and U_p matches the energy of the absorbed photons. In this way, the electronic excitation of an atom or molecule can be controlled by specific modulation of the intensity profile of the excitation laser pulse.

In the previous discussion, the time duration of the laser pulses has not been taken into account. For the above conclusions to be valid it is important that the laser pulses are short. Consider an electron emitted during the ionization process. Inside the laser focus, the electron has, apart from its kinetic energy, the additional quiver energy. Assuming for instance the Gaussian intensity profile shown Fig. 2.3, the additional quiver energy decreases in the outer areas of the distribution. If the pulse duration is longer than the time needed to drift out of the focus area, the electron experiences a gradient of the ponderomotive potential and becomes accelerated. In addition to the initial velocity $v_\circ$, from the excess energy of the ionization, the free electron retains the quiver energy as kinetic energy. On the other hand, if the laser pulse is shorter than the time needed to drift out of the focal area, this extra kinetic energy is not retained by the electron rather transferred back to the decreasing laser field before the electron is accelerated.

In Fig. 2.4 two excited states of a hypothetical atomic system are shown. They serve as intermediate resonances in a N+1 photo-ionization. N is the number of photons, the energy sum of which lies directly below the ionization potential (IP):

$$N \cdot \hbar\omega < IP < (N+1)\hbar\omega \tag{2.18}$$

Every laser pulse spans a certain intensity region. The poderomotive potential then varies accordingly and results to a time dependent energy shift of the Rydberg states X_1^* and X_2^*. In the approximation that the AC-Stark shift of the ground state is negligible,
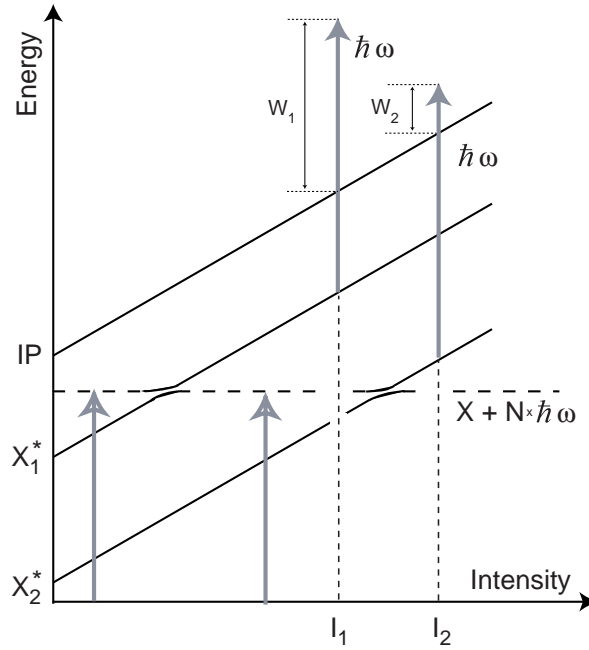
Figure 2.4: Energy scheme of two shifting resonances X_1^* and X_2^*. The AC-Stark energy shift bring the two states into resonance with the N-photon transition from the ground state. By absorption of one more photon the system is ionized. The resulting kinetic energy of the emitted photoelectron is denoted W_1 and W_2 respectively for the two different intermediate resonances.

the following picture can be drawn: The ground state is "dressed" with N photons and a *virtual* state $X + N \times \hbar\omega$ is populated. As a function of the laser intensity the dressed state crosses the up-shifting Rydberg resonances. With the absorption of N photons for instance, an excitation to the intermediate state X_1^* can take place, which eventually ionizes by absorbing one more photon. The resulting kinetic energy of the photoelectron is given by:

$$W_1 = U_{X_1^*} + \hbar\omega - IP \tag{2.19}$$

It makes no difference for the values of X_1^* and IP if the unperturbed or the AC-Stark shifted energies are chosen, since the Rydberg states and the ionization potential are shifted parallel to each other. For higher laser intensities a second crossing 2 is accessed and X_2^* serves as intermediate resonance. The resulting kinetic energy of the emitted photoelectron is accordingly given by:

$$W_2 = U_{X_2^*} + \hbar\omega - IP < W_1 \tag{2.20}$$

Therefore, by increasing the laser field intensity additional ionization channels can open. If more states were found in the vicinity of the N photon transition, they could also be

tuned into resonance by simply increasing the intensity. Such excitation schemes have been experimentally investigated by different research groups [37–41] utilizing various wavelengths in xenon and argon. Also, in this work, the channel switching effect was employed for the purpose of calibrating the photoelectron spectrometer (Chapter 3.3.5).

Suppose that in the previous example an (8 + 1)-photon ionization was realized. A further increase of the laser field intensity can lead to switching into a (9 + 1)-ionization scheme. This would occur if the AC-Stark shift of the ionization potential was so large that $IP + U_p > 9\hbar\omega$. Then the (8 + 1) channel would close and states of different parity would be involved, since the excitation scheme would pass from an odd to an even total number of photons.

2.2.3   Multiphoton transitions above the ionization threshold

In the previously discussed scheme, it was assumed that the electrons in the excited Rydberg states absorb only one photon in order to go to the continuum. However, it is possible that more than one photon is absorbed, and the kinetic energy of the emitted photoelectron is increased by many times the photon energy.

$$W_{e^-} = (N + S)\hbar\omega - IP - U_P \tag{2.21}$$

where N is the number of photons required to excite the electron from the ground state just above the ionization threshold, and S is the number of additional photons that excite the electron energetically higher inside the atomic continuum. This effect is known as *above threshold ionization* (ATI) and was investigated in 1979 for the first time by P. Agostini [42] in xenon atoms. The effect of ATI manifests itself on the photoelectron energy spectrum by the appearance of multiple peaks, with a successive energy distance of $\hbar\omega$. Generally, the amplitude of these peaks decreases as a function of the order of S (exceptionally, due to certain resonance effects this rule can be violated). The numerous peaks observed in the ATI photoelectron spectrum correspond to transitions from the atomic ground state up to different final states above the first ionization limit. However, when the laser field intensity becomes sufficiently high, a transition to a final state above the double ionization limit is even possible via multi-photon absorption. In this case, the energy gained by the absorption is sufficient to extract two valence electrons from the atom and to generate a doubly charged ion.

In Fig. 2.5, a simplified energy-level diagram of a model two-electron atom is depicted, where a large number of single as well as double excited levels are shown. These states can serve as intermediate resonances in the multiphoton excitation scheme and

enhance the probability of the double ionization. In Fig. 2.5 three different classes of atomic states are shown:

- Discrete neutral states (singly and doubly excited)

- Atomic continua

- Cationic states

On the right side, the levels of the ionized system are plotted (cationic states). The lowest one is the first ionization threshold of the atom. At this threshold the atomic continuum starts. The excited levels of the (one-electron) cation also constitute thresholds for the two-electron atom. A number of different atomic continua are marked by the gradient colored frames on the central part of the diagram, starting at the corresponding ionic state. The discrete levels of the two-electron atom (left) are bound or quasi-bound states. Each of these states is associated with a specific cationic state (dashed lines) and is therefore placed below the corresponding ionization threshold. The states that are associated to the ground cationic state are singly excited bound states, while the ones associated with excited cationic state are doubly excited. All two-electron atoms contain doubly excited states that are degenerate with the atomic continuum. In the initially localized state of the system, at least one of the electrons can escape the atom due to the mutual Coulomb repulsion (configuration interaction - CI) between the two valence electrons. This occurs without the exchange of energy with the surrounding environment. Such metastable states are therefore referred to as *autoionizing states*. The parameter that determines the lifetime of an autoionizing state is the strength of the Coulombic repulsion between the two electrons i.e. the amplitude of the coupling between the discrete doubly excited state and the degenerate states of the continuum. The decay of an autoionizing state results in the formation of a singly charged ion, which can be left in one of its ground or excited cationic states. By subsequent absorption of additional photons the singly charged ion can be further excited, so that the second valence electron is transferred to the double ionization continuum. This mechanism of double ionization takes place in a stepwise manner by which the two electrons are freed and is therefore denoted as *sequential double ionization* [46].

The way that multiphoton double ionization of an atom occurs is a long standing issue in atomic physics. Apart from the sequential mechanism another scenario is discussed, according to which the intermediate formation of a bound ionic state is not necessary. In this picture, the two valence electrons are rather simultaneously excited and eventually
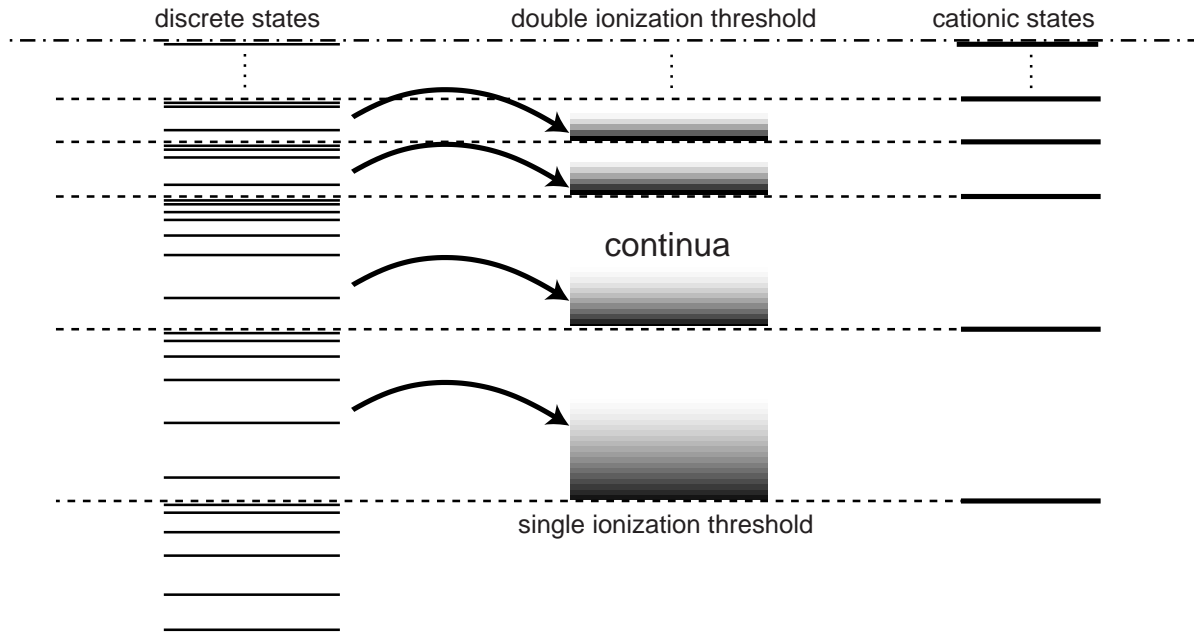
Figure 2.5: Excited states of a model two-electron atom. Three classes of excited states are shown a) discrete neutral states (left), b) Cationic states (right), corresponding to ionization thresholds of the two-electron atom (dashed lines) and c) Atomic continua (gradient colored frames-center). The double ionization threshold is located at the upper end of the diagram (dash-dotted line)

ejected into the atomic continuum. In this *non-sequential double ionization* [47] the correlation between the two electrons plays a very important role, rather than in the case of the step wise process. In the context of intermediate autoionizing resonances, a non-sequential mechanism would involve that within the lifetime of the state (before the autoionizing state decays to the single ionization continuum) an additional number of photons is absorbed and the two valence electrons of the atom are transferred to an energetically higher doubly excited electronic configuration. By increasing the excitation level a series of $nln'l'$ levels is accessed, which eventually reaches the two-electron escape limit. Therefore, such a series can be viewed as a two-electron ionization ladder.

2.2.4   Tunnel- and Field-Ionization

When an intense laser field interacts with an atomic or molecular system, a number of effects comes into play, due to the deformation of the potential that binds the electrons to the atom or molecule. This deformation can be described by means of an instantaneous potential which varies periodically, following the optical frequency of the laser field. Such an effective potential is shown in Fig. 2.6 for the case of a simple $1/R$ potential.
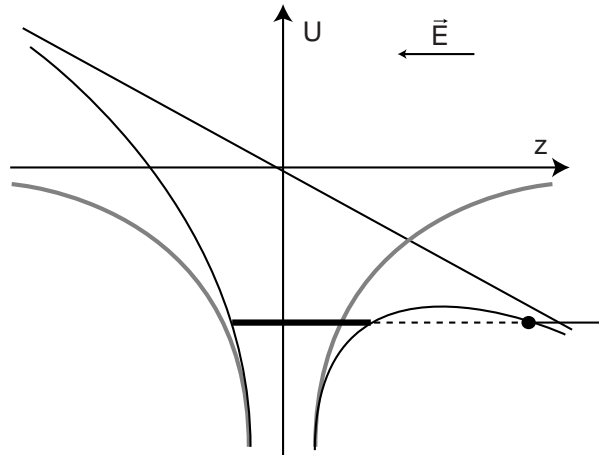
Figure 2.6: Tunnel ionization. The electric field of the laser causes the distortion of the Coulombic potential of the nucleus. Electronic states that lie above the induced barrier will be field-ionized while for the states below the barrier the emission of electrons to the atomic continuum is possible via tunneling through the potential barrier.

The polarization of the laser is chosen to be parallel to the z-axis, which indicates the distance from the atomic core. On the right side the potential barrier is lowered, so that the electrons can tunnel through this barrier and reach the continuum. The electrons that escape in this process are mainly emitted in the direction of the polarization and exhibit no sharp energy distribution. Also, excited bound states, close to the ionization threshold can loose their electrons which can flow over the potential barrier. This process is known as *field ionization.*

A parameter which characterizes the borderline between multiphoton ionization and tunnel ionization is the so-called *Keldysh-parameter* [43]:

$$\gamma = \sqrt{\frac{IP}{2U_P}} \tag{2.22}$$

γ is practically the measure of the ratio between the tunneling time and the optical period of the electromagnetic field [43, 44]. If $\gamma \ll 1$, then tunnel ionization is the dominant process. This occurs for rather high intensities.

2.3   Dynamics in polyatomic molecules

The complexity of polyatomic molecules originates from the numerous degrees of free-
dom in their nuclear motion. In contrast, diatomic molecules involve only one nuclear
coordinate, the inter-atomic distance, and a potential curve is sufficient to describe the
energy of the system U(R) as the two atoms are brought closer to, or moved away from
one another. For a polyatomic molecule there are more nuclear coordinates, inter-atomic
distances and the bond angles. Assuming only two active coordinates and plotting these
against the potential energy, a three dimensional topological map is produced, the *Po-
tential Energy Surface* (PES). A PES with more than two coordinates is denoted as a
Potential Energy Hypersurface but is impossible to visualize graphically .

The ultrafast dynamics of polyatomic molecules are dominated by the *non-adiabatic
couplings* between the PESs, which in many cases come very close to each other. In this
concept, the so-called *conical intersections* play an important role. These are specific
locations upon the multi-dimensional space of the nuclear motion where a non-adiabatic
degeneration between two PES of the system is taking place. The collapse of the Born-
Oppenheimer approximation in the area of a conical intersection and the pronounced
unharmonicity of the PES cause a very strong coupling between the electronic states.
This induces an ultrafast dynamic in the femtosecond timescale.

2.3.1   The adiabatic description of molecular electronic states

The many-particle three-dimensional time-independent Schrödinger equation is adapted
for molecular systems. The molecular Hamiltonian is:

$$H = T_N + T_{el} + V(\overrightarrow{r}, \overrightarrow{R}),$$ (2.23)

The first terms T_N and T_{el} represent the nuclear kinetic energy operator and the elec-
tronic kinetic energy operator, respectively. The third term is the potential energy of
the system, where $\overrightarrow{r}$ and $\overrightarrow{R}$ are the collective coordinates of the electrons and the
nuclei, respectively. According to the Born-Oppenheimer (BO) approximation [48], the
nuclei are much heavier than the electrons in a molecular system and their motion can
be separated. This means that as the nuclei move, the electrons move infinitely fast and
react to the nuclear changes instantaneously. Under this assumption, the Schrödinger
wavefunction is analyzed into an electronic and a nuclear component. The adiabatic
electronic component $\varphi_n(\overrightarrow{r}; \overrightarrow{R})$ is an eigenfunction of the electronic time-independent

Schröndiger equation:

$$\{T_{el} + V(\vec{r}, \vec{R})\}\varphi_n(\vec{r}; \vec{R}) = V_n(\vec{R})\varphi_n(\vec{r}; \vec{R}), \qquad (2.24)$$

for a fixed nuclear coordinate $\vec{R}$. By solving the above eigenvalue $V(\vec{R})$ problem for different values of $\vec{R}$, the multidimentional PES can be calculated and subsequently the forces $F_k(\vec{R}) = -\partial V_n(\vec{R})/\partial R_k$ that are responsible for the molecular dynamics. The total time-independent molecular wavefunction $\Psi(\vec{r}, \vec{R})$ can be developed into a sum of adiabatic electronic states:

$$\Psi(\vec{r}, \vec{R}) = \sum_n \chi_n(\vec{R})\varphi_n(\vec{r}; \vec{R}), \qquad (2.25)$$

If the above expression is appointed to Eq. 2.23, a system of coupled equations is obtained for the nuclear wavefunction $\chi_n(\vec{R})$.

$$\{T_N + V_n(\vec{R}) - E\}\chi_n(\vec{R}) = \sum_{m \neq n} \Lambda_{nm}\chi_m(\vec{R}), \qquad (2.26)$$

The matrix element Λ_{nm} is given by:

$$\Lambda_{nm} = -\int d\vec{r}\,\varphi_n^*(\vec{r}; \vec{R})[T_N, \varphi_m(\vec{r}; \vec{R})], \qquad (2.27)$$

and represents the *non-adiabatic coupling* between the electronic states φ_n and φ_m.

If the factor Λ_{nm} is neglected, a system of uncoupled equations is obtained.

$$\{T_N + V_n(\vec{R}) - E\}\chi_n(\vec{R}) = 0, \qquad (2.28)$$

which describes the nuclear motion in the nth electronic state. Under this approximation, a coupling between the different electronic states does not exist and the nuclear dynamic in a specific electronic state is not influenced by the dynamics in other electronic states. This separation defines the adiabatic BO approximation.

The BO approximation is valid when the electronic wavefunctions $\varphi_n(\vec{r}; \vec{R})$ depend hardly on the nuclear coordinate i.e. the kinetic energy of the nuclei, related to Λ_{nm}, remains small compared to the energy distance between the electronic states. The non-adiabatic coupling becomes rather strong or even singular, when two electronic PES come closer or intersect with each other. In this case, the character of the wavefunction change abruptly as a function of $\vec{R}$ and the deviations due to the nuclei kinetic energy are no more negligible. In most cases, this occurs close to avoided crossings or conical intersections between two PES. There, the strong non-adiabatic coupling breaks the BO approximation.

2.3.2 Wavepacket formalism of the molecular vibrational motion

When femtosecond laser pulses interact with a molecule, a coherent superposition of multiple vibrational states can be created due to the broad spectral bandwidth of the laser field. The phase-coupled excitation of these states is denoted as a *wave packet*. A simplified expression can written for the wavefunction $|\Psi >$ of the wavepacket as a superposition of the adiabatic wavefunctions of the coupled states:

$$|\Psi(r,R) >= \sum_{v}^{\infty} c_v \chi_v(\overrightarrow{R}) \varphi_u(\overrightarrow{r}; \overrightarrow{R}), \tag{2.29}$$

The coefficients c_v are time-dependent, and v represents the vibrational quantum number of the state. The phase of the c_v coefficients is given by:

$$\theta_v(t) = e^{-i(v+1/2)\omega\ t + \phi_{v\circ}}, \tag{2.30}$$

To derive the above expressions it was assumed that the energy of the vibrational states is:

$$E_v = \hbar\omega(v + 1/2), \tag{2.31}$$

The constant phase term $\phi_{v\circ}$ is defined by the spectral phase of excitation laser pulses. The coherent excitation to the vibrational states leads to a modulation of the nuclear bond distance R. The expectation value of the bond distance $< R >$ is evaluated by separating the stationary and time-dependent terms [61,62]:

$$< R(t) >=< \sum_{j=0}^{\infty} c_j(t) e^{-i(j+1/2)\omega\ t + \phi_{j\circ}} \chi_j(\overrightarrow{R}) |\widehat{R}| \sum_{k=0}^{\infty} c_k(t) e^{-i(k+1/2)\omega\ t + \phi_{k\circ}} \chi_k(\overrightarrow{R}) >, \tag{2.32}$$

$$< R(t) >= \sum_{j=0}^{\infty} \sum_{k=0}^{\infty} c_j(0) c_k(0) e^{-t/T_{1/2}} R_{jk} e^{i(j-k)\omega\ t} \tag{2.33}$$

R_{jk} stands for the matrix element $< \chi_j(\overrightarrow{R})|\widehat{R}|\chi_k(\overrightarrow{R}) >$. The time-dependent coefficients in equation 2.33 are summarized according to:

$$c_j^*(t) c_k(t) = c_j^*(0) c_k(0) e^{-t/T_2} \qquad ; \qquad c_j^*(t) c_j(t) = c_j^*(0) c_j(0) e^{-t/T_1}, \tag{2.34}$$

Assuming that the vibrational levels are eigenstates of a harmonic potential, the matrix elements R_{jk} are non-zero only for $|j \pm k| = 1$. Under this assumption R will oscillate with the eigenfrequency ω of the nuclear bond.
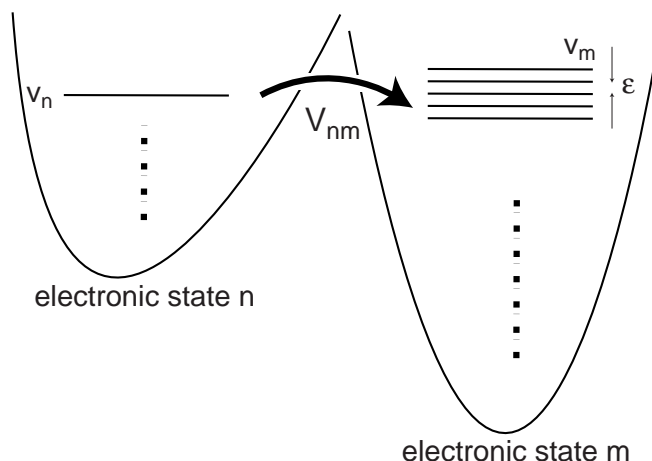
Figure 2.7: Weak non-adiabatic coupling. The two electronic bands n and m are non-adiabatically coupled via their v_n and v_m vibrational levels, respectively. V_{nm} is the non-adiabatic coupling matrix element. The rate constant of the population transfer from n to m is calculated on the basis of *Fermi's golden rule*. ε indicates the middle energy distance of the vibrational levels in the region of m state.

2.3.3   Radiationless transitions via a weak non-adiabatic coupling

Consider the energy scheme shown in Fig. 2.7, where two electronic states are adiabatically coupled via their vibrational levels v_n and v_m. If the origins of the two electronic bands have a large energy distance compared to their successive vibrational states, the adiabatic molecular wavefunctions can be used to describe the transition. The rate constant of the population transfer from n to m is calculated on the basis of *Fermi's golden rule* [49–51].

$$\Gamma = \frac{2\pi}{\hbar} \frac{|V_{nm}|^2}{\varepsilon} \tag{2.35}$$

ε is the average energy separation of the vibrational levels in the region of the v_m. V_{nm} is the non-adiabatic coupling matrix element between the two virbational levels.

$$V_{nm} = < \Psi_{nv_n} | H | \Psi_{mv_m} > \tag{2.36}$$

As shown in Eq. 2.35, the intramolecular conversion between the two electronic bands plays an important role only when $|V_{nm}| \gg \varepsilon$. Such a condition is fulfilled for instance if the lower electronic state exhibits a high density of states ($\varepsilon \to 0$), that are degenerate to the initially populated level. Such a coupling mechanism is addressed in Chapter 5.4, involving the S_2 and S_1 electronic states of stilbene.
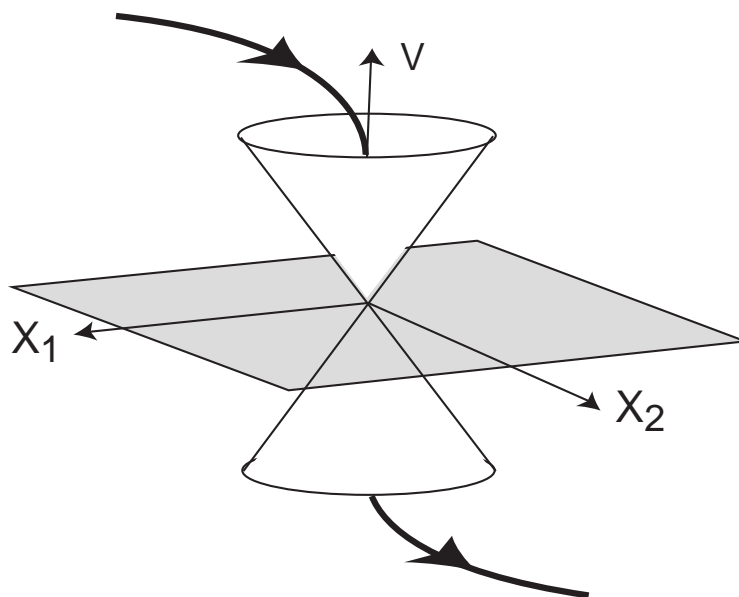
Figure 2.8: Schematic representation of a conical intersection. The PES is plotted along the nuclear coordinates of the tuning mode X_1 and the coupling mode X_2. The black arrow spanning the apex point indicates the strong coupling between the respective electronic states that causes the rapid cross from one electronic state to another.

2.3.4 Dynamics at a conical intersection - the photoisomerization model

Conical intersections occur in regions where two potential surfaces are degenerate and intersect. There, the adiabatic approximation breaks since the kinetic energy of the nuclei is comparable to the energy separation between the electronic states. The strong coupling between the two states causes a rapid crossing from one electronic state to the other. Conical intersections are also known as Jahn-Teller distortions following the advent of the Jahn-Teller theorem in 1937 [52] which describes the effect. At a conical intersection two directions, X_1 and X_2 [53] can be distinguished in the subspace of which the PES has the form of a double cone (Fig. 2.8). Starting from the degenerate apex point of the intersection and moving along the two coordinates the degeneracy of the electronic states is lifted [54]. The two modes are denoted as the *tuning mode* and the *coupling mode*.

The convex geometry of a conical intersection results in the focusing of a wavepacket that propagates upon the upper PES. The wavepacket reaches the apex point of the intersection and passes to the lower PES with a very high transition probability. In certain molecules the lower PES involves more than one energy minimum. They corre-
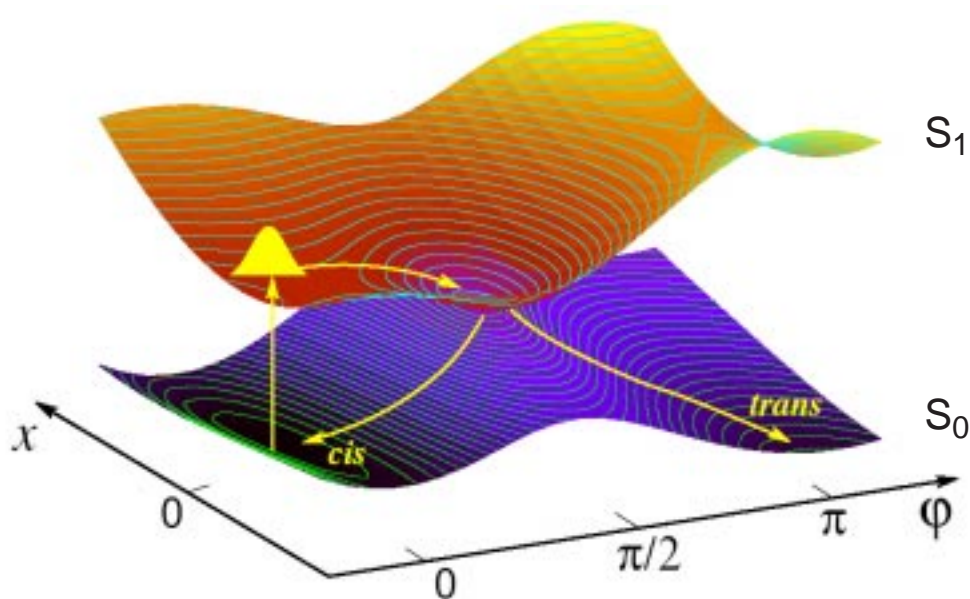
Figure 2.9: Schematic representation of the *cis* → *trans* photoisomerization model by G. Stock et.al. [57]. The ground S_0 and first excited S_1 states of ethylene are plotted along of the torsion angle φ and the coupling mode χ. Starting from the ground *cis* configuration the molecule is excited to the S_1 state. There, it undergoes an ultrafast transition through a conical intersection back to the ground S_0 state.

spond to different geometrical configurations of the nuclei. In Fig. 2.9 the ground S_0 and the first excited S_1 electronic states of ethylene are depicted. The lateral coordinate φ represents the torsion around the central C=C bond and the coordinate χ stands for the so-called pyramidalization of the molecule. In this scheme, the main aspects of a photoinduced isomerization reaction are illustrated, by which the molecule can rotate from the *cis* to the *trans* configuration. The direct transition between the two configurations is limited by the intermediate potential barrier. However, starting from the ground *cis* configuration, a femtosecond laser pulse can excite a wavepacket to the S_1 state. This state exhibits a strong coupling to S_0 via a conical intersection, located along the φ coordinate at the so-called twisted geometry ($\varphi = \pi/2$). The wavepacket reaches the conical intersection and funnels back to the ground state, accessing both the *cis* and the *trans* configurations of the molecule. This model has been successfully applied to isomerization reactions of a large number of polyatomic molecules involving ethylenic (C=C) double bonds [57]. For this class of molecules the reaction coordinate consists of a combination of the torsion angle φ around the (C=C) axis (coupling mode) and other nuclei motions (tuning mode) depending on the specific molecule. The excitation to the upper S_1 electronic state involves the transition from the bonding π orbital of the

C=C group to the anti-bonding $\pi^\star$ orbital. In certain molecules the S_1 surface exhibits a small potential barrier that can slow down the reaction rate.

A radiationless transition between two potential surfaces is also possible via an "avoided crossing". In the context of conical intersections, an avoided crossing can be understood as a slice through the cone (Fig. 2.8) taken slightly forward from the apex point. The distinctive parameter between the two coupling mechanisms is the tuning coordinate. It is simple to visualize that in an actual intersection the transition to the lower PES is easier than in an avoided crossing.

2.4 Elements of quantum control of electronic excitation dynamics

The electronic excitation dynamics in atomic and molecular systems can be influenced by specifically modifying the properties of the excitation laser field(-s) that induces the transition. In this way, both the properties as well as the evolution of the created coherent superposition of excited states can accordingly be influenced. In the following sections, two excitation schemes are discussed that serve as elementary examples in order to show how femtosecond laser control can be realized. The two so-called *pump-probe* and *Brumer-Shapiro* control schemes provide the basis for understanding how the temporal profile as well as the spectral phase of a femtosecond laser pulse can respectively influence the outcome of multiphoton laser transitions.

2.4.1 The Pump-Probe scheme

By means of the pump-probe scheme it is possible to observe atomic and molecular processes that take place upon an excited PES [58–60]. This can involve an ultrafast vibration, dissociation, isomerization, autoionization or other dynamical processes of the quantum system. In the primary pump-step, by absorption of one ore more laser photons a wavepacket is created upon the so-called *transition state* via a coherent super-position of many vibrational states, that lay within the spectral bandwidth of the laser excitation. The motion of the wavepacket describes the vibration of the molecule, as discussed in Section 2.3.2. Within the BO approximation, during the electronic excitation the position of the nuclei remains constant and the transition is denoted as *vertical*. In the general case, the energy region reached by a vertical transition (also known as *Frank-Condon (FC) region*) is not the energetically most favorable configuration upon the excited energy surface and the molecule undergoes an ultrafast geometry change towards the energy minimum of the potential surface. In the probe-step the time evolution of the transient state is interrogated. To achieve this, at the specific probe-time the product distribution is transferred to a detectable state. In the experiments described in this thesis, the later state involves a photoionization continuum where the information about the dynamics of the transient state is acquired by monitoring the mass- and charge-state of the generated cationic product (mass spectroscopy) or by measuring the kinetic energy of the emitted photoelectrons (photoelectron spectroscopy). In both cases, the detected signal is measured as a function of the delay time between the pump- and probe- laser pulses. The first spectroscopic method is suitable for investigating dissociation dynam-
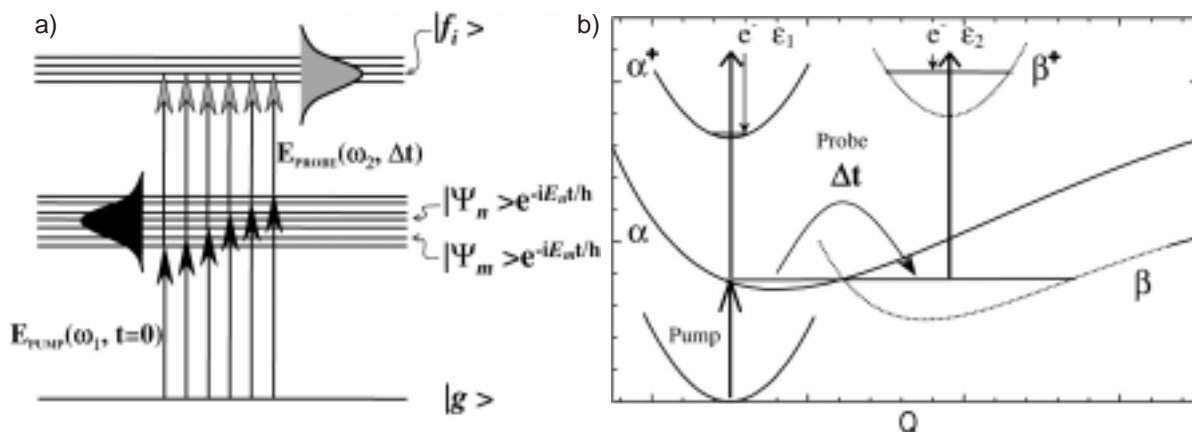
Figure 2.10: The pump probe excitation scheme. a) The pump laser pulse creates a coherent superposition of excited $|\Psi_k>$ states at $t = 0$. Then at time Δt the wavepacket is projected by a probe pulse onto a set of detectable final states $|f_i>$. [63] b) Pump-probe detection scheme of an adiabatic coupling process via photoelectron spectroscopy. A wavepacket is prepeared by a femtosecond laser pulse upon an electronic state α which converts to highly excited vibrational levels of a lower lying electronic state β. The two states ionize into different electronic continua α^+ and β^+ due to the Koopman's type correlation. [63]

ics of molecular systems, where the fragmentation dynamics is taking place upon the transient state. The method of photoelectron spectroscopy is rather employed to investigate intramolecular configuration changes, like isomerization, proton-transfer, adiabatic passages to different electronic states and others. In Fig. 2.10, a schematic pump-probe scheme is depicted, utilizing photoelectron spectroscopy for monitoring the dynamics of a non-adiabatic coupling process (adopted from [63]). There, a wavepacket is prepared upon an electronic state α by a femtosecond pump laser pulse which via a nonadiabatic process eventually converts to a vibrationally excited lower lying electronic state β. The two states will then ionize via one photon absorption of the probe laser pulse into the electronic continua α^+ and β^+. An elementary but rather useful picture involving the correlation of the neutral intermediate states α and β to the different cationic configurations is provided by the so-called *Koopman's theorem*. This simple correlation rule indicates that the cation state is expected to be formed upon single photon, single active electron ionization of a given molecular orbital. Partial ionization probabilities into specific cation electronic states can therefore differ drastically with respect to the molecular orbital nature of the neutral electronic states. According to this approach, when the wavepacket has an α-state character, its vibrational dynamics will be reflected in the structure of the ε_1 photoelectron band. After the nonadiabatic process, the wavepacket has a β-state electronic character and its dynamics will be reflected in the ε_2 band.

Following the coherent nuclear motion of the molecule, initiated by the pump-pulse, the opportunity for control arises when the probe laser pulse is fired at a time when the wavepacket is visiting a nuclear configuration, preferentially associated to the desired final state. In the general case, by carefully applying laser pulses with the appropriate frequency, intensity, duration, and timing it is possible to enhance and generally control chemical reactions [64], like in the case of photodissociation of a molecule. There, an unstable dissociating potential can be employed as transient state [10, 65–67] and the breaking of the molecule can be controlled. A theoretical approach of the pump-probe scheme was initially introduced in 1986 by Tannor, Kosloff, and Rice [68, 69]. They also proposed a control scheme utilizing the so-called *Pump-Dump* scheme. This is achieved in two steps, too. With a first pulse, the ground-state population is promoted to a suitable excited state and propagates upon the excited state. Then the second pulse arrives and the wavepacket is transferred downwards onto a different region of the ground state, which in certain cases cannot be directly reached from the initial configuration on the ground state, like in the case of the ethylenic isomerization (Section 2.3.4).

2.4.2 Quantum interference - The Brumer-Shapiro control scheme

One of the central concepts in quantum mechanics is the quantum interference, when the transition from an initial to a final quantum state is realized via more than one excitation pathways. In 1986 P. Brumer and M. Shapiro [70] implemented this principle to demonstrate an applicable scheme for selectively controlling the laser photofragmentation of a model molecular system. To achieve the desired selectivity, the excitation scheme must comprise of an initial state, intermediate resonant states and at least two different final product states. The excitation from the well-defined initial state to the degenerate product states is realized via two independent paths. For instance, the system may exhibit two different dissociating final electronic states that can be reached via an one-photon as well as via a three-photon excitation [71].

The initial state is a bound eigenstate of molecular Hamiltonian with energy E_i , and the final is a continuum state with energy E. Suppose that the system is irradiated with two electromagnetic fields:

$$E(t) = E_1 cos(\omega_1 t + k_1 r + \theta_1) + E_3 cos(\omega_3 t + k_3 r + \theta_3), \tag{2.37}$$

where $\omega_3 = 3\omega_1$. The two laser fields are assumed to have the same polarization vector, therefore a scalar representation is rather utilized. Let $k_3 = 3k_1$, corresponding to

parallel incident fields. The probability of forming a product in channel q with energy E is given by:

$$W(E, q; E_i) = W_3(E, q; E_i) + W_1(E, q; E) + W_{13}(E, q; E_i), \qquad (2.38)$$

where $W_a(E, q; E_i)$, $a = 1, 3$ are the transition probabilities corresponding to one-and three-photon absorption, respectively. $W_{13}(E, q; E_i)$ is the interference term between the one- and three-photon channels. In the weak field limit, the branching ratio for formation of products in exit channels q and q' is given by:

$$R_{qq'} = \frac{|E_3|^2 F_3^{(q)} - 2|E_3||E_1|^3 cos(\theta_3 - 3\theta_1 + \delta_{13}^{(q)})|F13^{(q)}| + |E_1|^6 F_1^{(q)}}{|E_3|^2 F_3^{(q')} - 2|E_3||E_1|^3 cos(\theta_3 - 3\theta_1 + \delta_{13}^{(q')})|F13^{(q')}| + |E_1|^6 F_1^{(q')}}, \qquad (2.39)$$

where,

$$F_3^{(q)} = (\frac{\hbar}{\pi|E_3|})^2 W_3(E, q; E_i) \qquad ; \qquad F_1^{(q)} = (\frac{\hbar}{\pi|E_1|})^2 W_1(E, q; E_i), \qquad (2.40)$$

and similarly for q'. Both the numerator and denominator of Eq. 2.39 obtain a sum of contributions from the independent one- and three-photon channels and an interference term. The later can be controlled by changing the relative phase of the one- and three-photon channels $(\theta_3 - 3\theta_1)$ and their relative amplitudes. Consequently, the product ratio R$_{qq'}$ can be controlled. The principle of this scheme can be compared to the Young double slit experiment.

The first experimental demonstration of this method came from Chen Ce and Elliott [73, 74]. The key idea of interference between two independent quantum channels has led to extensive experimental and theoretical studies of what has now been established as *phase-sensitive coherent control*. The ability to drive a molecular or atomic system is proved to be a valuable tool in the study of laser-molecule and laser-atom interactions. Coherent control methods are applied extensively in manipulating excitation processes and ionization rates, ionization and dissociation branching ratios, autoionization line shapes, angular distributions of photo absorption products as well as to generation of harmonics [75–84]. From the above, the experimental work by Gordon and co-workers [77] is of particular interest. They excited a beam of DI molecules [78] with one photon of 117.90 nm and three photons of 353.69 nm. The excited molecules decay either by autoionization, to produce DI$^+$, or by predissociation, to produce a ground state D atom and an electronically excited I atom. In the second case the I atom can absorb additional photons to produce I$^+$. As the phase between the two laser beams was increased, the ion signals varied periodically (Fig. 2.11b). The most important point is that the two
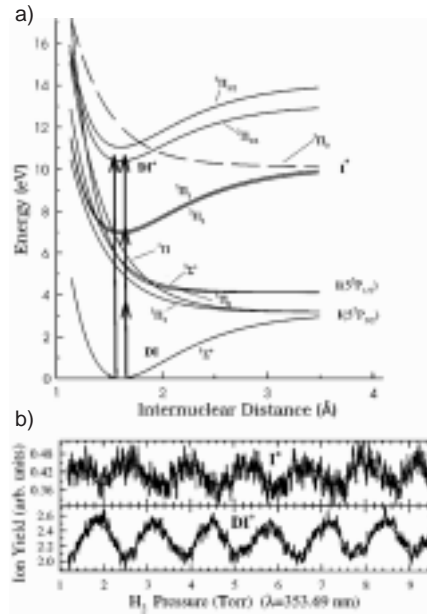
Figure 2.11: Two color phase-control utilizing the third harmonic laser field. a) Energy diagram of the control scheme realized by Gordon et.al. [78] on the molecular dissociation of DI. b) The resulting ionization signals of the I^+ fragment and the ionized molecule DI^+ as a function of the relative phase between the excitation laser fields.

oscillating ion signals differ with respect to each other by a constant phase lag $\Delta\delta$. In this way, the ratio of I^+ to DI^+ could be controlled by varying the phase difference between the two laser fields. Further investigations by Gordon et.al. [78] revealed the dependence of the phase lag on the final state energy. He addressed this effect to the presence of an autoionizing resonance.

The above phase sensitive control scheme can be generalized in excitation schemes, utilizing femtosecond laser radiation. There, quantum interferences can occur between the spectral components of the broad laser bandwidth. One example is depicted in Fig. 2.12, involving the two-photon electronic transition from an initial state $|i>$ to a final state $|f>$. The transition to $|f>$ is realized via absorption of two photon of the central frequency $\omega_\circ$ of the pulsed laser field, or by other photon combinations like: $\omega_1 + \omega_2$ and $\omega_2 + \omega_1$. Therefore, the specific modulation of the spectral phase of the laser field can induce constructive or destructive interferences between the multiple excitation channels and provides a flexible method for controlling the electronic transitions [85–87]. Supposed that the final state $|f>$ is embedded in a diversity of closely spaced energy levels, like in a molecular resonance or an atomic Rydberg manifold, the above scheme can be employed to selectively excite a specific state or to prepare a coherent superposition of states with the desired amplitude and phase parameters.
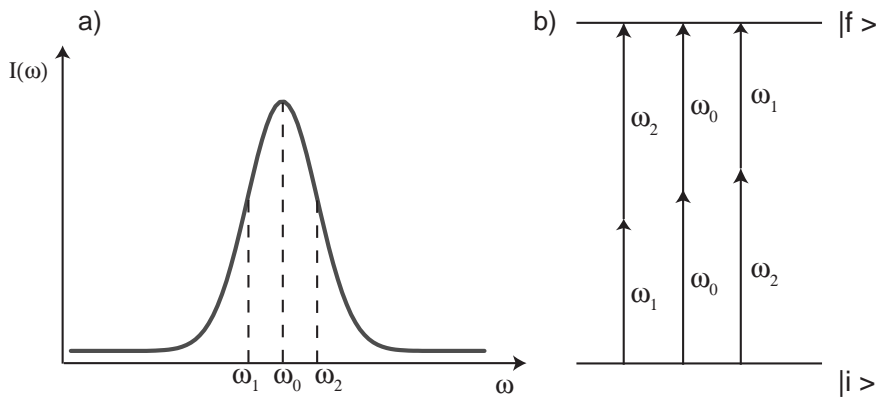
Figure 2.12: Single pulse phase-control of a model two photon femtosecond excitation scheme. The energy levels $|i>$ and $|f>$ are coupled via multiple combinations of photon with different frequencies within the broad spectral bandwidth of the excitation pulsed laser field b). The quantum interference between the multiple excitation pathways offers the opportunity of controlling the electronic transition, by modulating the spectral phase of the femtosecond laser pulse.

3 Experimental Realization

3.1 Overview

In the present chapter, a number of experimental methods are presented by which femtosecond time-resolved and laser-control spectroscopic studies were carried out in this thesis. For this purpose a combination of the following three experimental techniques was employed:

- The femtosecond laser system

- The time-of-flight spectrometer

- The molecular beam setup

The femtosecond laser system delivers pulses of typical duration of 90 fs. For pump-probe experiments, a Mach-Zehnder interferometer was used to transform single laser pulses into pairs of pulses with a controllable time-delay between them. Additional techniques were employed to modify the frequency and temporal characteristics of the femtosecond laser field, as summarized in Section 3.2. There, among others, the properties and principles of operations of the so-called "pulse-shaper" are presented. This optical arrangement allows for a computer controlled modulation of the spectral profile of (non-ultraviolet) laser pulses. The pulse-shaper is addressed by an evolutionary algorithm (Section 3.5.3) which adaptively adjusts the laser pulse in order to optimize a given outcome of a laser excitation process.

Two detection schemes were used to gain insight into the laser interactions of atomic and molecular systems, namely mass- and electron- spectroscopy. Both methods are based upon the principle of the time-of-flight scheme. The information about the mass- and charge-state of the ions or the kinetic energy of the emitted electrons, respectively, is experimentally acquired by measuring the time in which the generated charged particle, ion or electron, span a field free area and register on the detector. In this concept, two

different types of mass-spectrometer as well as two types of electron spectrometer are presented in Sections 3.3.1, 3.3.3 and 3.3.4. The basic aspects of the electronics, used to acquire, digitize and process the signals from the spectrometers are addressed in Section 3.5.

The analysis of atomic and molecular dynamical processes is considerably simplified when the sample particles are investigated under low pressure (collisionless) conditions. By use of the so-called "molecular beam" arrangement it is possible to prepare the atomic or molecular sample, so that in a well localized manner, an assembly of it's particles can collinearly propagate inside a high vacuum environment. The principles as well as the advantages and critical design parameters of the molecular beam arrangement are discussed in Section 3.4.

3.2   Optical Setup

3.2.1   Femtosecond laser system

The source that generates the femtosecond laser pulses is a Ti:Sapphire oscillator. It's active laser medium is a sapphire crystal doped with Ti^{3+} ions, which absorbs in a broad band region centered around 500 nm. The interaction between the doped Ions and the host crystal results in a broad band laser transition around 800 nm [88,89]. The coupling between the longitudinal modes, necessary for the pulsed operation of a laser, is accomplished via *Kerr-Lens-Modelocking* [3,90]. The optical pumping of the Ti:Sapphire laser is realized by focusing the beam from an Argon-Ion Laser into the sapphire crystal. The laser operation of the oscillator induces a gradient of the field intensity inside the crystal. This causes a spatial variation to the nonlinear part of the refractive index of the crystal (self focusing) and the pulsed-mode operation of the oscillator prevails over the continuous-wave (cw) operation. To compensate for the material dispersion, which would result in the substantial broadening of the femtosecond pulses, the Ti:Sapphire oscillator is equipped with a LaKl21-Prism compressor. The output of the oscillator is a femtosecond pulse train with a repetition rate of 80 MHz. Each laser pulse has an energy of around 4 nJ, and a time duration of 50 fs. This energy is however too low to reach the field intensities necessary to study atomic and molecular multi-photon transitions. The required amplification of the laser pulses is realized following the standard method of *Chirped Pulse Amplification* (CPA) [91,92]. For this, a commercial amplification system, manufactured by the company Quantronix and further modified by A. Assion [93], was employed. Before the laser pulses are coupled into the amplifier, their time duration
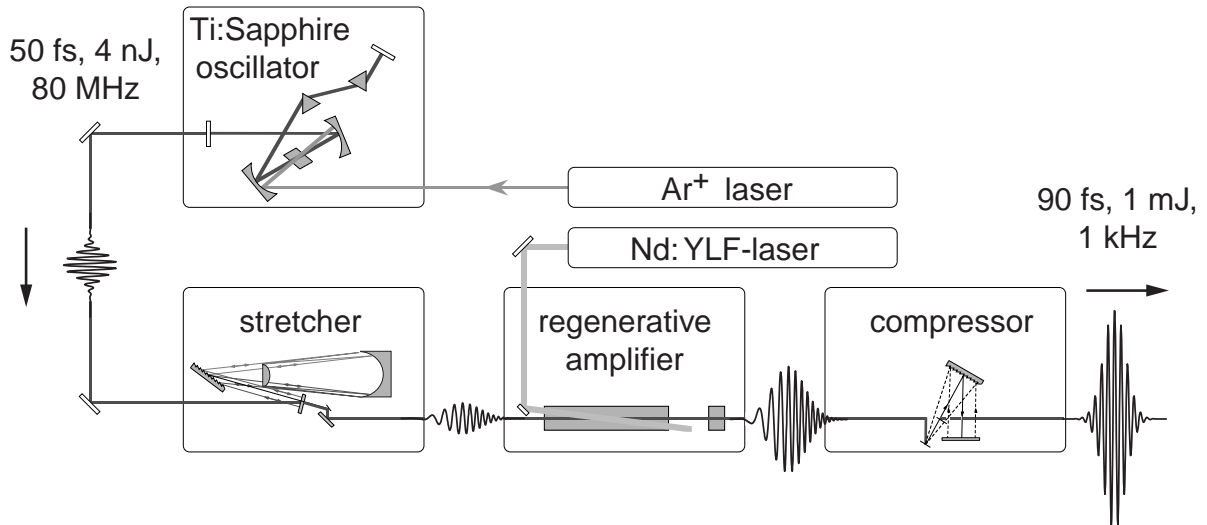
Figure 3.1: Overview of the femtosecond laser system. The ultrafast 800 nm laser pulses are generated at high repetition rate by a Ti:sapphire oscillator. After their temporal stretching, the pulses are subsequent to additional amplification at a lower repetition rate. The amplified laser pulses are finally recompressed to a 80 fs pulse duration. This three steps amplification technique is known as *Chirped Pulse Amplification* (CPA).

is stretched by a factor 10^3, to avoid the damage of the numerous optics components inside the amplifier from the high peak intensity of the laser pulses. The amplification medium is also a Ti:Sapphire crystal and is optically pumped by a pulsed Nd:Yag laser. The later delivers pulses of nanosecond duration and an energy output of 10 W in a 1 kHz repetition rate at 527 nm. In this arrangement, an amplification factor 10^6 is achieved in expense of a lower repetition rate. The amplification is realized within 10 round trips of the pulses inside the amplifier cavity. After that, the laser pulses are coupled out of the cavity by means of polarization selective optics. The optimal timing between the optical pumping of the amplifier and the coupling of the laser pulses in and out of the cavity is achieved via an electronic control unit (MEDOX). Finally, the laser pulses are compressed back to a duration of 90 fs. This is relatively longer than that of the oscillator pulses due to the effect of *Gain Narrowing* [94]. The energy of each laser pulse is now 1 mJ. The central wavelength of 800 nm is preserved.

3.2.2   Frequency conversion methods

In Section 3.2.1, the generation of 800 nm femtosecond laser pulses was described. However, for many experiments in this thesis, pulses of ultraviolet (UV) laser radiation were necessary. Their generation is possible by means of non-linear optic techniques [95,96] which convert the 800 nm laser radiation into shorter wavelengths (and therefore higher
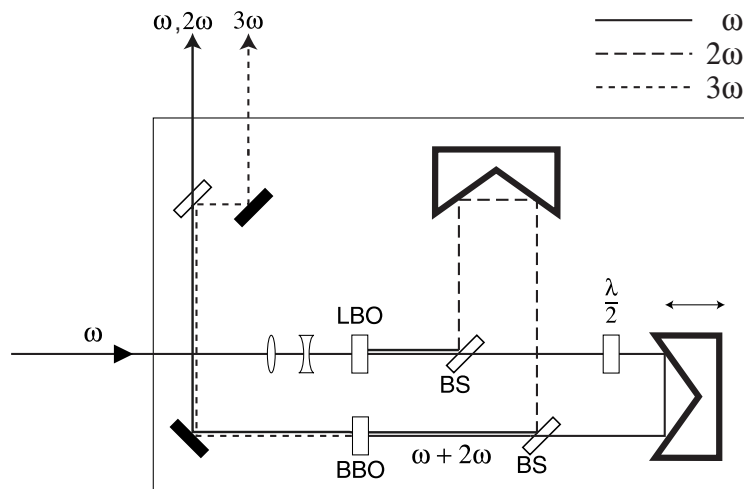
Figure 3.2: Schematic representation of the laser beam path inside the Tripler. By means of a doubling LBO-crystal 400 nm laser pulses are generated via SHG. They are mixed (SFG) with the remaining 800 nm pump laser radiation inside a BBO-crystal, by which the third harmonic laser field (266 nm) is generated. A Mach-Zehnder interferometer is employed to optimize the temporal overlap of the 800 nm and 400 nm laser pulses in the mixing process.

photon energies). By frequency doubling in a Beta-Bariumborat (BBO) crystal, the central wavelength of the laser field can be converted to 400 nm (*Second Harmonic Generation*–SHG) [96, 97]. Due the material dispersion inside the optical medium, the thickness of the BBO crystal was only 0.1 mm. The SHG conversion efficiency is around 10%.

Laser pulses of even shorter wavelength, namely 266 nm (*third harmonic generation*– THG) can be generated by the optical setup depicted in Fig. 3.2. First, the diameter of the 800 nm laser beam is reduced with a telescope and the second harmonic is generated in a 0.1 mm thick LBO crystal. The two laser field, the second harmonic (400 nm) and the remaining fundamental (800 nm), are then separated by means of a dichroic mirror, which selectively reflects the 400 nm radiation, and guides it toward one arm of a Mach-Zehnder interferometer. Then, the 800 nm and 400 nm pulses are incident on a second dichroic mirror and recombine. The Mach-Zehnder interferometer allows for an optimal temporal overlap of the two laser pulses. Finally, the two pulses pass through a 0.3 mm thick BBO crystal and the third harmonic laser field (266 nm) is generated by *Sum Frequency Mixing* (SFM). Both crystals meet a Type-I phase matching condition i.e. the polarization of the incidence laser radiation must be parallel to the optical axis of the crystal. However, in the process of SHG the polarization of the generated harmonic is perpendicular to the that of the fundamental 800 nm radiation. To match the vectors
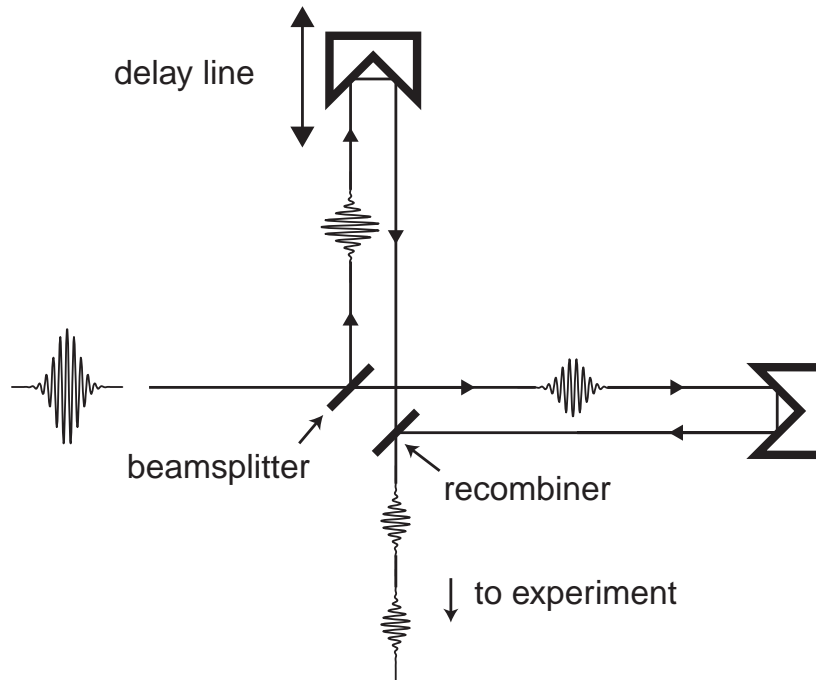
Figure 3.3: Schematic representation of the pump-probe optical arrangement. The in-going 800 nm femtosecond laser pulse is split with a 50 % reflectivity mirror (beam splitter) into two identical pulses. These pulses propagate upon the arms of a Mach-Zehnder interferometer and recombine upon incidence on a second 50 % reflectivity mirror. The temporal distance between the laser pulses is controlled with a computer-addressed translation stage, installed in one arm of the interferometer.

in SFM, the polarization of the 800 nm field is rotated by a $\lambda/2$ plate after the frequency doubling. From now on, the optical arrangement employed for generating 266 nm laser pulses will be referred to as the "tripler". Assuming an optical pumping with 800 nm laser pulses of 90 fs duration and 1 mJ energy, the typical output of the tripler is 80μJ for the second harmonic field (400 nm) and 30 μJ for the third harmonic field (266 nm). The two laser fields as well as the remaining part of the fundamental 800 nm exit the tripler collinearly and can be separated by means of the appropriate dichroic mirrors.

3.2.3   Pump-probe setup

The pump-probe technique is one of the fundamental methods for studying ultrafast molecular dynamics. It involves a pair of excitation laser pulses (pump- and probe-pulses) which can be delayed with respect to each other in a controllable manner. This concept is fulfilled by employing a Mach-Zehnder interferometer, as shown in Fig. 3.3. A mirror of 50 % reflectivity (beam splitter) divides the initial femtosecond laser pulse into two identical pulses. One arm of the interferometer is installed on an adjustable

translation stage. The geometrical paths upon the two arms of the interferometer result in different flight-times for the two laser pulses. Finally, a second beam splitter recombines the two delayed laser pulses. The translation stage is controlled by a DC-motor (Aerotech, Unidex 100/1035DC) with a precision of 1 fs. Due to the two reflections upon the 50 % reflectivity beam splitters, the energy content of each of the outgoing laser pulses is 4 times less than that of the in going laser pulse.

3.2.4   Femtosecond laser pulse Shaping

The fist pulse shaping technique of picosecond laser pulses was introduced in 1983 by Froehly et. al. [99]. The method was further developed by J. Heritage, A. Weiner and coworkers [100, 101] who used this techniques for modulating femtosecond laser pulses. The later design is employed also in the present work for modulating 800 nm laser pulses. As previously mentioned (Section 2.1), a femtosecond laser pulse can be fully described in terms of a spectral amplitude $E(\omega)$ and a spectral phase $\Phi(\omega)$, the modulation of which results in a change of the time profile of the laser pulse. In Fig. 3.4 a schematic representation of the pulse-shaper is shown. It comprises two holographic gratings located at the focal point of two plano-convex cylindrical lenses with 80 mm focal length. After incidence on the first grating, the spectral components of the femtosecond laser pulses are analyzed. Then, they are focused by the first lens on the fourier plane of the setup, where a commercial Liquid Crystal Display is located. Finally, the laser spectrum is recombined by a second lens-grating pair. The transmission of the setup is around 70%. The Liquid Crystal Display (LCD) comprises of 128 rectangular pixels with an active width of around 97μm and a height of 2 mm. The beam diameter of the laser is reduced with a telescope, to match the pixel height. The distance between two successive pixels is 3μm. By applying a voltage on a pixel of the LCD the orientation of the liquid crystal molecules changes. Accordingly, the refraction index for vertical polarized light changes, as well as the optical path of the frequency component which propagates through the pixel. A $\lambda/2$ plate is positioned just before the LCD to rotate the polarization of the incident laser by 90°. This is necessary since the highest reflectivity of the grating is for horizontal polarization and the refraction index of the liquid crystal pixel changes only for vertical polarization. A second $\lambda/2$ plate is located after the LCD to rotate the polarization back to horizontal. The optical paths of 128 different frequency components can be individually controlled and the spectral phase of the laser pulse can be modulated. In this configuration, apart from the energy reduction, the
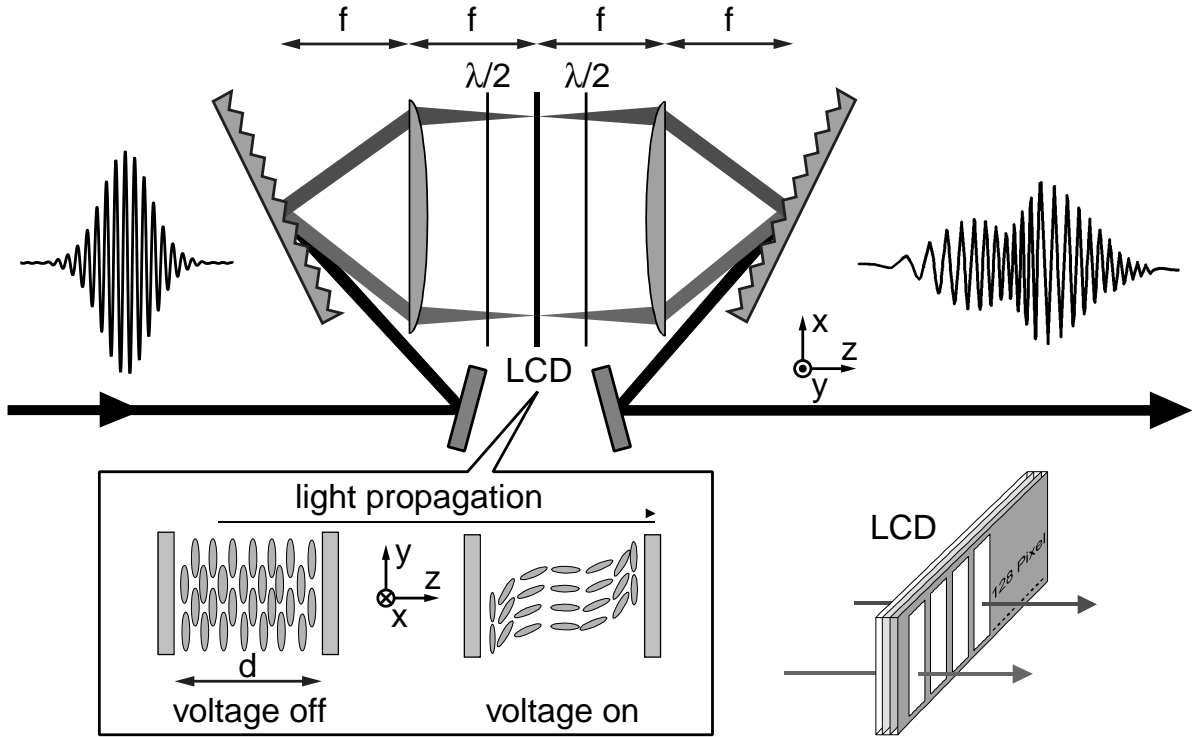
Figure 3.4: Schematic arrangement of the femtosecond LCD-pulse shaper. A liquid-crystal display (LCD) is located in the symmetry plane of a zero-dispersion $4f$-compressor. The refraction index of the individual LCD pixels can be adjusted by an electric field, which induces the partial reorientation of the liquid-crystal molecules in the pixels.

spectral amplitude of the laser field is not altered. The electric voltage of the individual pixels is applied with an accuracy of 12 Bits via a computer addressed controller. The reaction-time of the LCD is 150 ms. This is the time that the liquid crystal molecules require to reorient themselves. A detailed description of the pulse shaper as well as the wavelength and voltage calibration is found in the diploma thesis of T. Brixner [102] as well as in the PhD thesis of V. Seyfried [103].

3.2.5   Pulse-shaping of the third harmonic (266 nm) laser field

The use of the liquid crystal display (LCD), described in the previous section, is restricted to modulation of laser fields in the near infrared (NIR) and Visible (VIS) spectral range. This is due to the limited transparency of the liquid crystals as well as that of TiO_2, which is used as a transparent electrode to apply the voltage on the pixels of the display. The shaping of ultraviolet (UV) laser pulses is rather achieved by use of frequency up-conversion methods. Initially the modulation of laser pulses is realized at a spectral region where the LCD can be operated. Then, the generated pulse shape is transferred
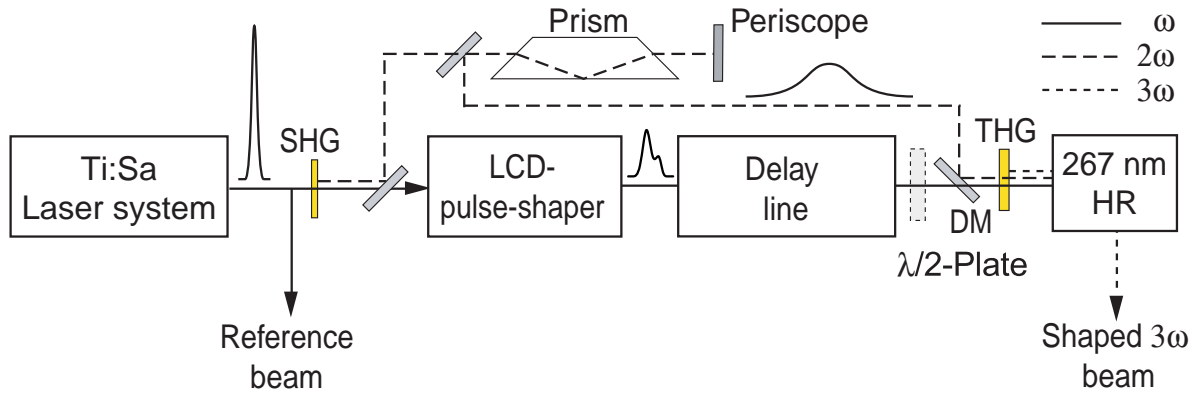
Figure 3.5: Schematic arrangement of the indirect shaping of 266 nm laser pulses. The second harmonic 400 nm field is generated before the LCD-pulse-shaper and guided through a thick dispersive material (Dove-prism). The remaining 800 mn field is shaped and recombined with the temporally stretched 400 nm field. Then, the two laser fields are mixed inside a 300 μm thick BBO-crystal. The generated 266 nm field is finally filtered by multiple reflections upon dichroic reflectors.

to the UV by means of a frequency mixing process. A direct frequency conversion of modulated 800 nm laser pulses with the tripler (Section 3.2.2) results in a rather poor conversion efficiency. This is due both to the lowering of the peak intensity when the laser pulses are modulated and to the third-order intensity dependence of the third-harmonic-generation process. To overcome this problem, an optical arrangement was developed, by which the shaped 800 nm laser pulses are mixed with unmodulated 400 nm laser pulses. In this arrangement, the reduction of the peak intensity of the shaped pulses is linearly transferred to the signal of the generated third harmonic. This concept was first realized in the group of E. Riedle [104]. A similar but rather simpler setup was developed in our lab for the purposes of adaptive control experiments on photoisomerization reactions, nicely summarized in the diploma thesis of P. Nürnberger [105]. One important consideration concerning the mixing process is that the unmodulated 400 nm has to be relatively long in time. The modulated 800 nm pulses often gain a duration spanning over many picoseconds, while the duration of the 400 nm laser pulse practically defines the time window where the pulse shape of the 800 nm field can be modulated and still be frequency up-converted.

Following the above considerations, the optical arrangement used for indirect shaping of the 266 nm laser pulses is depicted in Fig. 3.5. The second harmonic 400 nm field is generated in a 100 μm thick doubling LBO-crystal and separated from the fundamental 800 nm field, which is then coupled into the LCD-pulse shaper. In order to acquire the desired long pulse duration of the second harmonic field, a 13 cm long Dove-prism,

already available in our laboratory optics collection, was employed. The choice of the specific optical component serves no other purpose than to disperse the propagating laser field. The 400 nm pulses are then reflected backwards, parallel to the incoming beam but at 1 cm lower height, with a periscope. The estimated optical path through the Dove-prism is 20 cm, which is well suited to stretch the second harmonic pulses up to 1,5 ps. A detailed discussion about the influence of the Dove-prism on the phase of the laser field is found in [105]. Finally, the modulated 800 nm pulse recombines with the stretched 400 nm pulses by means of a dichroic reflector (recombiner) and the two laser fields are coupled into a 300 μm thick sum-frequency-mixing BBO-crystal. As in the case of the tripler, the polarization vectors of the mixing laser fields are matched by inserting a $\lambda/2$-plate before the recombiner. The temporal overlap between the two pulses is adjusted with a variable delay line. After the frequency mixing, the generated 266 nm laser pulses are separated from the remaining 800 nm and 400 nm fields by multiple reflections upon dichroic reflectors. A small portion of the initial 800 nm field is reflected and, as explained later, is used as reference to characterize the structure of the modulated 3ω pulses.

3.2.6   Laser pulse characterization

In sections 3.2.4 and 3.2.5, the technique of pulse shaping was presented. In the following, a number of experimental methods is described, by which the structure of complex femtosecond pulses can be characterized. Since no electronic device is so fast, the characterization of femtosecond pulses relies on optical methods. During the last decade, a wide variety of methods have been introduced for the characterization of complex laser pulses both in the time as well as in the frequency domain. In these techniques, the unknown laser pulse interferes with a second reference femtosecond pulse. The created interference pattern is then detected by means of conventional "slow" detectors (photo-diodes, CCD-cameras etc.) to reveal the structure of the analyzed laser pulse. In this concept, the most important development is the method of *Frequency Resolved Optical Gating* (FROG) [106, 107] which is mainly used in this work.

To introduce the fundamental concepts of the FROG technique, a short description of the so-called autocorrelation method is first presented. In the autocorrelation method, a femtosecond laser pulse is split in two identical pulses, as in the pump-probe arrangement. The two pulses are delayed with respect to each other and finally overlapped inside a SHG crystal, as shown in Fig. 3.6. The dependence of the generated second
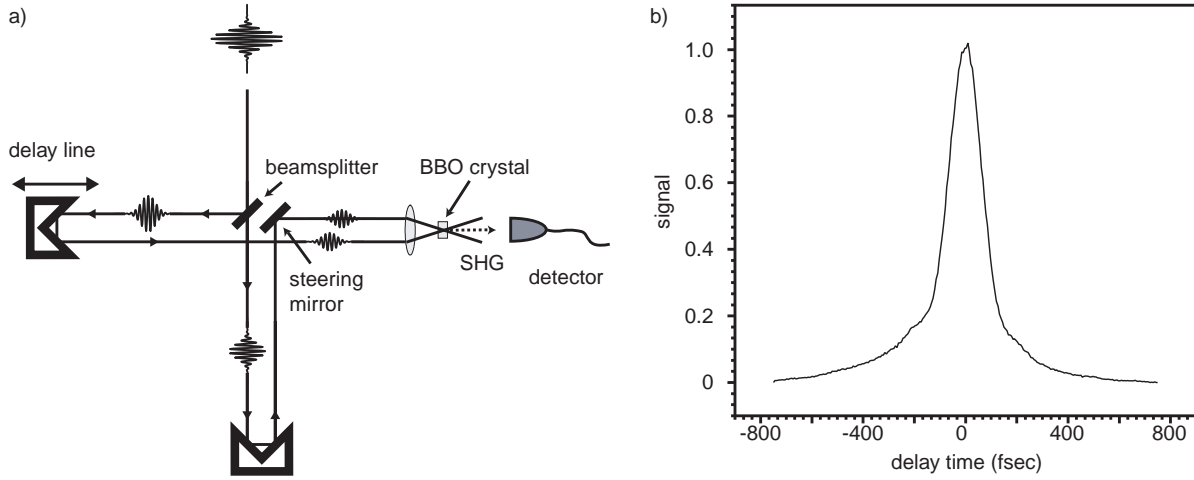
Figure 3.6: Schematic representation of the autocorrelation technique. a) The analyzed laser pulse is split into two identical pulses, which are delayed with respect to each other and finally recombined inside a SHG-crystal. b) The signal of the generated second harmonic field is measured as a function of the delay time between the two pulses.

harmonic signal on the time delay time τ between the two pulses, is described by the second order autocorrelation function [108]:

$$A(\tau) = \int\limits_{-\infty}^{\infty} I(t) \cdot I(t-\tau)dt, \qquad (3.1)$$

which is symmetric with respect to the variable τ. The exact structure of the laser pulse cannot be fully acquired by this measurement. Nevertheless, the time duration of the laser pulse can be retrieved by fitting the measured trace with a model autocorrelation curve. For bandwidth-limited or linearly chirped laser pulses a Gaussian function or a quadratic hyperbolic secant ($sech^2$) are commonly used for this purpose. The FWHM of the model autocorrelation curve can then be correlated to the FWHM of the measured autocorrelation trace [108].

As already mentioned, to analyze a complex laser pulse a second reference (gate) pulse is necessary. In the autocorrelation method an identical copy of the analyzed pulse itself serves this purpose. The same concept is employed in FROG. But, instead of monitoring the integrated second harmonic signal, the analyzed spectrum $I(\omega)$ of the generated harmonic field is rather recorded as a function of the delay time. The measured signal is a function of two variables, the delay time τ and the frequency ω of the generated second harmonic.

a) wavelength / time

b) temporal intensity I(t) / temporal phase Φ(t) / rad — time / fs (-400, -200, 0, 200, 400)
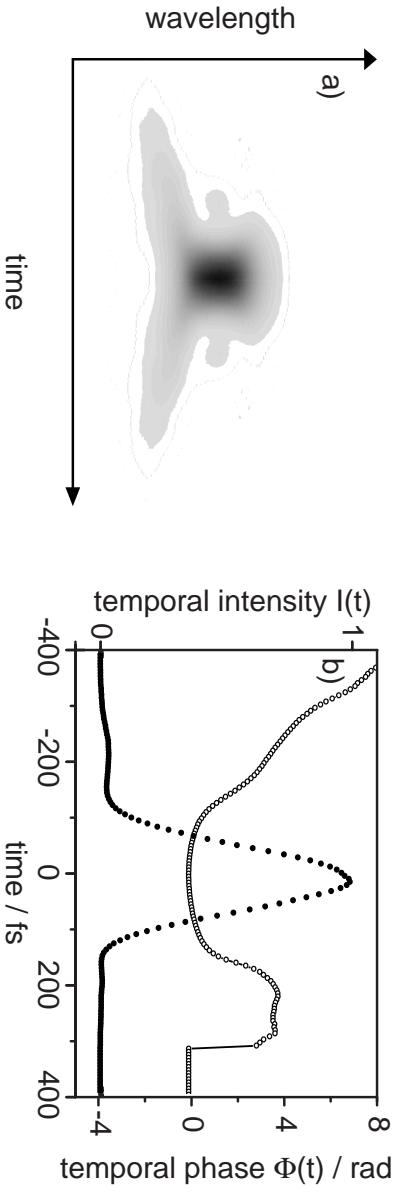
Figure 3.7: Characterization of a femtosecond laser pulse with FROG. a) The measured $I_{FROG}(\omega,\tau)$ signal and b) the retrieved intensity and phase function of femtosecond laser pulse.

The two-dimensional FROG signal can be analyzed by means of an iterative algorithm [110, 111]. In the so-called FROG-algorithm, the $I_{FROG}(\omega,\tau)$ function of a theoretical electric field $E(t)$ is calculated and compared to the measurement. The test electric field is then altered [112] and again tested in an iterative manner until the deviation from the measured $I_{FROG}(\omega,\tau)$ function reaches a desired error limit. In this way, the amplitude and phase information of the analyzed laser pulse can be fully acquired. An example of a complex 800 nm laser pulse analyzed with SHG-FROG is presented in Fig. 3.7.

$$I_{FROG}(\omega,\tau) = \left| \int_{-\infty}^{\infty} dt\, E(t) E(t-\tau) e^{-i\omega t} \right|^2 \qquad (3.2)$$

The distinctive feature among them is the way that the temporal gating of the analyzed pulsed is realized. To characterize a complex UV laser pulse, like the 266 nm pulses described in Section 3.2.5, a frequency doubling process is not possible due to the lack of the appropriate SHG crystal for this spectral region. However, the temporal gating can be realized by means of an independent (but always coherent to the analyzed pulse) reference 800 nm pulse. In this so-called X-FROG scheme [113], the measured signal results from the *Difference Frequency Mixing* (DFM) of the analyzed 266 nm field with the reference 800 nm laser pulse. The spectrum of the generated 400 nm laser field is again analyzed and recorded as function of the delay between the two pulses, like in SHG-FROG.

Up to now, a number of variations of the FROG technique have been demonstrated.

$$I_{X-FROG}(\omega, \tau) = \left| \int\limits_{-\infty}^{\infty} dt E_{UV}(t) E_{Ref}(t - \tau) e^{-i\omega t} \right|^2 \qquad (3.3)$$

To retrieve the analyzed $E_{UV}(t)$ field, the $E_{Ref}(t)$ function of the reference laser pulse must be provided to the FROG algorithm. For this reason, the X-FROG method is combined with SHG-FROG to characterize the reference 800 nm laser field.

3.3   Spectroscopic methods

3.3.1   Time-of-flight spectrometry

Consider an interaction of a pulsed laser field where ions of mass m and electric charge q are produced. Then, the ions get accelerated by an electric voltage U and move across a field-free area of length L until they reach a charged particle detector. This arrangement is known as a linear *time-of-flight* (TOF) spectrometer [114]. The information about the mass of the generated ion can be acquired by measuring the time t_m that it takes for the ion to reach the charged particle detector and is summarized as follows:

$$m = \frac{2qU}{L^2} \cdot t_m^2 \tag{3.4}$$

In a similar geometry the electrons ejected during the laser interaction can also be detected. Since their mass is many orders of magnitude smaller than that of the corresponding ion, their kinetic energy, inherently acquired during the ionization process, is sufficient for the electrons to leave the interaction region and reach the particle detector. In this case the measured time-of-flight carries the information about the kinetic energy of the electrons.

3.3.2   The Wiley-MacLaren spectrometer

In Fig. 3.8 the linear time-of-flight spectrometer used for the experiments presented in Chapter 4 is depicted. It comprises a number of circular metal apertures coated with a graphite layer which allows the formation of smooth conducting surfaces and protects the metal against corrosion from aggressive molecular samples. A circular opening in the middle of each aperture allows for the transmission of the charged particles along the spectrometer axis. To maintain the uniformity of the applied electric fields, a thin Nickel mesh is fixed over each opening. The electric potential applied to each plate can be individually controlled. Using two different voltage configurations the detection of ions as well as electrons is possible. In both cases, the charged particle detection is realized by means of a *multi-channel-plate* (MCP) detector. In the ion-measurement configuration, the positive charged particles are initially accelerated towards the MCP detector. Following the design introduced by W. C. Wiley and I. H. MacLaren [114], before the ions enter the field free area an additional aperture (without a Nickel mesh) is used to spatially focus the ion bunch.
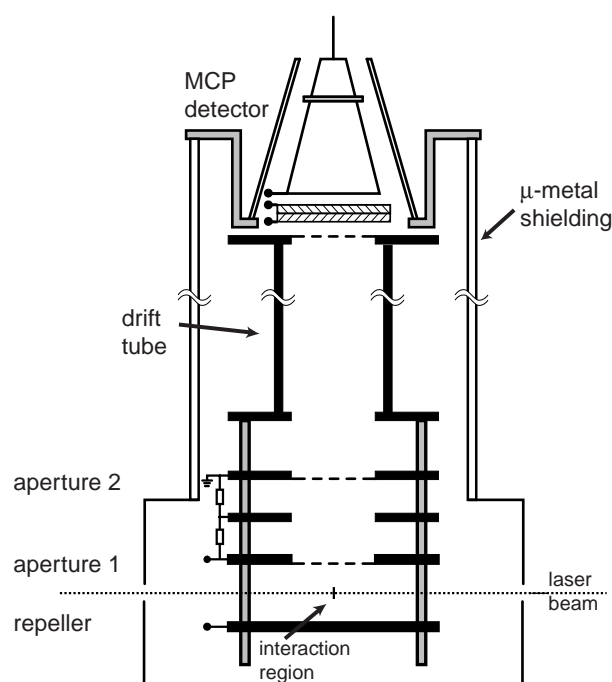
Figure 3.8: The Wiley-MacLaren time-of-flight spectrometer. The detection of ions as well as of electrons is possible by means of two different configurations of the voltages applied to the various contacts indicated with small black filled circles. For ion detection, two acceleration areas a) between aperture 1 and the Repeller and b) between aperture 1 and 2 are employed. The Wiley-MacLaren arrangement allows for the focusing of the generated ions at the upper position where an MPC-detector is located. For electron detection no extraction field is applied to the interaction region. After passing aperture 1, the electrons are accelerated with an additional 2 eV kinetic energy in order to improve the throughput of the spectrometer.

The factors that limit the resolution of a time-of-flight mass spectrometer are summarized below:

- The duration of the laser pulse

- The velocity distribution of the atomic-/ molecular-sample before the laser-interaction

- The finite size of the interaction area

When the duration of the laser pulse is relatively long (or comparable to the time-of-flight), the time at which an ion is detected does not depend on the drift-time only, but also on the time, within the pulse duration, at which the ion was generated. This results in a broadening of the measured mass-spectrum. Subsequently, the mass of the ion cannot be exactly measured since the generation-time of the ion is not experimentally defined with this experimental arrangement. However, the experiments presented in this thesis were performed with laser pulses, the duration of which lies in the fs-ps range. This is is many orders of magnitude shorter that the time-of-flight time-scale(μs), therefore the resolution of the spectrometer in this case does not deteriorate.

Another limiting factor for the resolution of the time-of-flight measurement is the non-zero velocity of the sample atoms/molecules before the laser-excitation. A broad distribution of the velocity component v_z along the TOF-axis results to an evident deviation from Eq. 3.4 and degrades the resolution of the acquired mass-spectrum. The width of the v_z distribution and the subsequent broadening can be treated by preparing the atomic/molecular sample in a collimated beam. This technique is addressed in detail in section 3.4.

The third factor that limits the resolution of a time-of-flight mass spectrometer is the finite size of the laser interaction region. Ions of a particular mass that are generated in different positions within the interaction region acquire different amounts of kinetic energy from the acceleration field. Eventually, this translates into different flight-times and into the broadening of the measured mass spectrum. In the Wiley-MacLaren TOF configuration, this problem is compensated for by employing two fields for the ion acceleration. The ions that travel a longer distance towards the detector acquire a higher kinetic energy. After a specific distance, they reach the ions that had an advanced starting position, but acquired less kinetic energy from the extraction field i.e the ions are practically focused. The MCP detector is positioned at this location and a mass resolution of around $\frac{m}{\Delta m} = 300$ is achieved in out TOF setup. The time-of-flight is then given by:

$$t = t_a + t_b + t_c, \tag{3.5}$$

$$t_a = \frac{2a}{\sqrt{U_a}} \sqrt{\frac{m}{2q}}, \tag{3.6}$$

$$t_b = \frac{2b}{U_b} \sqrt{\frac{m}{2q}} (\sqrt{U} - \sqrt{U_a}), \tag{3.7}$$

$$t_c = \frac{c}{\sqrt{U}} \sqrt{\frac{m}{2q}}. \tag{3.8}$$

where t_a, t_b and t_c are the times that ions spend inside the two acceleration areas and the field-free region, accordingly. A more detailed treatment of the above formalism is given in [115].

For the detection of electrons however, no extraction field is applied in the interaction region. Unlike the case of ions, the drift of the electrons towards the MCP detector can be easily disturbed by residual magnetic fields, due to their small mass. For this reason, the spectrometer is equipped with a double μ-metal shield. To increase the fraction of electrons that are transmitted through the field free drift tube, a negative voltage is applied to both, the aperture 1 and the repeller (Fig. 3.8). In this arrangement, an energy resolution of around 100 meV for electrons of 1 eV kinetic energy is achieved.

3.3.3   High resolution mass spectrometer - The reflectron

A significant improvement of the mass resolution is accomplished by combining the Wiley-MacLaren arrangement with an electrostatic ion mirror. This setup was introduced in 1973 by B.A. Mamyrin [116,117]. The ions incident on the electrostatic mirror experience a decelerating field and subsequently get reflected in the opposite direction by a second field. The most energetic ions penetrate deeper into the electrostatic mirror and travel a longer path. This constitutes a second focusing process by which the focal point of the Wiley-MacLaren arrangement is imaged onto the MCP detector. The required analysis and formalism is presented in [118]. With this combined geometry, a flight-path of almost 1 m is possible as well as an enhanced resolution of $\frac{m}{\Delta m} = 2000$. In the spectra presented in Fig. 3.9, the mass spectrum of the metallocene catalyst, investigated in Chapter 6, was measured with a) the reflectron spectrometer and b) the linear Wiley-MacLaren TOF. Due to the high resolution of the reflectron, the three peak pattern measured with the linear TOF is further resolved to reveal a multiple peak structure. This structure originates from the natural isotopes of zirconium, the catalytic active center of the molecule.
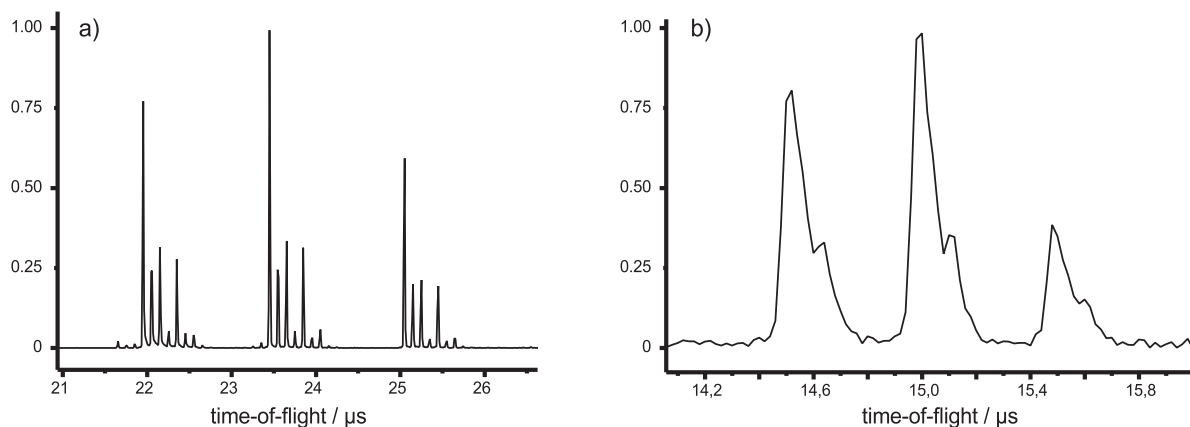
Figure 3.9: Comparison of the photofragmentation spectrum of a Metallocene catalyst measured a) with the reflectron and b) with the linear Wiley-MacLaren TOF. In the case of the reflectron, a multiple peak structure is resolved, corresponding to the natural isotopes of zirconium. This structure is not resolved with the linear TOF.

3.3.4   The magnetic-bottle electron spectrometer

In general the electron emission during a laser ionization process exhibits a rather complex angular distribution over a solid angle of 4π. With the Wiley-MacLaren TOF photoelectron spectrometer described earlier in this chapter, to retain the desired energy resolution in the acquired photoelectron spectra, only a small portion (5–10%) of the emitted electrons is transmitted along the spectrometer axis and is finally detected. To solve this problem, an alternative type of photoelectron spectrometer was developed in 1983 by Kruit and Read [119] and further improved by Cheshnovsky and Smalley [120], the so-called *Magnetic-Bottle Photoelectron Spectrometer* (MBPES). In the magnetic bottle a magnetic field is employed to collect a larger portion of the emitted electrons and guide them towards the electron detector. This is achieved with a combination of two separate magnetic field regions: a strong inhomogeneous magnetic field (1 Tesla), covering the laser interaction region, and a weaker homogeneous magnetic field (1 mTesla) (Fig. 3.10). In the strong-field region all the electrons emitted towards the upper 2π solid angle region are collected and guided to the detector. Then, the weak field is applied to direct the electrons along the 50 cm long flight-tube. Again, the information of the kinetic energy is contained in the time-of-flight of the electrons. Figure 3.10 shows an imaginary vertical cut along the magnetic bottle spectrometer axis. The current flowing through the solenoid magnet creates the weak magnetic field, while the inhomogeneous magnetic field is realized by means of a strong electromagnet, located at the lower part of the spectrometer. The desired field geometry is accomplished
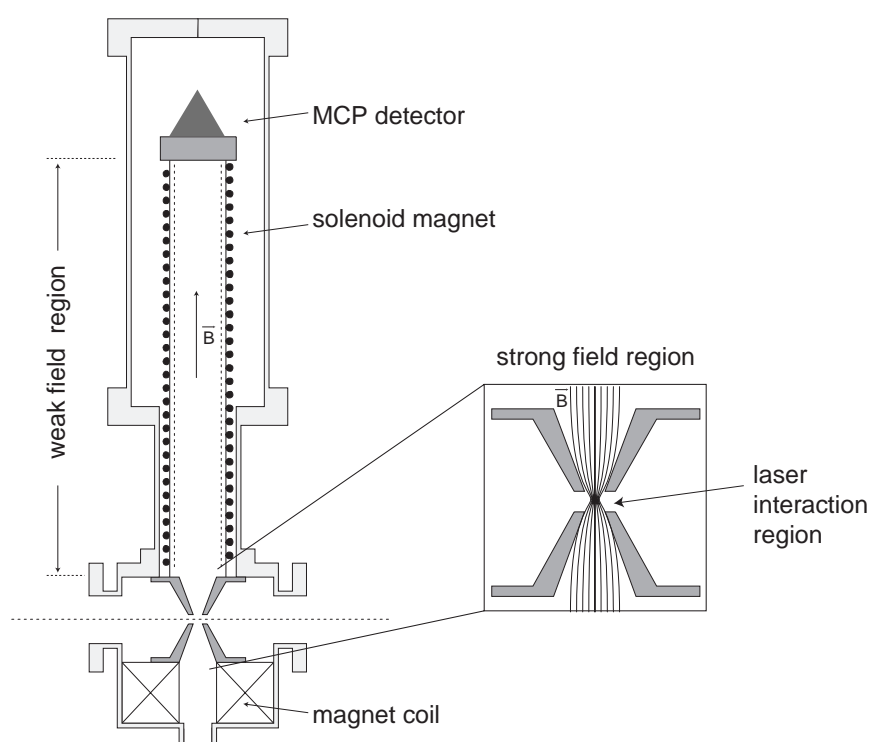
Figure 3.10: The magnetic bottle photoelectron spectrometer (MBPES). The high collection efficiency of the MBPES is achieved by the geometry of the field lines of a strong 1 Tesla magnetic field (see inset graph), induced in the interaction region by the strong electro magnet, located in the lower end of spectrometer. With this configuration, the upper 2π solid angle distribution of the emitted photoelectrons is collected and eventually guided to the MCP detector, on the upper end of the spectrometer. A week 1 mTesla magnetic field is additionally employed to direct the electrons towards the detector.

by means of a special stainless steel (St37) gasket design, equipped with two conical apertures shown in the right side of Fig. 3.10. Both the high collection efficiency of the magnetic bottle, as well as the oriented motion of the electrons along the drift region, allow for the construction of relative long flight distances. This enhances the energy resolution of the spectrometer to 30 mV, for electrons with kinetic energy in the 1 eV region.

3.3.5   Energy calibration of the photoelectron spectrum

The calibration of a photoelectron spectrum requires the definition of a function $E_{kin}(T)$, which transforms the measured time-of-flight electrons signal S(T) into a function $S(E_{kin})$ of the kinetic energy. In the ideal case where an electron drifts through a field-free region, the flight-time required to cover a distance L is given by:

$$T = L\sqrt{\frac{m_e}{2E_{kin}}} \tag{3.9}$$

In practice, the above equation is a very rough approximation and cannot be used exactly for the calibration, since the length of the flight tube is not known with the desired accuracy. Moreover, the original assumption of a field-free region is violated by the presence of weak external electric fields (static electric fields or contact potentials) that cause a significant deviation from the above expression. For this reason the $E_{kin}(T)$ function is expressed as a polynomial:

$$E_{kin} = c_0 + \frac{c_1}{T - T_{\circ}} + \frac{c_2}{(T - T_{\circ})^2} + \dots \tag{3.10}$$

$T_{\circ}$ is the time when the laser pulse is incident in the interaction region. Practically, the development up to the second order can adequately describe the calibration function. The reference time $T_{\circ}$ is directly measured by means of a fast photodiode. However, the constants c_0, c_1 and c_2 must be determined by fitting the calibration curve to a reference kinetic energy distribution. The accuracy of the calibration depends on the number of points used as reference for the fit. In regions where no reference signal is available, the $E_{kin}(T)$ function has to be extrapolated. To obtain the reference signal over a rather wide energy range, the well-studied photoelectron spectrum of atomic xenon [121,122] is employed. In Ref. [121,122] the laser field used for the multiphoton ionization of the atom has practically identical parameters (wavelength, pulse duration etc.) as the Ti:Sapphire used for the experiments in this work. For the ionization of xenon at least 8 photons of 800 nm central wavelength must be absorbed. Further absorption of additional photons
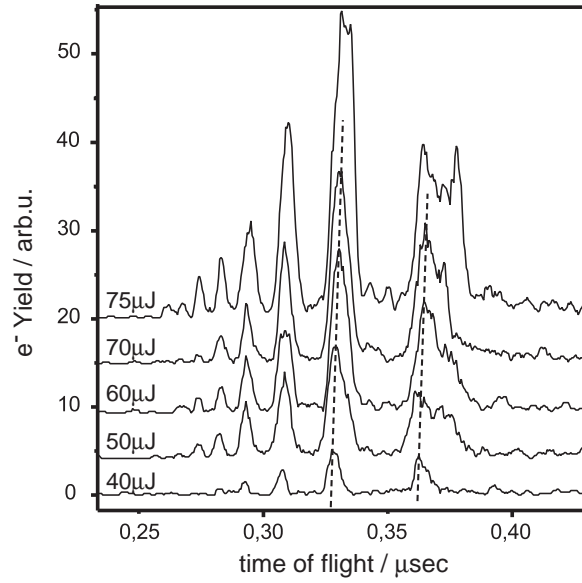
Figure 3.11: Above-threshold-ionization (ATI) spectra of atomic xenon, measured for different energies of the excitation pulses (40, 50, 60,70 and 75 μJ per pulse from the lower to the upper spectrum accordingly). The central wavelength of the laser field defines the constant energy distance between the successive ATI electron peaks. On the time-of-flight spectrum, due to the non-linearity of the E_{kin}(T), the spacing of the successive ATI peaks becomes narrower as the ATI order increases (from right to left). For the highest energy 75 μJ AC-Stark shifted resonances come into play.

gives rise to the ATI structure discussed in Section 2.2.3. The resulting photoelectron spectrum, measured with the Wiley-MacLaren TOF, is depicted in Fig. 3.11. The signal function S(T) was measured for five different energies: 40, 50, 60, 70 and 75 μJ per pulse. Notice that for time-of-flight spectra the electrons with higher kinetic energies take less time to reach the detector, since they drift with a higher velocity. Therefore, the ATI peak order increases from right to left. Also, due to the non-linearity of the E_{kin}(T), the spacing of the successive ATI peaks becomes narrower as the ATI order increases. To compare the different ATI spectra in Fig. 3.11 the following dynamical effect must be taken into account:

- The ponderomotive shift of the ionization threshold

- The intermediate atomic levels shifted into resonance due to the AC-Stark effect

As discussed in Section 2.2.2, the ponderomotive energy is the mean kinetic energy of a free electron in an electromagnetic field. The ponderomotive shift U_p has the same value, since when an atom is ionized the energy spent goes both, to the ionization and to the quiver motion of the electron. This is as if the ionization potential was increased

by the ponderomotive energy. A practical form of Eq. 2.16 for the calculation of U_p is given by:

$$U_p(in \;\; eV) = 9.3 \times 10^{-14} I_0(in \;\; W/cm^2)\lambda_0(in \;\; nm), \qquad (3.11)$$

In the above expression λ_0 stands for the central wavelength and I_0 for the peak intensity of the laser pulse. The shift toward longer time-of-flight, indicated also by the dotted lines in Fig. 3.11, is a manifestation of the kinetic energy loss of the emitted photoelectrons due to the ponderomotive shift. A direct assignment of a kinetic energy value to an ATI peak is therefore not trivial, since the peak intensity at the interaction region is not known (can only be estimated). On the other hand, if by means of an independent method, the actual energy of the electron peaks could be defined, this would provide a robust experimental method also to define the exact peak intensity of the excitation laser field. Such a method is based on the shift of intermediate resonances due to the AC-Stark effect.

Highly excited Rydberg states involve electrons that are almost free and shift parallel to the ionization potential. Therefore, the kinetic energy of the electrons emitted by resonant multiphoton ionization via those states is independent of the laser field intensity (Eq. 2.19 and 2.20). The absorption of 8 photons (λ_o=800 nm) is sufficient to excite xenon above the $^2P_{3/2}$ ionization threshold located at 97834 cm^{-1} [123] above the ground state. The excess energy of the transition, if ponderomotive shifting is neglected, would be 2150 cm^{-1}. If the intensity of the laser field exceeds the value of 2.9×10^9 W/cm^2, the corresponding ponderomotive potential is enough to close this ionization channel and more photons are required for ionization. By absorption of one more photon the second ionization threshold $^2P_{1/2}$ at 108371 cm^{-1} [123] is reached. The into-resonance shift of atomic levels is manifested by the change of the ATI electron peak shape from a symmetric sharp profile, in the case of non-resonant ionization, to a more structured and broad profile. The onset of this effect is visible in Fig. 3.11 for the highest pulse energy 75μJ. A more detailed investigation of this effect is shown in Fig. 3.12b, where the first two ATI electron peak were measured with the Wiley-MacLaren TOF for excitation energies of 85, 95 and 105 μJ per pulse. Also, for comparison, the corresponding reference spectra reported by Nandor et.al. [121] are depicted in Fig. 3.12a. The electron peaks in Fig. 3.12b originate from the 8-photon ionization and the first order (S=1) ATI of xenon. Following the discussion in Ref. [121,122], an increase of the laser field intensity results in the channel switching via the $^2P_{3/2}nf$ and $^2P_{1/2}ng$ Rydberg levels of xenon. The peaks A and B in figures 3.12 a and b correspond to the 4f and 5g states. Both
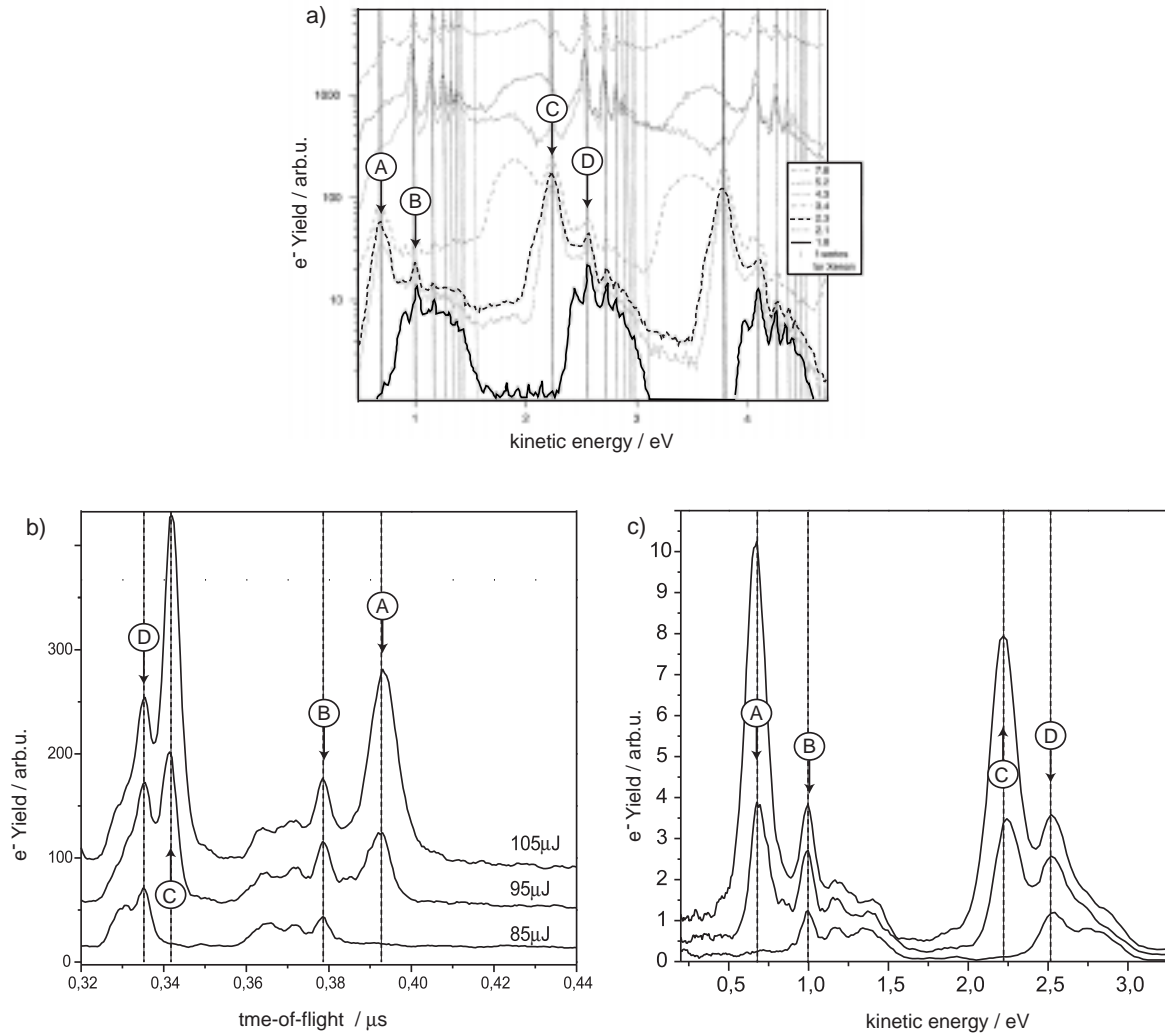
Figure 3.12: Resonance effect in above-threshold-ionization of xenon due to AC-Stark shifted Rydberg states. The electron peaks A and B correspond to the channel switching to the $^2P_{3/2}4f$ and $^2P_{1/2}5g$ Rydberg states of xenon that occur for laser field intensities 1.9×10^{13} W/cm^2 and 4.0×10^{13} W/cm^2, respectively [122]. a) Reference photoelectron spectra adapted from [121] b) time-of-flight spectra measured with the Wiley-MacLaren electron-TOF and c) the corresponding calibrated photoelectron spectra.

Electron peak	Ionization scheme	Intermediate resonance	Associated ionization threshold	Kinetic energy
A	8+1	$(^2P_{3/2})4f$	$^2P_{3/2} : 97834\ cm^{-1}$	0.68 eV
B	9+1	$(^2P_{1/2})5g$	$^2P_{1/2} : 108371\ cm^{-1}$	1.0 eV
C	8+2	$(^2P_{3/2})4f$	$^2P_{3/2} : 97834\ cm^{-1}$	2.23 eV
D	9+2	$(^2P_{1/2})5g$	$^2P_{1/2} : 108371\ cm^{-1}$	2.55 eV

Table 3.1: Reference kinetic-energies employed for the calibration of the electron spectrometer. Both photoelectron peaks A and C result from the resonant multiphoton ionization of Xe, via the $(^2P_{3/2})4f$ level, and ionize, by absorption of one and two additional photons, respectively, to the $(^2P_{3/2})$ threshold. Accordingly, for peaks B, and D, ionization occurs via the $(^2P_{1/2})5g$ level, which correlates to the$(^2P_{1/2})$ threshold.

shift into resonance when the excitation laser field reaches the intensity $1.9 \cdot 10^{13}$ W/cm^2 and $4.0 \cdot 10^{13}$ W/cm^2, respectively. Due to the electronic configuration of the specific states, by absorption of one more photon an electron is ejected into the $^2P_{3/2}$ and $^2P_{1/2}$ atomic continua, respectively. The corresponding kinetic energies are 0.68 eV and 1.0 eV. At higher order ATI peaks the distinct Ryderg structure is still present. However, the limited spectrometer resolution prevents the clear observation of the resonance structure above the (S=3) ATI order (not shown here). The electron peak assignment used for the energy calibration is summarized in Table 3.1.

Using the above kinetic-energy assignment of the photoelectron peaks A, B, C and D, the constants of the second-order polynomial calibration curve $E_{kin}(T)$ can be defined. Since Eq. 3.10 is a non-linear function, to derive the calibrated electron-spectrum $S(E_{kin})$ the time-of-flight spectrum $S(T)$ is subject to the so-called *Jacobi Transformation*. Consider the integrated electron signal $S(T) \cdot \Delta T$, measured by the MCP detector within a finite time-of-flight interval ΔT. When performing the transformation into the calibrated signal function $S(E_{kin})$, the integrated electron signal within the corresponding energy interval ΔE_{kin} must be conserved. This condition is fulfilled by means of the Jacobi Transformation:

$$S(T) \cdot \Delta T = S(E_{kin}(T)) \Delta E_{kin}, \qquad (3.12)$$

which in the limit $(\Delta T \rightarrow 0)$ becomes:

$$S(E_{kin}) = S(T)(\frac{\partial E_{kin}}{\partial T})^{-1}, \qquad (3.13)$$

Practically, the last equation implies that to derive the calibrated spectrum $S(E_{kin})$ the measured time-of-flight spectrum has to be divided by the derivative of the calibration function $E_{kin}(T)$.

3.4   The Molecular beam setup

The subject of this thesis is the interaction of femtosecond laser radiation with isolated atoms and molecules. To meet this requirement, experiments were performed under low particle density conditions, to avoid collision of the sample atoms or molecules with eachother. These so-called gas phase experiments are customarily performed in high vacuum ($10^{-5} - 10^{-7}$ mbar) by extracting the atmospheric air from airtight metallic chambers. Then, the sample is brought to the laser interaction region in very low densities through small orifices with a typical diameter of 100 μm. If the pressure $p_\circ$ in the gas reservoir, supporting the gas flow through orifice (backing pressure), is relatively low, the mean-free-path of the molecules is larger than the opening of the orifice and the gas expansion inside the vacuum chamber is denoted as an *effusive beam* [124]. In the opposite case that the backing pressure of the reservoir is high, the passing through the orifice is accompanied by multiple collisions of the gas molecules. The expansion is so fast that practically no temperature exchange is taking place with the surrounding i.e. the expansion is adiabatic and the total enthalpy is conserved. If both the kinetic energy of the gas inside the reservoir as well as the pressure in the vacuum chamber are assumed zero, the enthalpy conservation law can be expressed as:

$$U_\circ + p_\circ V_\circ = U + \frac{mu^2}{2} \tag{3.14}$$

where $V_\circ$ is the reservoir volume, $U_\circ$ and U the inner vibrational and rotational energy of the molecules before and after the expansion, m the mol-mass and u is the velocity of the molecules after passing through the orifice. From Eq. 3.14, if the kinetic energy $\frac{mu^2}{2}$ of the expanding gas increases, then the inner energy and subsequently the temperature of the gaseous sample is reduced.

On the other hand, the gas flow through the orifice results in an increase of the pressure inside the vacuum chamber, which can be problematic in the sense of maintaining the low particle density condition. To encounter this discrepancy, a special technique was developed by D.R. Herschbach [125], Y.T. Lee [126] and J.C. Polanyi [127] that revolutionized the era of laser spectroscopy, namely the *molecular beam* technique. It allows for the propagation of dense gaseous samples in a well-localized manner inside vacuum by means of specially designed conical apertures (skimmers) that select the central and well collimated part of the adiabatic gas expansion. This experimental scheme is depicted in Fig. 3.13. The divergence of the formed molecular beam depends on both the distance between the skimmer and the orifice d and the opening of the skimmer b,
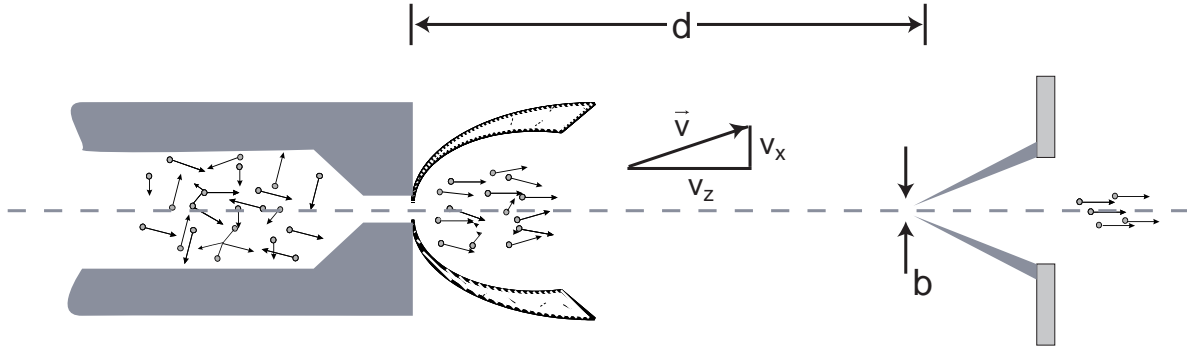
Figure 3.13: The molecular beam setup. The investigated gaseous sample is expanded inside the vacuum chamber through a small orifice. Under appropriate backing pressure conditions the expansion is adiabatic and a substantial lowering of the samples temperature is achieved. By means of a conical apperture (skimmer) the central and most dense part of the expansion is selected. This propagates further to the right side of the skimmer, where the investigated laser interaction is taking place.

according to the formula:

$$\frac{v_x}{v_z} \leq \frac{b}{2d} \tag{3.15}$$

where v_x and v_z are the parallel and the vertical velocity components with respect to the beam propagation axis. For even better collimation, a second skimmer can be used. Following the discussion in Ref. [124, 128, 129], the temperature lowering during the formation of the molecular beam is accompanied by the transition from the broad Maxwell velocity distribution inside the reservoir:

$$N = N_\circ e^{-\frac{m}{2kT_\circ}v_z^2} \tag{3.16}$$

to a significantly narrower distribution:

$$N = N_\circ e^{-\frac{m}{2kT_\parallel}(v_z - u)^2} \tag{3.17}$$

The average velocity u is given by:

$$u = \sqrt{\frac{2kT_\circ}{m}\frac{k}{k-1}} \tag{3.18}$$

where k is the adiabaticity coefficient, depending on the specific molecule. In Fig. 3.14 a) the thermal velocity distribution (dashed line) is depicted, in comparison to the sharp distribution in the molecular beam (solid line). In several cases, the investigated molecular sample may exhibit a vapor pressure that is not sufficient to support an adiabatic expansion. However, the required pressure conditions can be achieved, if the
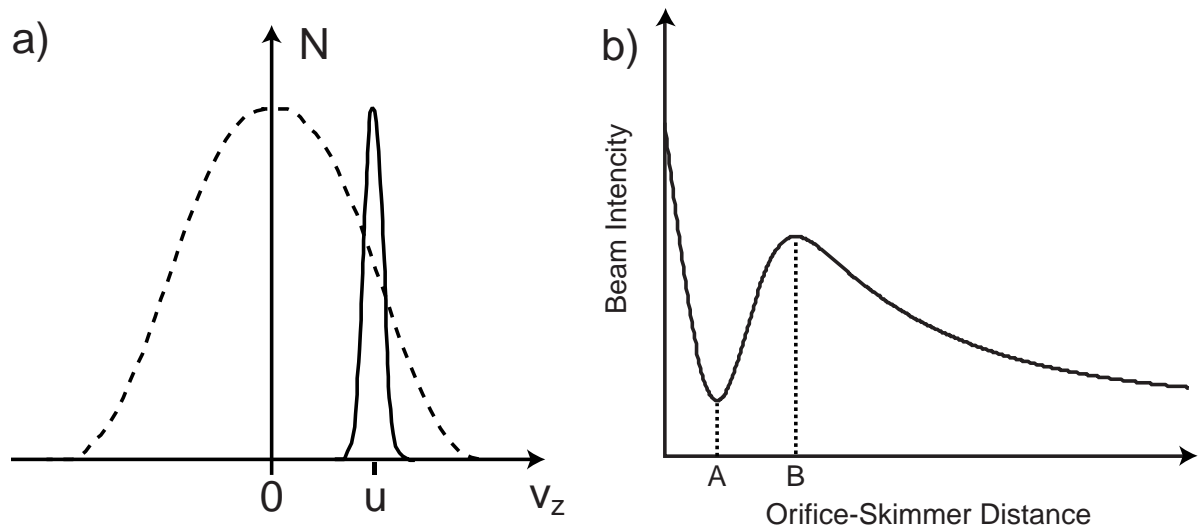
Figure 3.14: Adiabatic expansion of a gaseous sample. a) qualitative diagram of the velocity distribution in the sample reservoir (dashed line) and the narrow distribution after the adiabatic expansion (solid line), b) the molecular beam intensity dependence as function of the distance between the orifice and the skimmer.

molecular sample is mixed with a so-called buffer gas. The buffer is a neutral gas (typically Ar or He) and coexpands with the molecules of the sample. This method is denoted as the *seeded molecular beam* technique.

To maintain the desired vacuum conditions, the experimental arrangement in Fig. 3.13 is equipped with a pumping system, comprising two separate vacuum chambers (differentially pumped system), one on the left and the other on the right side of the skimmer. The only link between the two chambers is the small skimmer opening which allows for maintaining two different vacuum levels simultaneously. The left chamber, routinely denoted as preparation chamber, is pumped by an oil-diffusion pump of 3000 l/s pumping speed and operates at a vacuum level of 10^{-5}–10^{-4} mbar. The chamber on the right, which encloses the mass- or electron- spectrometer (spectrometer chamber), is pumped by a turbomolecular pump of lower pumping speed 500 l/s but operating at a much lower vacuum level 10^{-7} mbar. This configuration combines the high pumping speed of the oil-diffusion pump, necessary for removing the residual gas that is rejected by the skimmer and the low final pressure achieved with the turbomolecular pump. The later is crucial with respect to both, the reduction of the background signal in the spectrometer and the maintenance of the undisturbed operation of the multichannel plate (MCP) detector.

Due to the relatively high pressure inside the preperation chamber, the adiabatic gas expansion is, to a certain degree, subject to retardation effects. These manifest

themselves by the reduction of the expansions velocity u and by the formation of shock waves [124,129]. In Fig. 3.14b, the qualitative behaviour of the molecular beam intensity along the propagation axis is depicted as a function of the distance between the orifice and the skimmer. The analytical form of this function is found in Ref. [124]. The position as well as the decrease-rate from the intensity maximum B depend on the pressure conditions inside the preparation chamber as well as on the dimensions and geometry of the orifice.

From the spectroscopical point of view, the temperature decrease of the investigated molecular sample is of great importance. Especially in studies involving large molecular systems, where the energy spacing between successive vibrational levels is rather small, preparation of the sample in a cold molecular beam corresponds to a substantial narrow distribution of the quantum states, that serve as initial states in the laser excitation schemes.

3.5   Data acquisition and processing

The study of femtosecond dynamics, by means of ion- and electron-spectroscopy, requires the digitization and recording of the analog signal from the time-of-flight measurements. Also, in pump-probe experiments, this process has to be repeated many times, for different values of the delay time between the excitation pulses, to acquire the complete transient spectrum. In the following paragraphs, a number of acquisition systems are described that undertake the above tasks and have been used for the experiments in this thesis. The processing of the spectroscopic signal follows the 1 KHz repetition rate of the amplified Ti:Sapphire system. This allows for combining the time-of-flight method with a machine learning algorithm. In the last paragraph of this chapter, an iterative scheme is addressed, where the spectroscopic TOF signal is implemented as feedback in an evolutionary algorithm. The later addresses the LCD modulator and tests different femtosecond pulse-shapes. With this iterative scheme, optimal femtosecond laser pulse-shapes were found, that drive a laser excitation process toward a desired outcome.

3.5.1   Acquisition of a time-of-flight spectrum

The complete time-of-flight spectrum can be acquired with a digital oscilloscope (LeCroy, 9354AM) and then directly transmitted to the laboratory computer via a serial-IEEE connection. As reference time for the acquisition, a 1 KHz digital TTL signal, synchronous to the Ti:Sapphire system, was employed. This reference signal is delivered by the electronic unit (MEDOX) that controls the timing of the electro-optical switching in the Ti:Sapphire amplifier and is routinely denoted as "the trigger". The digital oscilloscope performs elementary mathematical operations, like averaging of the acquired waveform (spectrum) over a large number of laser pulses. In this way the signal-to-noise ratio of the measurements substantially improves. However, in several cases, the ionization signal is so low that an averaging over a very long time interval must be performed. This can be problematic due to systematic background electrical noise, which after a long averaging time acquires an amplitude which is comparable to the time-of-flight signal. To cope with this problem, a *Time-to-Digital Converter* (TDC) (FASTComtech p7886) is rather employed. TDC records the time between the trigger (start-event) and the time that a single electron- or ion- is registered on the MCP-detector (stop-event). For a single start-event (single laser pulse) the recording of several stop-events is possible (multihit-operation) with a dead-time of 0,5 ns. In this aquisition scheme, the analog signal from a particle that reaches the MCP detector is digitized and the background
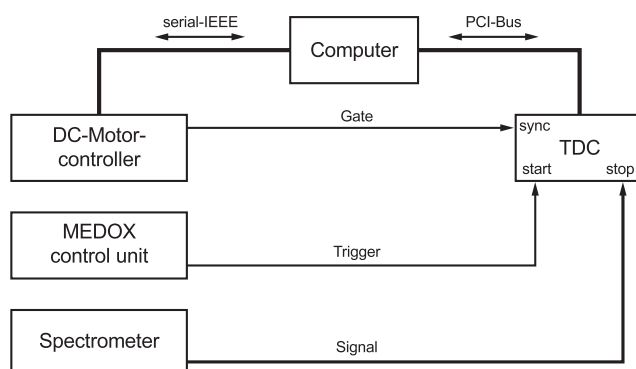
Figure 3.15: Schematic representation of the asynchronous combined operation of the DC-motor and the TDC. A direct connection between the two devices (gate) allows for their sequential operation. After reaching the desired position, the DC-motor control unit transmits a constant voltage which initiates the acquisition of the time-of-flight spectrum by the TDC.

noise is filtered out.

3.5.2 Acquisition of a Pump-Probe transient

The delay-time in the pump-probe experiments is automatically adjusted by means of a computer addressed DC-motor (Aerotech, Unidex 100/1035DC), which also allows for the combined operation with the TDC. This combination is realized in a so-called "asynchronous" scheme, by which the time-of-flight spectrum can be recorded as a function of the motor position. The term asynchronous indicates that the two devices operate in a sequential manner, independent from one another, without the necessity of an intermediate synchronization unit. In Fig. 3.15 a schematic representation of this acquisition system is depicted. The direct connection (gate) between the DC-motor control-unit and the TDC delivers a constant voltage after the motor has reached a specific position and gives a command to the TDC to start recording the time-of-flight spectrum. The scanned interval of the delay-time is programmed by the computer via a serial-IEEE interface. To improve the signal-to-noise ratio of the transient measurements, multiple scans of the same delay-time region can be recorded and averaged by the computer.

An alternative method to acquire a pump-probe transient in by means of the *Boxcar-Averager*. The Boxcar is an analog device that integrates the signal within a region of the time-of-flight spectrum and encodes it into a DC-voltage level. The outgoing analog signal is connected to an Analog-to-Digital Converter (ADC) and becomes digital. Then, the data are read-out from the computer and further processed. Unlike the TDC, the Boxcar is combined with the DC-motor in a "synchronous" mode i.e. the pump-

probe delay-time is scanned, while the averaged signal from the Boxcar is continuously recorded. In this configuration, a much shorter acquisition time is needed at the cost of that the pump-probe transient of just one (integrated) part of the spectrum is acquired. In general, several Boxcars can simultaneously be operated and acquire the transients of several parts of the time-of-flight spectrum.

3.5.3   Adaptive optimization algorithm

In Section 3.2.4, the optical methods by which complex femtosecond laser pulses can be generated were presented. With the liquid-crystal-display (LCD) the spectral phase of the laser pulses can be automatically addressed by the laboratory computer [131, 132]. Therefore, a number of computational methods, like machine learning algorithms, can be implemented to search for the complex laser pulse shapes, required for the control experiments. The shape of a specific laser pulse, which in the following will be referred to as an "individual", is encoded into an array of 128 discrete phase values. It corresponds to a specific sequence of voltage values applied to the LCD array. Each individual is experimentally tested for its control performance by using experimental feedback from the mass- or electron-spectrometer. For this, the integrated signal from one or several regions of the time-of-flight spectrum is acquired with the Boxcar and recorded by the computer. In this way a "fitness function" is assigned to each individual.

The global search method employed to find the fittest individual is an evolutionary algorithm. Evolutionary optimization strategies were invented in the early seventies by Ingo Rechenberg [133] and further developed by H.P. Schwefel [134, 135] for solving a number of technical problems, inspired by the theory of biological evolution. The iterative course of the optimization is summarized in Fig. 3.16. Initially, a pool of 60 randomly initialized individuals, are experimentally tested and a fitness value is assigned to each one. After evaluating all individuals from the pool, the 10 fittest laser pulses are selected to produce a new pool of laser pulses, namely the new "generation". This is realized by use of "cloning", "mutation" and "cross-over" operations. The new generation is then tested again. By cycling the evolutionary loop a number of times, the fitness of the best individuals increases from generation to generation until an optimum is found.
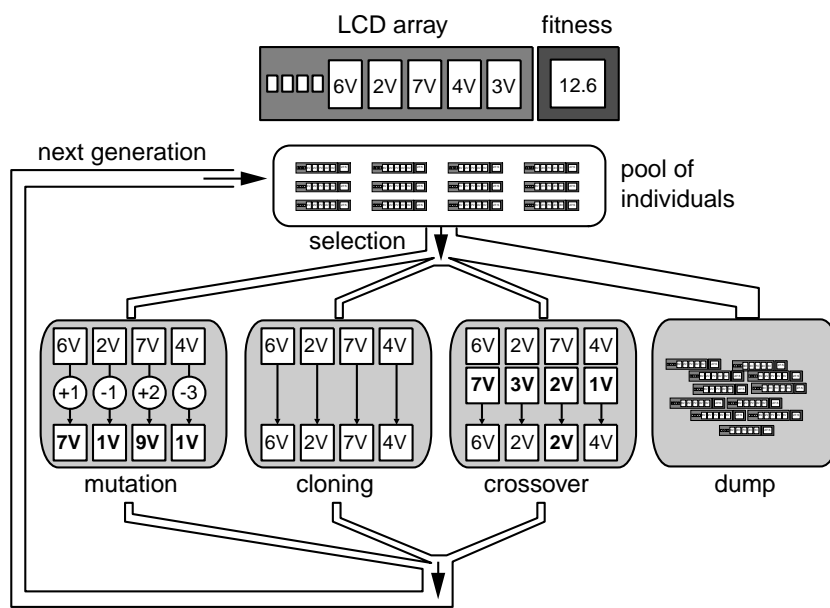
Figure 3.16: The evolutionary algorithm. Each laser pulse-shape (individual) is appointed to an array of 128 voltage components. In each iteration of the algorithm, 60 individuals are tested, and a fitness value is assigned to them. From the initial individual pool, the 10 fittest are selected and further used for generating the next generation of individuals.

4 Adaptive laser control of atomic double ionization

4.1 Introduction

Interaction of intense laser radiation with atoms or molecules can lead to the generation of multiply charged ions. This astonishing effect was first experimentally observed in 1979 by I. S. Alexakhin [136] and his coworkers, who investigated the multiphoton ionization of strontium utilizing an intense neodymium laser. In the following years, similar results have been reported by other groups for rare gases [137, 138], alkaline earths [139–143], alkali [144]and rare earth atoms [138, 145]. These experimental findings awakened a wide scientific interest to understand such high intensity effects. From a theoretical point of view, the electronic excitation of an atom can be described by the time dependent Schrödinger equation. However, for multielectron-atoms a challenging problem arises, due to the mutual Coulombic repulsion between the electrons. Investigating these complex correlation effects by means of an analytical or numerical solution is a tedious task and a number of approximate methods must be employed. The simplest approach is the single-active-electron approximation (SAE) by which the Schrödinger equation of a single electron is solved within an effective Hartree potential, which includes the Coulomb forces from the nucleus as well as the remaining electrons in a static manner. Several cases of interactions of laser radiation with multielectron-atoms can be well-described within this approximation.

However, significant deviations from SAE have been reported in experiments involving atomic double ionization. There, the experimental observations deviated from the values predicted within the SAE approximation by many orders of magnitude. For instance, in the spectrocopic studies by D.N. Fittinghoff [147] and B. Walker [148] a so-called *"knee structure"* of the femtosecond double ionization of helium was observed (Fig. 4.1a). In this graph, the solid line corresponds to the ionization probability calculated, using the SAE approximation. The predicted ion yield for single ionization
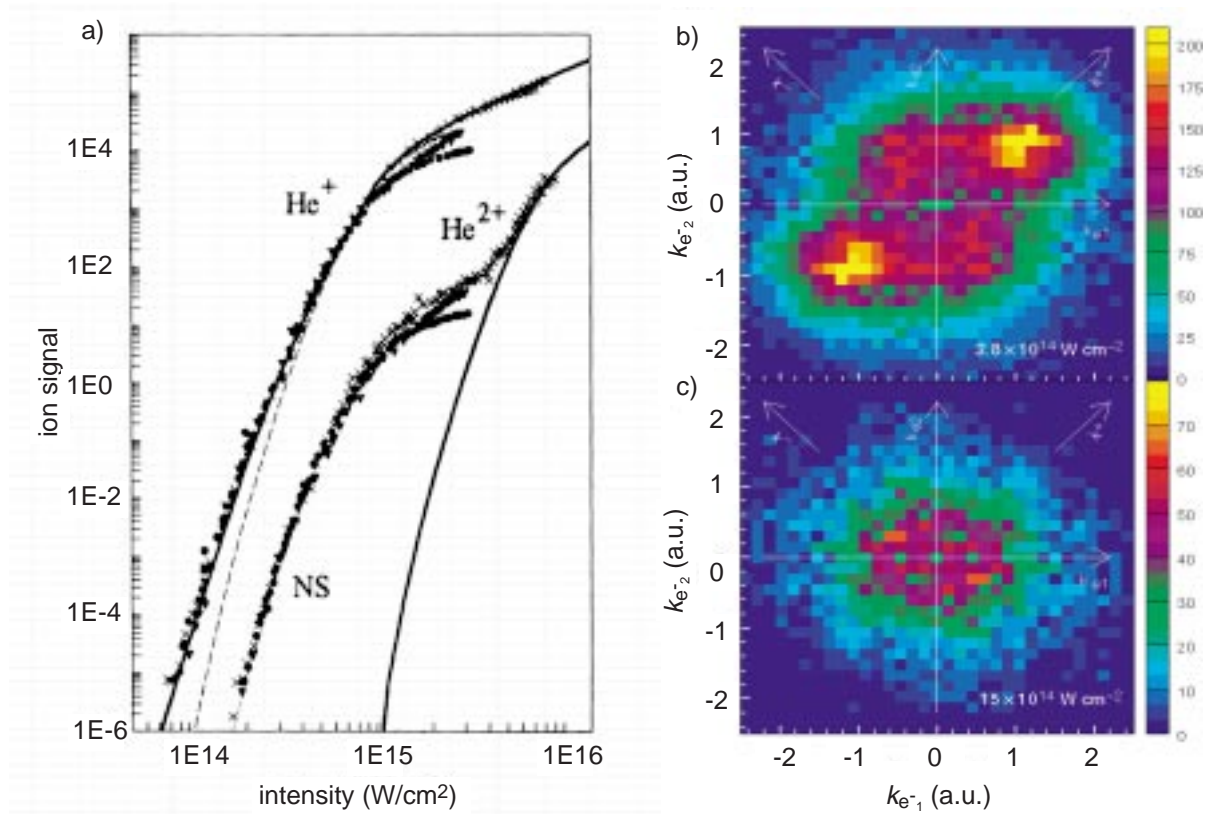
Figure 4.1: Double ionization of helium. a) Intensity dependence of the single and double ionization of helium, adopted by [147]. A so-called *"knee structure"* is observed for the He^{2+} signal which is not predicted within the SAE approximation (solid lines). A theoretical model involving an pair of correlated electrons (dashed line) rather matched the experimental findings. b),c) Velocity distribution mapping of the electrons emitted during the double ionization of helium measured with COLDTRIMS [149,150]. The physical interpretation of these measurements is addressed in the text.

matches nicely the measured signal, while for laser intensities above $5 \cdot 10^{15}$ W/cm^2 the same holds for the double ionization. Nevertheless, in the intensity region below $5 \cdot 10^{15}$ W/cm^2 a significant deviation from the measured He^{2+} signal is observed. There the SAE approximation fails to describe the experimental findings and a different mechanism of double ionization is believed to be dominant. Following the discussion in Ref. [147, 148], an alternative scenario would involve the simultaneous excitation of two electrons, which in a correlated manner are ejected into the atomic continuum. A numerical simulation of this process is shown in Fig. 4.1a (dashed line) which is in good agreement with the measured He^{2+} yield.

The direct experimental verification of a simultaneous and correlated electron excitation is no trivial task. A detection scheme utilizing time-of-flight photoelectron spectroscopy is obstructed by the fact that the electrons from the simultaneous exci-

tation channel energetically overlap with those ejected sequentially and uncorrelated. In 1997, a specially designed technique was introduced by Ullrich and his cooworkers to cope with this problem, namely the *Cold-Target Recoil-Ion Momentum Spectroscopy* (COLDTRIMS) [149, 150]. In COLDTIMS the momentum of both the two ejected electrons as well as the remaining doubly charged ion can be measured. The generated doubly charged ions are detected simultaneously with the corresponding electrons (coincidence measurement), and a position sensitive detector delivers the information of their momentum. The impressive results reported by Weber et.al [151] are shown in Fig. 4.1b and c. In those figures, a velocity-map of the two emitted electrons is depicted, following the double ionization of argon. In Fig. 4.1b, the intensity of the excitation laser field lies in the region where the correlated (non-sequential) excitation mechanism is dominant. In Fig. c, the intensity is higher and the SAE model holds. The correlated motion of the emitted electrons is evident by the observed splitting of the electron signal in two locations upon the diagonal axis of Fig. 4.1b.

One crucial parameter in COLDTRIMS is that the total ionization rate has to be extremely small, to avoid statistical errors in the coincidence measurement. Therefore, the acquisition time for a single map lies in the range of tens of hours. Additionally, the investigated atoms must be prepared in an atomic beam with internal temperature below 0.2 K, which for substances like alkaline earths is no trivial task. However, alkaline earth atoms are of particular interest since, unlike in the case of helium, they doubly ionize with much lower laser field intensities i.e. the double ionization is taking place in the multi-photon rather than in the tunneling regime. Experiments on calcium and magnesium have shown that electron correlation plays an important role also for single ionization [142, 143].

In the multi-photon regime, the simultaneous excitation of two valence electrons can be strongly influenced by the presence of doubly exited states. These are embedded in the atomic continuum (Chapter 2.2.3) and can resonantly enhance the non-sequential multiphoton transition to the double ionization continuum. In the tunneling-regime, the process of double ionization is rather insensitive to the exact electronic structure of the atom. In previous studies on multi-photon double ionization of calcium [141], conducted with 1064nm picosecond Nd-YAG laser radiation, comparable Ca^+ and Ca^{2+} ion signals were measured for laser field intensities as low as 10^{12} W/cm^2. The high Ca^{2+} yield was assigned to the effect of a dynamically shifting resonance. Also, in the later work by DiMauro et.al. [142], employing time-of-flight photoelectron spectroscopy, the different channels of sequential and non-sequential multiphoton double ionization are addressed.
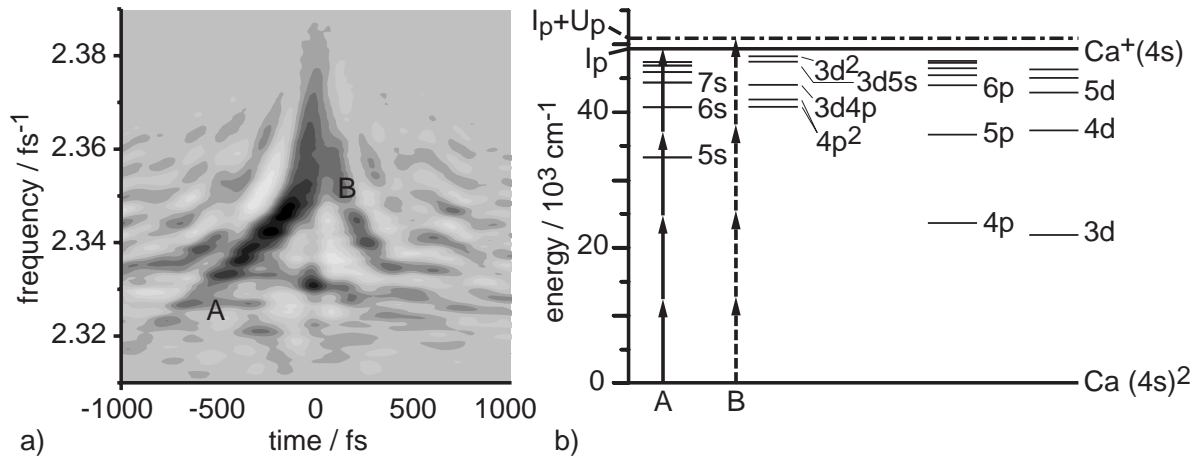
Figure 4.2: Adaptive optimization of Ca^+. a) The optimized laser pulse shape is plotted as Wigner distribution. b) The energy level diagram of atomic calcium. The weak-field ionization potential is labeled with Ip. It can be reached by four-photon absorption of intermediate photon energies (A, solid arrows). However, the ponderomotive shift Up leads to an increase of the ionization threshold up to Ip+Up (dashed-dotted line) so that photons of higher energy are required (B, dashed arrows).

There, a sequential ionization process was found to be dominant for the production of Ca^{2+}. However, in the same work, it was suggested that by properly choosing the laser parameters the amount of doubly ionized atoms could be further enhanced. Specifically, they proposed to tune the laser into resonance with a doubly excited state.

In a recent experiment performed in our group, the Ca^+ signal, produced by employing 800 nm femtosecond laser pulses and an atomic calcium beam, could be enhanced by modulating the spectral phase of the laser pulses. Single ionization of atomic calcium requires at least four 800 nm photons. Because of this nonlinearity, one could expect that an optimally short bandwidth-limited laser pulse with intrinsic maximized peak intensity serves rather this purpose. However, this was not the case. With a specific optimal laser pulse, it is possible to obtain more Ca^+ ions than with the bandwidth-limited laser pulse. Both, the Wigner trace of the optimized laser pulse (Fig. 4.2a and the energy level diagram of calcium (Fig. 4.2b give the key for the understanding of this unusual behaviour. The optimal laser pulse consists of mainly two contributions: a) a linearly up-chirped part between about -500 fs and 0 fs, in which the momentary light frequency increases from position A to position B and b) an unchirped part around 0 fs, in which a broad range of frequencies is available simultaneously. In the beginning of the linearly chirped part (position A), the energy of four photons (Fig. 4.2 b, solid arrows) is just sufficient to ionize calcium in a non-resonant four photon process. How-

ever, in the subsequent temporal evolution, the momentary intensity of the laser pulse increases. This leads to a ponderomotive shift Up which shifts the ionization potential upwards to higher energies Ip+Up (Fig. 4.2b, dashed-dotted line). The density of states in the singly ionized continuum is the largest in the direct proximity of the ionization threshold. Therefore, an optimized transfer of population can be achieved with linear up-chirp, as the increasing energy of the four photons absorbed (Fig. 4.2b, dashed arrows) always equals the increasing energy difference between ground state and shifted ionization threshold. In the same manner, a down-chirp component should occur in the falling edge of the laser pulse (decreasing intensity). Such a component does not appear in Fig. 4.2a. This could be due to the failure of the algorithm to locate such an optimal pulse structure, or to an additional dynamical process which is not taken into account in this interpretation. The second contribution in the optimum pulse shape represents a broad range of frequencies from the upper-energy part of the laser spectrum. This unchirped contribution is associated with high intensity, as seen in the distribution of simultaneous arriving frequencies around time zero, and suits for optimum transfer.

In this chapter, a similar optimization scheme is employed to study the multiphoton double ionization on calcium atoms with 800 nm femtosecond laser radiation. In this context, the technique of adaptive femtosecond pulse-shaping is combined with the simple, compared to COLTRIMS, techniques of time-of-flight (TOF) mass spectroscopy as well as TOF photoelectron spectroscopy, to gain insight into electron correlation effects and the dominant mechanisms responsible for the large yield of double ionization of atomic calcium.

4.2   Experimental scheme

An atomic beam of calcium was prepared by heating calcium pellets up to 600ºC inside the preparation chamber, which is separated by a 1 mm skimmer from the spectrometer chamber. There, the 800 nm femtosecond laser pulses by the Ti:Sapphire laser system are focused and crossed at right angle with the atomic calcium beam. The Wiley-MacLaren time-of-flight spectrometer was oriented perpendicular both to the laser beam and the atomic beam axis. As described in Section 3.3.2, the laser interaction region is located between two voltage controlled metallic apertures 1 cm apart from each other. Both, the released ions and photoelectrons were detected in this geometry. In TOF-mass spectrometry the formed ions were extracted by a field of 300 V/cm, while energy resolved TOF-photoelectron spectroscopy was performed with no electric field in the interaction region. For ion detection the signal from the MCP-detector was directly connected to the digital oscilloscope (LeCroy, 1GHz). For electron measurements the TDC (Section 3.5) was rather employed. The laser intensity in the interaction region was estimated by measuring the ponderomotive shift in the reference ATI spectra of xenon (Section 3.3.5). To optimize the ion yield of Ca^{2+} the adaptive optimization loop, described in chapter 3.5.3, was employed and is schematically summarized in Fig. 4.3. The femtosecond laser pulses are shaped in time by manipulating their spectral phase function. In this shaping procedure the total pulse energy was not modulated.

4.3   Intensity dependence of the ionization signal

In a first experiment the yield of singly ionized calcium Ca^+ and of doubly ionized calcium Ca^{2+} was measured as a function of the laser intensity. From the double-logarithmic plot (Fig. 4.4a) a four photon dependence for the Ca^+ signal is found, as expected for the photon energy of 1.55 eV employed. With four photons of 800nm the ionization potential of atomic calcium of 6.11 eV is slightly lower than the total excitation energy. For a laser intensity of I=1×10^{13} W/cm^2 the Ca^{2+} and Ca^+ signals are similar. In the case of Ca^{2+}, the laser intensity dependence in the range of 10^{12}W/cm^2 shows only a slope of N=3.4±0.1 which does not reflect the high nonlinearity of the double ionization. With 800 nm photons eight more photons (starting from $Ca^+(4s)$) are needed to reach the double ionisation threshold at 15.78 eV. Similar measurements of the Ca^+ and Ca^{2+} yields were performed with photons of 400nm. From the double-logarithmic plot (Fig. 4.4b) a two photon dependence for the Ca^+ signal is found in the intensity
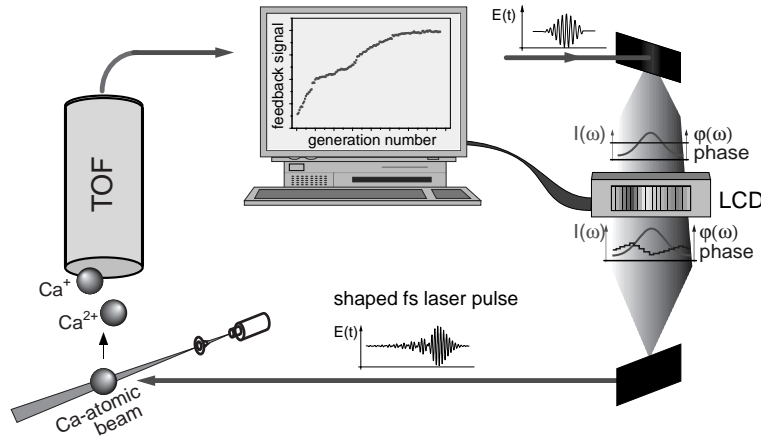
Figure 4.3: Experimental setup. The ion yield of Ca^+ and Ca^{2+} is measured utilizing a time-of-flight (TOF) spectrometer. The charge resolved ion signal is directly integrated as feedback signal to an evolutionary algorithm. The laser pulse shape is automatically controlled and an optimal laser pulse shape is iteratively determined. The same TOF spectrometer can be used to measure electron energy distributions. Different features of the photoelectron spectrum are used as feedback signal for the optimization.
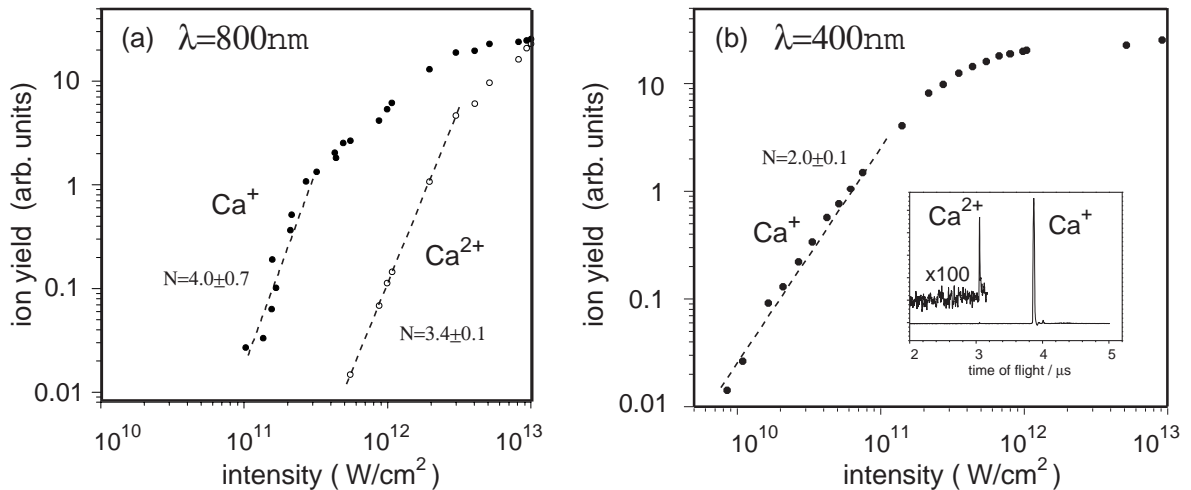

Figure 4.4: Log-log representation of the integrated charge resolved ion signal for excitation with a) 800 nm photons and b) 400nm photons as function of the laser field intensity. A typical TOF spectrum for excitation with 400 nm is shown in the inset of graph for laser field intensity $10^{13}\,\mathrm{W/cm^2}$. The production of doubly charged calcium ions appears to be two orders of magnitude less than that of singly charged ions, in contrast to the case of 800nm photons where the production of singly and doubly charged ions is comparable.
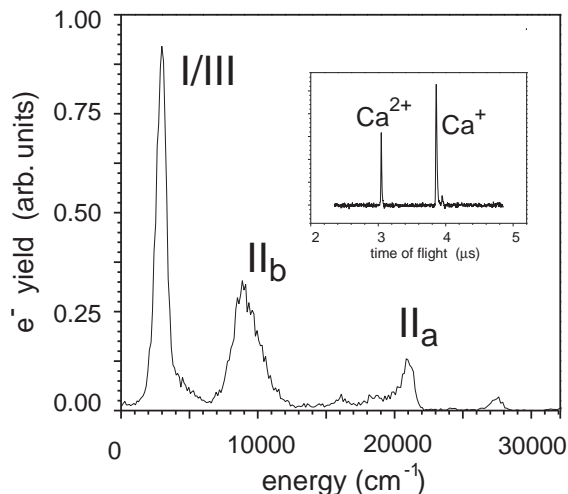
Figure 4.5: Electron energy distribution resulting from multiphoton ionization of calcium atoms interacting with 10^{12} W/cm^2 of 800nm laser field. The numeral labels I, IIa, IIb and III refer to the ionization channels defined in Fig. 4.6. In the inset graph, the corresponding TOF mass-spectrum is shown.

range of 10^{10}-10^{11} W/cm^2. In the inset of Fig. 4.4b the TOF mass spectrum is shown for an intensity of 10^{13}W/cm^2 of the 400nm laser field. The yield of Ca^{2+} is two orders of magnitude less than that of Ca$^+$ in contrast to the similar yields obtained in the measurements with 800nm photons.

4.4   The Photoelectron spectrum of calcium

The electron energy spectrum obtained following ionization of calcium atoms by 800 nm femtosecond laser radiation at an intensity of 2×10^{12} W/cm^2 is shown in Fig. 4.5. One of the dominant features observed is the peak (IIb) in the energy region of 9000 cm^{-1} which is attributed to the five-photon excitation of the $3dnl$ states with subsequent autoionization to the ground Ca$^+(4s)$ ionic state, which is process IIb in Fig. 4.6. The width of this electron peak exceeds 2000 cm^{-1} and is probably due to the five-photon absorption bandwidth. The $3dnl$ manifold in this excitation process is resonantly enhanced by the doubly excited $3d^2$ state. Also evident is a peak at an electron energy of about 21000 cm^{-1} which is assigned to the six-photon excitation of the $4pnl$ states and subsequent autoionization via pathway (IIa) to the Ca$^+(4s)$ ionic ground state. Note that by taking into account the six-photon bandwidth and the ponderomotive shift of the atomic energy levels direct ionization yielding Ca$^+(4p)$ is possible as well as excitation of a range of the $4pnl$ autoionizing states. This gives rise to minor features on the
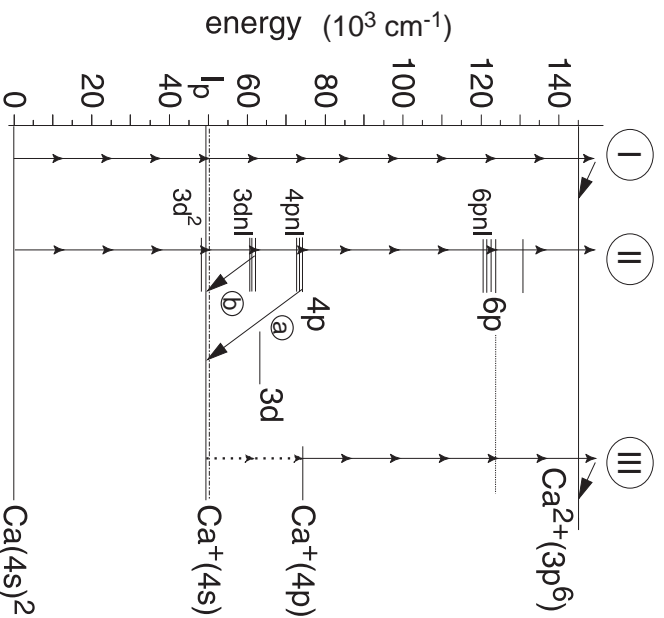
Figure 4.6: Energy diagram of atomic calcium. Excitation pathways resulting in the production of doubly charged calcium.(I) Non-sequential, non resonant, (II) Non-sequential resonantly enhanced and (III) sequential pathway, the atom is singly ionized while the parent ion is left to its ground $Ca^+(4s)$ or excited $Ca^+(4p)$ state. By an additional eight or six-photon absorption the double ionization threshold is reached respectively. In the case of the $Ca^+(4p)$ intermediate the resonance enhancing $Ca^+(4p-6p)$ transition results in a maximum nonlinearity of fourth order.

low energy side of the electron peak at 21000 cm^{-1}. The largest peak in the photoelectron spectrum around 3000 cm^{-1} is assigned to the formation of doubly charged calcium ions via sequential double ionization (process III). Here the singly charged ion $Ca^+(4s)$ is formed which is probed upon absorption of eight more photons to give $Ca^{2+}(3p^6)$. By taking into account the known central wavelength of the 800 nm femtosecond laser radiation this peak in the electron energy distribution should show up at 4300 cm^{-1}. The difference between the experimental value of 3000cm^{-1} and the estimated value of 4300 cm^{-1} may be due to the multiphoton nature of the transition and the resonance enhancing $Ca^+(4p-6p)$ transition. When considering the non-sequential double ionization processes I and II (Fig. 4.6), the corresponding electron energy distribution is expected to be a flat continuous spectrum from zero energy up to an energy determined by the excess energy of the twelve-photon absorption leading to $Ca^{2+}(3p^6)$ formation. This excess energy is about 5000cm^{-1} if ponderomotive level shifting is neglected. The excess energy is shared between the two ejected electrons with all possible angular mo-
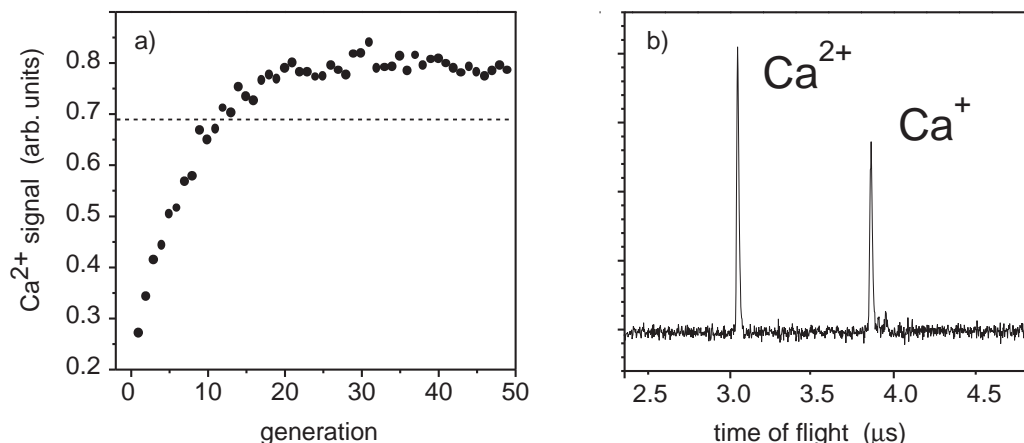
Figure 4.7: Optimization curve. a) The fitness function is presented as a function of iteration number during the optimization of Ca^{2+} yield. The dashed line shows the fitness value corresponding to unmodulated laser pulses. b) The resulting mass-spectrum after the optimization.

mentum combinations resulting in a broad energy distribution [142]. In addition to that the transmission of low energy electrons is poor for the linear TOF spectrometer. Both effects prevent the detection of the low energy electrons produced by the non-sequential processes I and II. Because of the low transmittance of our linear TOF spectrometer for electrons having low kinetic energy the observation of the 800 nm four-photon threshold ionisation of $Ca(4s^2)$ is also not possible.

4.5 Optimization of Ca^{2+} signal

In the experiments described above, time-of-flight (TOF) mass-spectroscopy as well as TOF photoelectron spectroscopy were employed in order to gain insight into excitation scheme of calcium interacting with the 800 nm femtosecond laser pulses. As a next step, adaptive optimization experiments were performed to maximize the double ionization yield by tailoring the femtosecond laser pulses. Here, the total Ca^{2+} signal was recorded and used as feedback in the optimization algorithm. The evolution of the Ca^{2+} yield is shown in Fig. 4.7 together with the time-of-flight mass spectrum obtained with the optimally shaped laser pulse. In the optimization the laser pulse energy is kept constant and is the same as employed in photoelectron spectroscopy (Fig. 4.5). The Ca^{2+} signal now exceeds the Ca^+ signal. Hence, by applying the adaptive optimization loop the absolute Ca^{2+} yield was enhanced by 30% under the given experimental conditions. It should be noted that no information about the process of double ionization is needed to find this optimal result. The optimal laser pulse (Fig. 4.8a) which is characterized by

the FROG technique is not bandwidth-limited as seen in the Wigner distribution function. The Wigner distribution function is obtained from the measured energy spectrum of the laser and the spectral phase function. The graph shows a positive linear chirp of the laser pulse at the leading edge followed by a part at time zero where almost all frequency components are available simultaneously. Additionally, a pronounced down-chirp is seen in the trailing edge of the pulse. This clearly shows that a specific phase modulated laser pulse is necessary for this optimal Ca^{2+} signal and not the maximum laser intensity. Considering the effect the optimally shaped laser pulse has on the electron energy spectrum compared to that of an unmodulated laser pulse, it is evident that the yield of the five-photon ionization process corresponding to the peak observed at 9000cm^{-1} (Fig. 4.8c) has decreased. This is consistent with the decrease of the Ca^{+} ion yield seen in Fig. 4.8b. The sequential ionization process III corresponding to the peak observed at 3000cm^{-1} in the electron energy spectrum has decreased as well. The enhanced signal of Ca^{2+} ions can therefore by no means be attributed to the sequential double ionization process III. Therefore it is evident that there is an additional contribution resulting from non-sequential double ionization. The electrons that originate from this ionization process cannot be directly observed due to the experimental constrains of our TOF spectrometer. This non-sequential ionization channel can be inferred indirectly by the increased Ca^{2+} ion yield and by the increased signal of the electron peak at 21000cm^{-1} which both depend on the phase structure of the tailored femtosecond-pulse. This electron peak corresponds to a six-photon absorption process in which excitation of the $4pnl$ autoionizing states occur via the intermediate doubly excited state resonance $3d^2$ and $3dnl$. Part of the Ca$^{**}(4pnl)$ population undergoes autoionization resulting in Ca$^{+}(4s)$ ions and the remaining part serves as intermediate enhancing resonance for the non-sequential ionization yielding Ca$^{2+}(3p^6)$. An additional ionization pathway connected with this six-photon absorption is the ionization and formation of excited Ca$^{+}(4p)$ due to the broad excitation bandwidth. Further four-photon excitation of Ca$^{+}(4p)$ into Ca$^{+}(6p)$ and subsequent two-photon ionization yield Ca$^{++}(3p^6)$.

4.6 Optimization of 21000cm^{-1} electron peak

In order to support the interpretation discussed above an additional experiment was performed. Adaptive optimization was now employed to maximize the electron signal of the peak observed at 21000cm^{-1}. The electron energy spectrum obtained after the optimization is shown in Fig. 4.9c and it is evident that the intensity of the electron peak

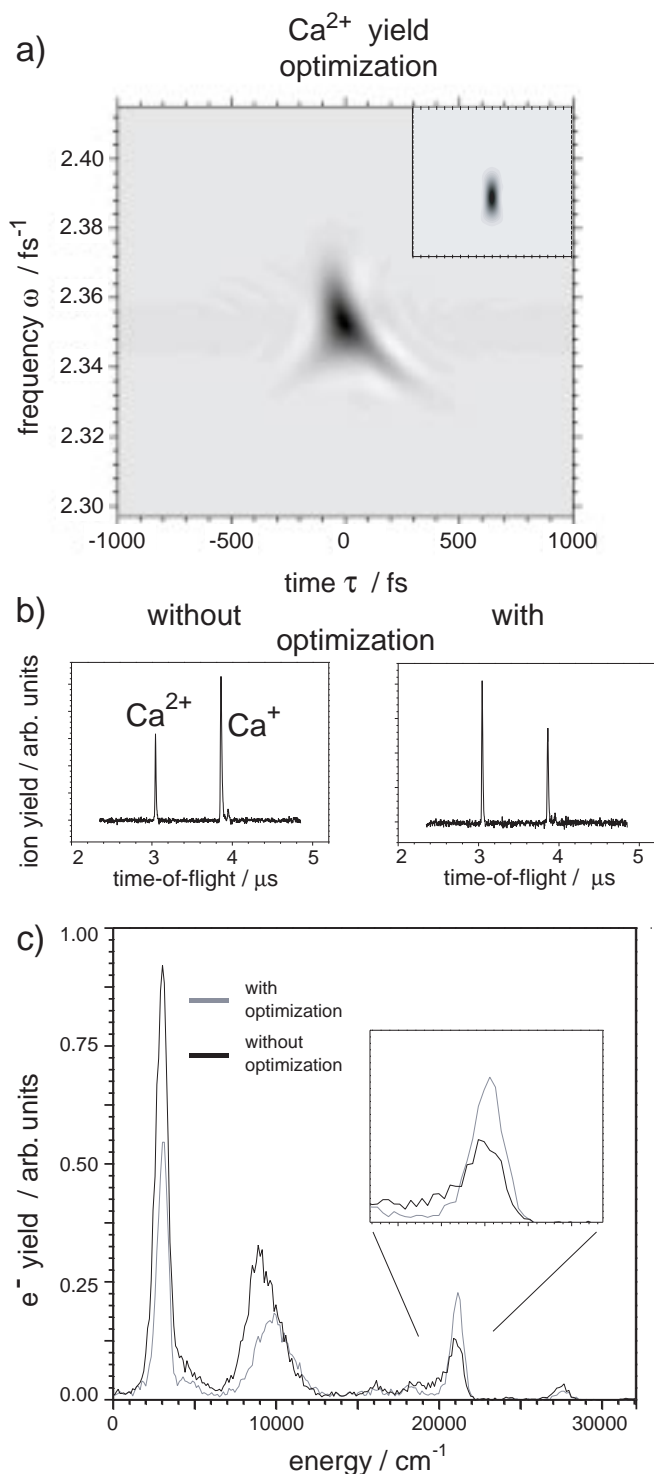**Figure 4.8:** Summary of the Ca^{2+} yield optimization: a) Wigner distribution of the optimal laser pulse. Inset graph on the top right shows the wigner distribution of the laser pulses with unmodulated spectral phase b) mass-spectrum with and without optimization of the laser pulse spectral phase, c) electron energy distribution with and without optimization of the laser pulse spectral phase.

at 21000cm^{-1} is considerably enhanced. The ion yields obtained after that optimization i.e. employing the same tailored laser pulses are shown in Fig. 4.9b. Without any doubt the Ca^{2+} signal now again exceeds the Ca$^+$ signal. This result clearly proves that the 21000cm^{-1} electron peak is at least partly due to an excitation process that results in the generation of Ca$^{2+}(3p^6)$ ions. However, it has to be noted that the absolute Ca^{2+} ion yield is reduced by a factor 0.85 compared to the excitation and ionization with the unmodulated laser pulse. The Wigner distribution of the optimal laser pulse is shown in Fig. 4.9a. The graph shows a negative linear chirp all along the pulse duration. Similarities and differences of this optimal pulse shape compared to the one found in the Ca^{2+} optimization are addressed in the next section.

4.7 Discussion

The key feature found in the adaptive control of double ionization of atomic calcium with 800nm femtosecond laser excitation appears to be the Ca$^{**}(3dnl)$ manifold of doubly excited states. As seen in the energy level scheme of atomic calcium (Fig. 4.6) the bound doubly excited states Ca$^{**}(3d^2)$ can be excited with the red part of the broad spectrum of the 800 nm femtosecond laser pulses in a four-photon process. Due to the large bandwidth ($\sim$600 cm^{-1}) of the four photon excitation of Ca$^{**}(3d^2)$ the further one-photon excitation to the Ca$^{**}(3dnl)$ manifold is strongly increased. It is known that the Ca$^{**}(3dnl)$ states have typical lifetimes of a few hundred femtoseconds [152]. Within this lifetime the Ca$^{**}(3dnl)$ states can either decay to the ground Ca$^+(4s)$ ionic state, or they can be transferred by additional one-photon absorption to the Ca$^{**}(4pnl)$ autoionizing manifold, giving rise to the electron distribution seen in the region of 21000 cm^{-1} in the electron energy spectrum. By further absorption of six more (800 nm) photons the Ca$^{**}(4pnl)$ population is transferred into the Ca$^{2+}(3p^6)$ continuum. Because of the large number of excited Ca$^{**}(4pnl)$ states the (800nm) four photon absorption process Ca$^{**}(4pnl) + 4$hv $\rightarrow$ Ca$^{**}(6pnl)$ within the six-photon ionization is strongly enhanced. In this excitation scheme it is well understood how the non-sequential double ionization takes place within a multi- resonance scheme of doubly excited states embedded in the ionic continuum. Consequently, the strongly nonlinear process of Ca^{2+} generation with 800 nm photons is divided into a series of excitation processes with a maximum non-linearity of fourth order. This is in good agreement with the observation shown in Fig. 4.4a where a fourth order non-linearity from the slope of the Ca^{2+} ionization yield was found. The optimal pulse shapes retrieved in the two optimization experiments, the
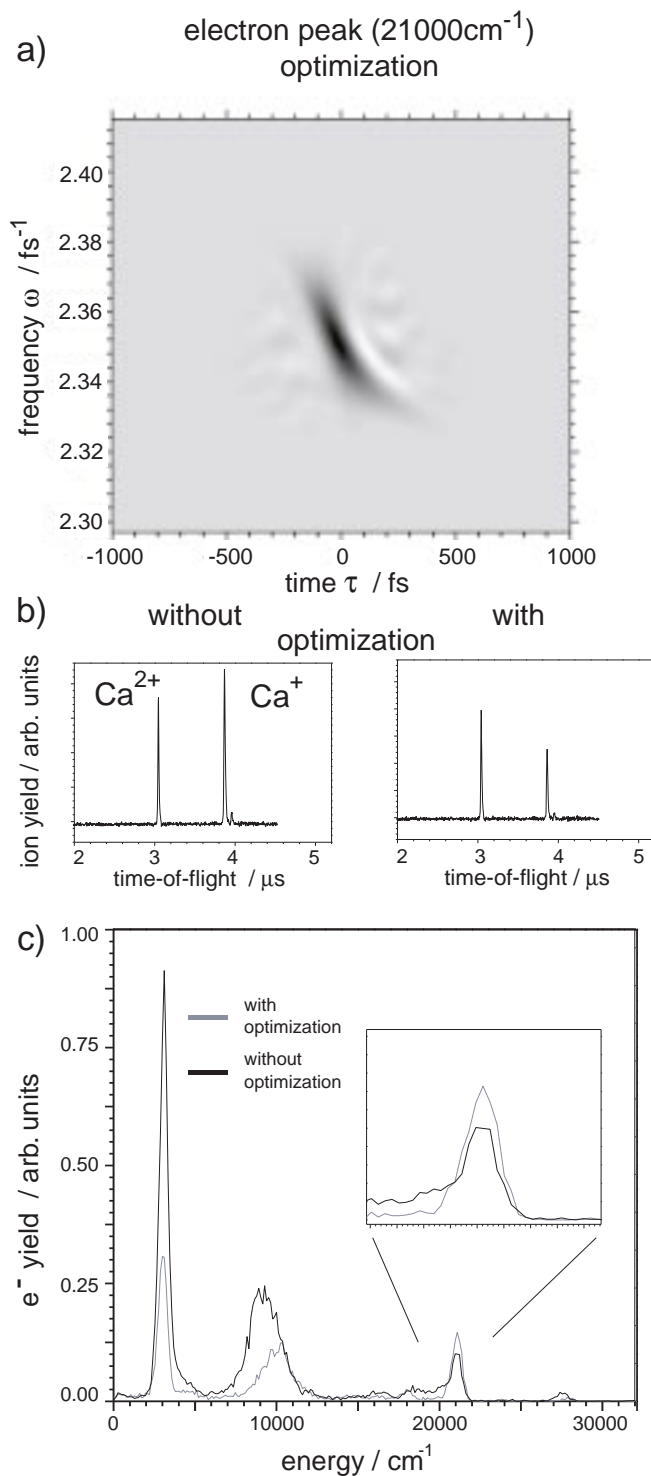
Figure 4.9: Summary of the 21000cm^{-1} electron peak optimization: a) Wigner distribution of the optimal laser pulse, b) mass-spectrum with and without optimization of the laser pulse spectral phase, c) electron energy distribution with and without optimization of the laser pulse spectral phase.

Ca^{2+} yield optimization and the $21000cm^{-1}$ electron peak optimization, both exhibit a pronounced downchirp feature in the trailing edge of the laser pulse. The main part of the laser pulse is less chirped and more intense and excites a broad range of states within the $Ca^{**}(3dnl)$ autoionization manifold. The trailing downchirp then excites preferentially the $Ca^{**}(4pnl)$ states instead of $Ca^+(4p)$ - photoionization and therefore increases the population in the doubly excited manifold which gives rise to an enhanced non-sequential ionization signal. Ionization leading to $Ca^+(4p)$ contributes finally to sequential ionisation. In both optimizations the enhanced excitation process is the non-sequential double ionization via the $Ca^{**}(3d^2)$, $Ca^{**}(3dnl)$ and $Ca^{**}(4pnl)$ states. The difference in absolute Ca^{2+} ion yields in the two experiments originates from the contribution of the sequential double ionization process III, which appears to be less dominant in the case of the electron peak optimization. This is in agreement with the measured photoelectron spectra (Fig. 4.8c and 4.9c). In the context of the optimal control scheme described above it can be understood why the probability of double ionization of atomic calcium is much smaller compared to single ionization when 400nm femtosecond laser radiation is employed. Although the $Ca(4s^2) + 2hv \rightarrow Ca^{**}(3d^2)$ transition is not forbidden due to dipole selection rules, the excitation efficiency to the $Ca^{**}(3d^2)$ configuration is expected to be significantly higher with 4 rather than 2 photons. Since the population of the $Ca^{**}(3d^2)$ state is essential for the non-sequential double ionization this process is more efficient for 800nm. In the recent theoretical work by Suzor-Weiner et.al [153] the interaction of a model atomic system with our experimentally measured optimal pulse shapes is presented. The effect of enhancement of the Ca^{2+} yield upon interaction with the optimal laser field shown in Fig. 4.8a was reproduced. The discussed mechanism of doubly excited intermediate resonances is close to our proposed control scheme. Nevertheless the importance of the phase structure of the optimal laser pulse shape has to be stressed i.e. the time at which the different frequency components of the laser bandwidth occur within the pulse duration. This is in contrast to the theoretical work where the effect of optimization is attributed only to the time asymmetry of the laser pulse envelope.

4.8   Conclusion

In this chapter investigation of the multiphoton double ionization of atomic calcium employing 800 nm and 400 nm femtosecond laser radiation in the intensity regime $10^{11}-10^{13}$ W/cm^2 was presented. By combining the technique of feedback-controlled femtosecond

pulse shaping with time-of-flight (TOF) mass-spectroscopy as well as TOF photoelectron spectroscopy sequential and non sequential excitation pathways were investigated. On the basis of the measured electron energy spectra a non-sequential process is found, which plays an important role in the formation of doubly charged Calcium ions. With optimized phase-only modulated femtosecond laser pulses an absolute 30% enhancement of the double ionization yield was obtained. This increase of double ionization is found to be due to a non-sequential contribution to the Ca^{2+} yield. The observed changes of the electron energy spectrum in the course of the electron optimization lead to the conclusion that a multi resonance control scheme involving the $Ca^{**}(3d^2)$ bound doubly excited state as well as the autoionizing resonances $Ca^{**}(3dnl)$ and $Ca^{**}(4pnl)$ are responsible for the enhanced non-sequential double ionization.

5 Ultrafast dynamics of ethylene-like molecules

5.1 Introduction

In the course of biological evolution nature has developed a number of proteins, the structure of which allows for the efficient conversion and transport of energy in biological systems. A case of particular interest is the protein rhodopsin which is responsible for the fundamental process of vision. Upon the molecular skeleton of rhodopsin a kind of molecular antenna is located, the so-called chromophore, which exhibits an extremely efficient absorption of visible light. Absorption of the light signal results in the ultrafast isomerization of the retinal-chromophor around a specific C=C double bond [154]. This reaction is the primary step in a succession of events that transforms optical signals into electrochemical potential.

The dynamics of the isomerization reaction, for the $all-trans$ to the $13-cis$ ground state conformation of the retinal-chromophor (Fig. 5.1) was first characterized in 1985 by M. C. Nuss and his coworkers [155]. In the following years, the dynamics of this primary $trans \rightarrow cis$ reaction has been studied in different environments, like liquid solutions [156, 157] or protein matrices [158]. Depending on its chemical environment the isomerization reaction can be influenced, as far as the reaction speed and the quantum yield of the reaction is concerned. The subject of this chapter is to investigate the possibility of influencing and eventually controlling the $trans \rightarrow cis$ isomerization around C=C double bonds by modulating the excitation light field that induces the reaction. Following the discussion in Section 2.3.4, absorption of a photon leads to the excitation from the bonding π to the anti-bonding $\pi^\star$ orbital of the ethylenic C=C group, which, in a simplified picture, allows for the free rotation and isomerization of the molecule. When femtosecond laser radiation is utilized for the excitation, a wavepacket is generated upon the excited state potential surface, which leaves the Frank-Condon (FC) region and propagates along the reaction coordinate (ethylenic tortion in the sim-
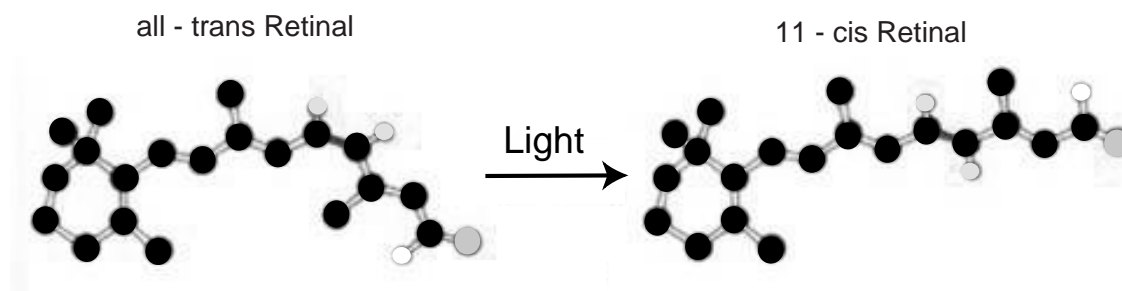
Figure 5.1: The *trans* → *cis* photoisomerization reaction of the rhodopsin chromophor. Absorption of a UV photon leads to $\pi\pi^\star$ excitation of the ethylenic C=C double bond between the 11 and 12 carbon atoms which, in a simplified picture, allows the molecule to rotate. This isomerization reaction constitutes the primary step in the biological process of vision [154].

plest case). At the so-called twisted geometry, the excited electronic state exhibits a strong coupling to the ground electronic state. There, the wave packet funnels back to the ground state. In many cases, the coupling between the ground and the excited electronic states exhibits a conical intersection. This results in an extremely fast isomerization rate. The exact topology of the excited potential surface can be influenced by additional couplings to higher excited electronic states. Determining the potential surfaces of the excited electronic states as well as the coupling mechanisms between them remains one the most challenging topics of modern chemistry. In the above context, two molecules are addressed in this chapter, namely the molecules of stilbene and tetracis-(dimethylamyno)-ethylene (TDMAE). The first constitutes an extensively studied model for isomerization reactions around C=C bonds, while the later is a more complex but experimentally more tractable system to control experiments, as will be shown in the following.

In order to define the target for a potential control experiment, a number of preparative measurements had to be performed. They were realized utilizing the magnetic bottle photoelectron spectrometer described in Section 3.3.4, which was developed for the purposes of this project. The field of femtosecond photoelectron spectroscopy of polyatomic molecules was new for our group, therefore both the spectroscopic techniques, as well as the theoretical basis for interpreting the acquired spectra, had to be developed. In the previous Chapter, a first experimental approach to combine the technique of adaptive femtosecond pulse shaping with photoelectron spectroscopy was presented. By actively

influencing the features of the photoelectron spectrum a totally new understanding about competing excitation mechanisms was achieved. In that experiment, a large amount of information was available, involving the electronic structure of the atomic system. This enabled a rather straightforward interpretation of the measured electron spectra. In polyatomic molecular system, a similar approach would not be possible, since multiphoton transitions in such systems are subject to numerous and broad intermediate resonances. An intuitive interpretation of the resulting photoelectron spectrum is rather forbidden by the complexity of the excitation scheme. From the experimental point of view, the number of intermediate resonances can be reduced when UV laser radiation, with large photon energy, is used for the excitation. Both in stilbene and TDMAE, a $\pi\pi^\star$ transition can be realized by absorption of one 266nm photon. Then, the propagation of the wavepacket upon the excited potential surface can be monitored by a time delayed probe laser pulse through a single or a two photon absorption. From the theory point of view, the collaboration with the theoretical chemists F. Santoro and R. Improta has been of great help in interpreting the experimental results on stilbene. Part of their results, involving theoretical calculations of the electronic structure of stilbene and simulated electron spectra, are also presented in this chapter.

5.2   The molecule stilbene

The chemical structure of stilbene is shown in figures 5.2a and b. It consists of two phenyl rings (C_6H_5) and an ethylene C=C group bound via the conjunction of four $e_{1g}\pi$ phenyl orbitals and one π orbital of ethylene. The ground state of the molecule exhibits two stable geometrical conformations, namely the $cis-$ and $trans-$ isomers. In the electronic ground state, a large energy barrier between the two configurations does not allow the rotation of the molecule around the ethylenic C=C bond. Although a planar conformation would be favored by the delocalization of the electronic wavefunction, the complete planar geometry for the $cis-$ isomer is prevented by the steric interaction between the phenyl moieties. This gives rise also to differences in the electronic structure between the two isomers, as observed in the photoelectron spectra shown in figures 5.2c and d for $trans-$ and $cis-$ stilbene, respectively. These spectra were measured by T. Kobayashi [159] in 1975 utilizing the 584 $\mathring{A}$ emission line of helium as excitation field. The position of the first band A (Fig. 5.2) interestingly differs for the two isomers by almost $300meV$. Based on this spectroscopic observation the idea of using the photoelectron spectrum as feedback signal for a control experiment was born. The kinetic energy
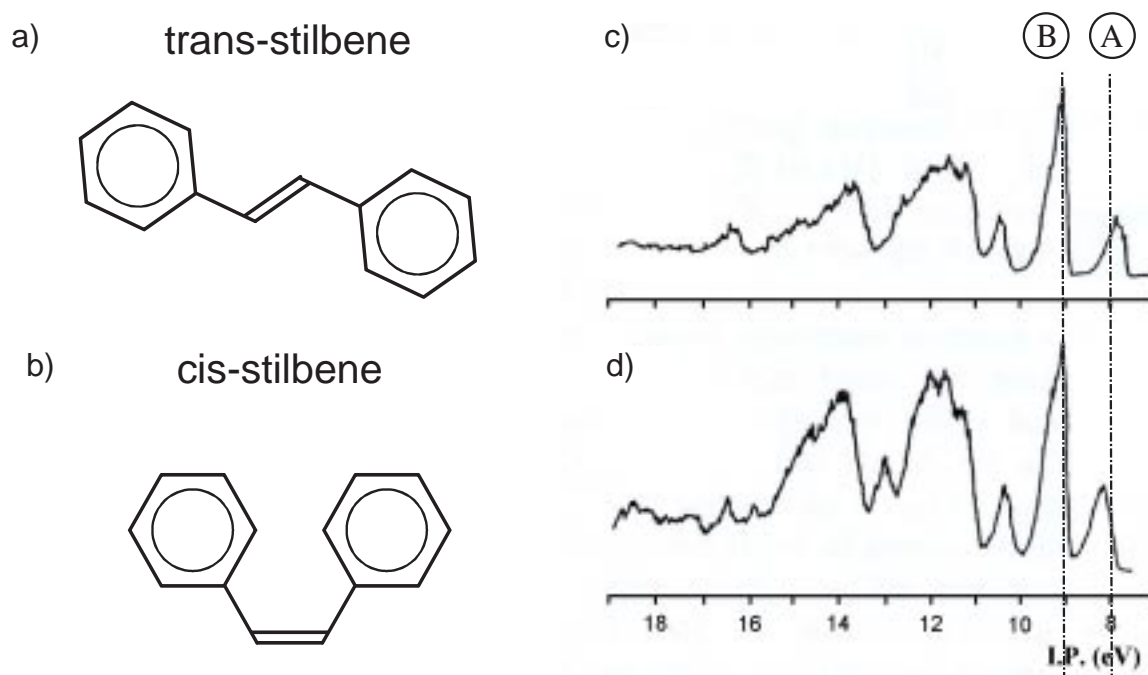
Figure 5.2: The $trans-$ a) and $cis-$ b) geometrical conformation of stilbene ground state. Photoelectron spectra of $trans-$ c) and $cis-$ stilbenes d) following one photon ionization, using a $584\mathring{A}$ helium resonance line as excitation source [159]. The vertical dashed lines A and B indicate the differences in the spectra of the two isomers, originating mainly from the steric effect between the phenyl moeities.

of the electrons originating from $trans-$ or $cis-$ stilbene could be used as feedback signal for optimizing the formation of a specific photoproduct. Nevertheless, when comparing the photoelectron spectra shown in Fig. 5.2 with those where ultraviolet femtosecond laser radiation is used for the excitation, it has to be noted that in [159] ionization is achieved in a one-photon excitation scheme, while for the 266nm exciation an intermediate step is needed (two-photon transition). In two recent studies of the photoelectrons spectrum of $trans-$stilbene [160,161] employing the *Zero Kinetic Energy* (ZEKE) spectroscopy, a two-photon ionization scheme was investigated. There, the first excited S_1 state of stilbene, originating from the bonding-antibonding $(\pi\pi^\star)$ transition, was used as intermediate resonance for the two-photon transition to the molecular continuum.

From earlier spectroscopic studies, the topology of the first excited S_1 state of $trans-$stilbene is known to exhibit a potential minimum and a barrier, which effect the twisting motion about the ethylene bond [162] (Fig. 5.3). Following the explanation proposed by Orlandi, Siebrand and others [163, 164], the potential barrier arises from the interaction of S_1 with a higher excited surface that exhibits a minimum at the perpendicular $(\theta = 90°)$ configuration. When the excitation energy exceeds the 1200
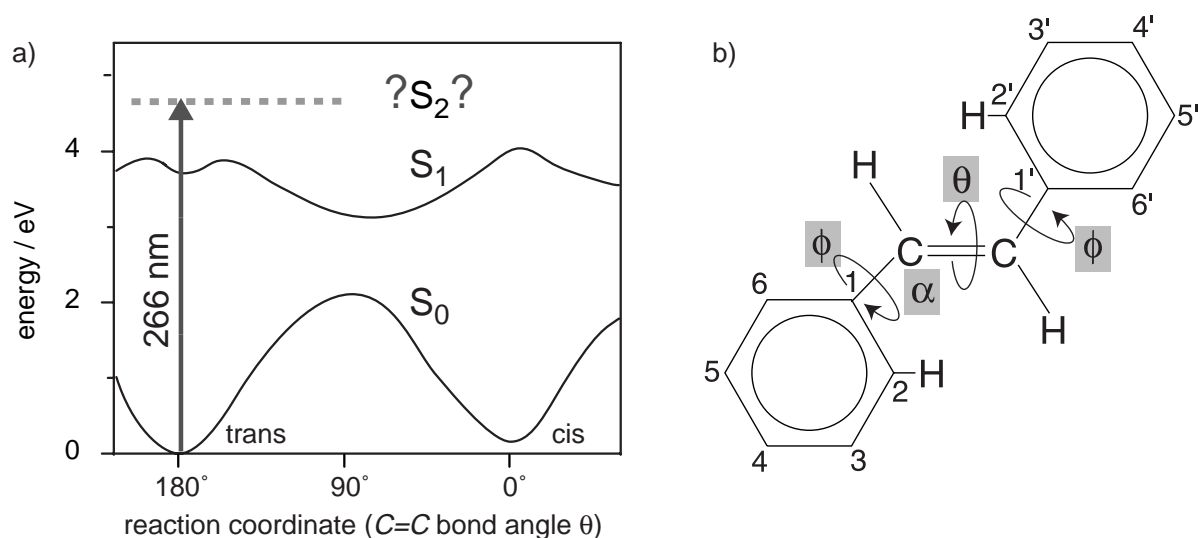
Figure 5.3: a) Energy scheme of the $trans \rightarrow cis$ isomerization of stilbene. The approximate shape of the potential surfaces of the ground S_0 and first excited S_1 state [163]. Following absorption of a 266nm photon a wavepacket is excited in the energy region high above the reaction barrier of the $trans-$ configuration. A second excited S_2 state is theoretically predicted [179] in this energy region. b) Three torsion coordinates α, ϕ, θ are believed to play an important role during the isomerization reaction of stilbene. At the perpendicular ($\theta = 90°$) configuration the wavepacket undergoes a nonradiative transition from the excited S_1 to the ground S_0 surface.

cm^{-1} barrier, the twisting motion about the ethylene bond brings the molecule toward the $\theta = 90°$ configuration (Fig. 5.3). Then, due to the S_0/S_1 conical intersection, the molecule undergoes a nonradiative transition to the ground S_0 surface. The lifetime of the excited S_1 state lies in the range of several picoseconds and decreases as a function of the excitation energy [166]. Various experimental schemes has been employed to measure the lifetime of the excited S_1 state [167, 168].

On the other hand, the isomerization reaction from the $cis-$ to the $trans-$ configuration of stilbene exhibits practically no barrier on S_1. Consequently, the isomerization time-constant starting from the $cis-$ configuration is orders of magnitude shorter (320fs for excitation with 312nm [169]) than in $trans-$stilbene. The peculiarity of the excited state topology of $cis-$stilbene can be explained on the basis of the steric interaction between the phenyl moeities mentioned earlier. For $cis-$stilbene, the electronic excitation to S_1, apart from the twisting motion about the ethylene bond, involves a second isomerization coordinate. This has a large contribution to the twisting around the angle α (Fig. 5.3), and the two phenyl moeities approach each other until a bridge between C_2 and C_2' atoms is formed. The emerging product of this photocyclization reaction is the so-called dihidro-phenantrene (DHP) (Fig. 5.4b). The $cis \rightarrow DHP$ reaction has
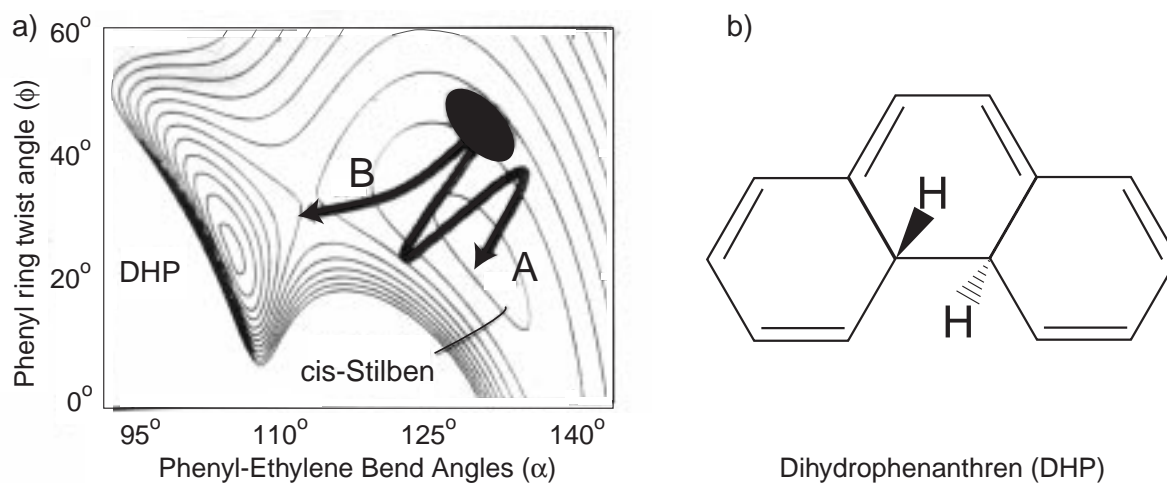
Figure 5.4: a) Model map of the S_1 potential surface along the phenyl-ethylene bend angle α and the phenyl ring twist angle ϕ [170]. The electronic excitation from the ground S_0 states generates a wavepacket upon the S_1 in the area marked with the black ellipse. The thick black arrows A and B represent the motion along the *cis* $\rightarrow$ *trans* and *cis* $\rightarrow$ DHP reaction coordinates respectively. b) The chemical structure of the photocyclization reaction channel dihydrophenantrene (DHP) is presented.

been extensively investigated both experimentally as well as theoretically [170,171]. The reported isomerization time-constant [169] is slightly shorter than in the *cis* $\rightarrow$ *trans* reaction. A plausible explanation is provided by the theoretical model [170] shown in Fig. 5.4 a. There, a map of the skeletal motion of the stilbene molecule is depicted along the phenyl-ethylene bend angle α and the phenyl ring twist angle ϕ. The reaction coordinates leading to formation of the *trans* and DHP isomers are represented by the two thick black arrows. The channel leading to DHP exhibits a rather straight motion in the direction of the final product, which could explain the relative speed of the two isomerization channels.

In previous studies, utilizing time resolved fluorescence [172], absorption spectroscopy [173] as well as zero kinetic energy (ZEKE) photoelectron spectroscopy measurements [160,161], a large amount of spectroscopic information, involving the ground S_0, the first excited S_1 as well as the ground ionic D_0 states of stilbene, was accumulated. However, in the energy region above the isomerization barrier, the spectroscopic information up to date is rather limited. In this region, the fast intramolecular vibrational redistribution (IVR) reduces severely the analytical ability of the spectroscopic methods mentioned above. Additionally, theoretical calculations [174,175,179] as well as experimental studies performed on similar molecular systems [176–178] raise a question concerning the presence of higher excited electronic states in this energy region and the coupling of

electronic state	energy eV	occupation of the orbitals					statistical weight %
		$5b_g$	$6a_u$	$7a_u$	$8b_g$	$9b_g$	
$S_0(1^1A_g)$	0.00	2	2	2			100
$S_1(1^1B_u)$	4.00	2	2	1	1		100
$S_2(2^1B_u)$	3.93	2	1	2	1		49
	4.43	2	2	1		1	51
$D_0(^2A_u)$	7.6	2	2	1			100

Table 5.1: Molecular orbital configuration of the ground and the two first excited states of $trans-$stilbene as well as the ground cationic state, following the TD-DFT calculations from R. Improta and F. Santoro [179].

those to the S_1 state. This spectroscopic information is vital to understand the excited state dynamics of stilbene and its isomerization reaction. In the recent theoretical TD-DFT calculations by R. Improta and F. Santoro [179] a second S_2 $1B_u$ electronic state is predicted in the vicinity of 4.62 eV. As summarized in table 5.1 the S_1 state corresponds mainly to a HOMO $\rightarrow$ LUMO excitation, while S_2 can be described by a combination of the HOMO $\rightarrow$ LUMO+1 and HOMO-1 $\rightarrow$ LUMO excitations. Both S_1 and S_2 are of $1B_u$ symmetry and can be reached from S_0 ($1A_g$) with a single photon transition. Nevertheless, the S_1 is strongly absorbing (the TD-DFT oscillator strength at the Frank Condon (FC) geometry is 0.93) while S_2 is weakly absorbing (oscillator strength 0.02). The experimental observation of the second excited S_2 state has not been previously reported.

5.3 Femtosecond photoelectron spectroscopy of $trans-$stilbene

The photoelectron spectrum of trans-stilbene following the excitation with 266 nm laser pulses is shown in Fig. 5.6a. $Trans$-stilbene was evaporated at a temperature of about $70°$C and coexpanded with the inert carrier gas Argon (1bar pressure) through a nozzle. The molecular beam was skimmed and directed through the pole-pieces of the magnetic bottle electron spectrometer where it intersected perpendicularly with the laser beam. The spectrum consists of a pronounced three-peak structure (peaks $\epsilon_1 - \epsilon_3$ in Fig.5.6a), which are subject to a substantial broadening, due to the large number of closely spaced vibrational states involved in the excitation scheme. Each of these peaks corresponds
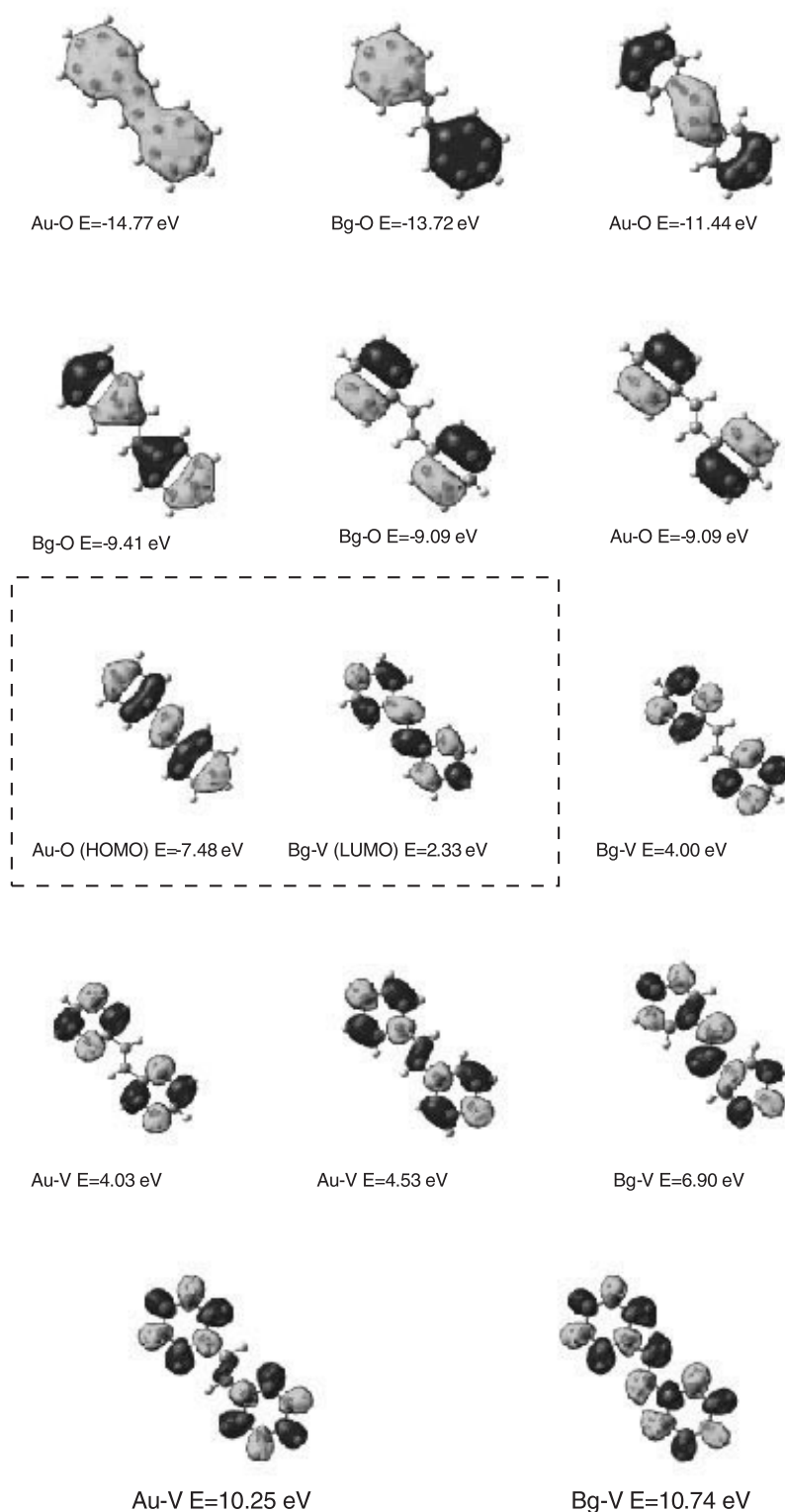
Au-O E=-14.77 eV   Bg-O E=-13.72 eV   Au-O E=-11.44 eV

Bg-O E=-9.41 eV   Bg-O E=-9.09 eV   Au-O E=-9.09 eV

Au-O (HOMO) E=-7.48 eV   Bg-V (LUMO) E=2.33 eV   Bg-V E=4.00 eV

Au-V E=4.03 eV   Au-V E=4.53 eV   Bg-V E=6.90 eV

Au-V E=10.25 eV   Bg-V E=10.74 eV

Figure 5.5: Molecular orbitals of $trans-$stilbene calculated by R. Improta and F. Santoro in a $HF/6-31G^{\star}$ theory level. The HOMO($7a_u$), LUMO($8b_g$) orbitals involved in the $\pi\pi^{\star}$ excitation are indicated with a dashed frame.
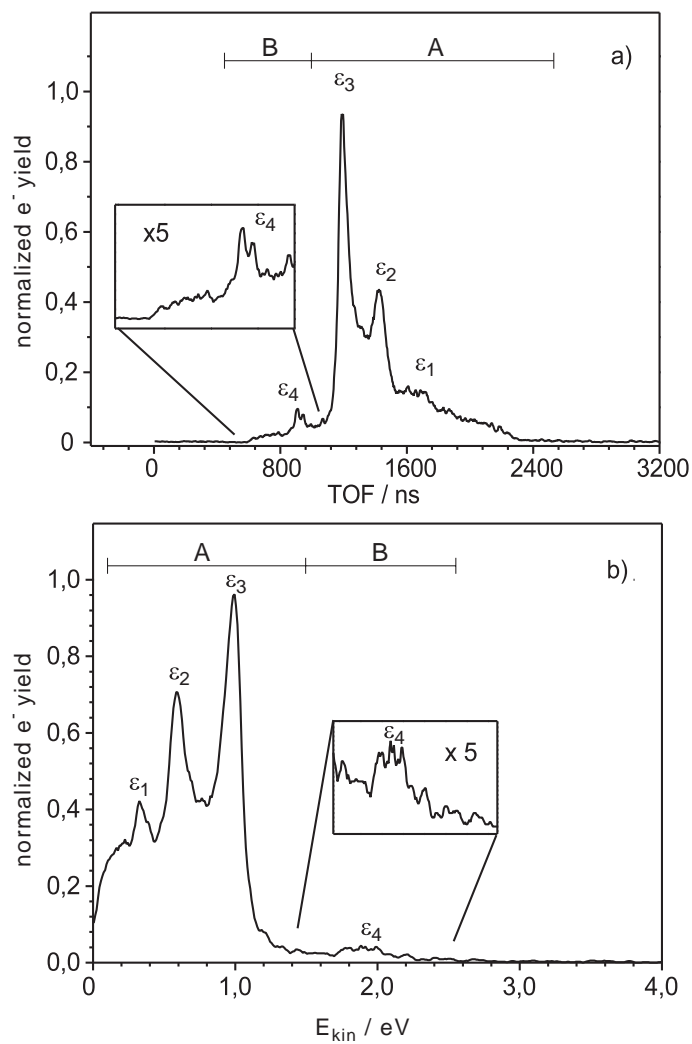
Figure 5.6: a) Time-of-flight photoelectron spectrum of *trans*-stilbene following the excitation with 266 nm femtosecond laser pulses. b) calibrated spectrum.
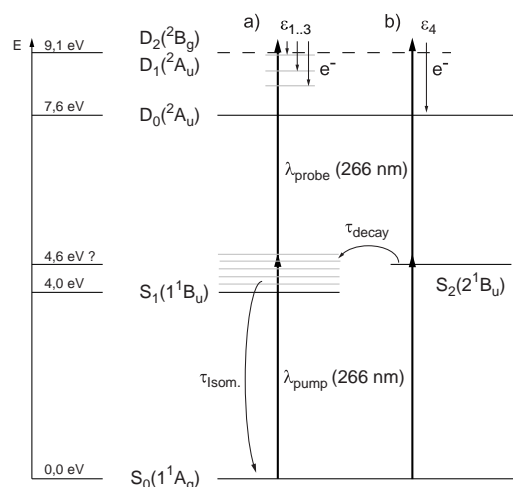
Figure 5.7: Energy diagram for the pump-probe spectroscopy. After a pump-photon excitation to the energy region above the reaction barrier with a 266 nm femtosecond laser pulse, the dynamics of the induced wavepacket is explored with a time-delayed second 266 nm probe laser pulse by measuring the kinetic energy of the emitted photoelectrons. The major contribution in the photoelectron spectrum results from the path via the S_1-state (a). But apart from that contribution, in the measured transient spectra evidence of a second electronic state is found to play a role (b).

to a kinetic energy which is determined by the total energy of the level reached in the two-photon absorption and the vibronic state at which the parent ion is left after the ionization. As seen in the calibrated spectrum (Fig. 5.6b), the spacing of these states comply with periodicity of about 3000 cm^{-1} and 1600 cm^{-1} which, according to previous studies [166], could fit with progressions along the C-H-stretching and C-C-stretching modes of the cationic D_0-state. In the context of the 1+1 resonance enhanced scheme, the excitation energy following the absorption of a 266 nm photon exceeds the origin of the S_1 intermediate by almost 0,7 eV (Fig. 5.7). Subsequently, the transition is resonantly enhanced by the excited vibrational levels of the S_1 band. Following the absorption of a second 266 nm photon, the molecule is ionized with the maximum probability of leaving the parent ion in an excited vibrational state of D_0. This is due to the Franck-Condon correlation between the S_1 and D_0 vibrational levels. For this reason, as shown in Fig. 5.6b, the maximum electron yield reached in the photoelectron spectrum corresponds to a kinetic energy of ≈ 1 eV. This is substantially less than the observed 1,7 eV, which would result from ionization to the origin of the cationic D_0-state. Nevertheless, there is a small contribution in this energy region (peak ϵ_4) which could be either assigned to an ionization from the highly excited S_1-levels to D_0, or via a second electronic state, whose origin is located closer to the one-photon 266 nm
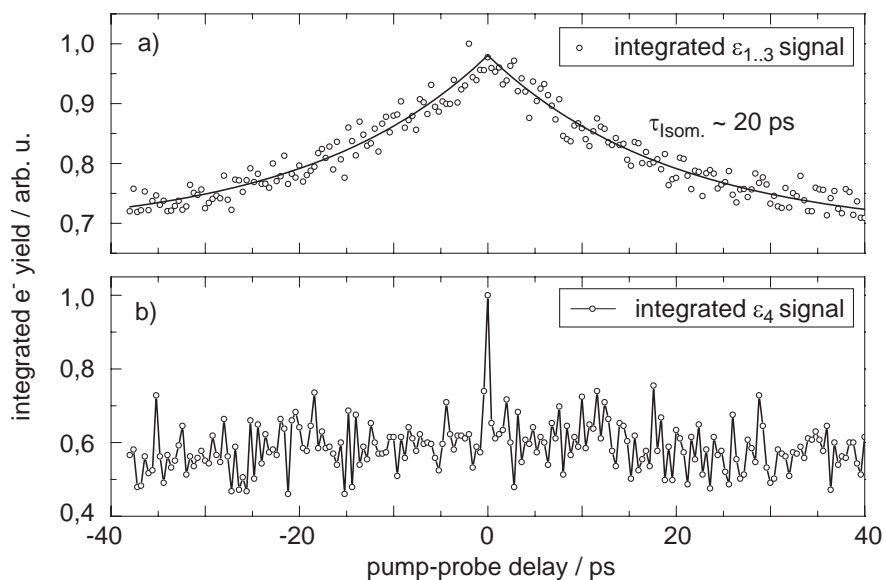
Figure 5.8: Transient photoelectron yield integrated (a) over the area A from Fig.5.6 (open circles) and (b) over the area B from Fig.5.6 (connected circles) for pump-probe delay times between -40 ps and +40 ps in steps of 400 fs. The signal is normalized to the maximum photoelectron yield. For the transient ionization signal in (a), an exponential decay was fitted, with a time constant of $\tau_{decay} = (19 \pm 1)$ps (solid line).

absorption, also ionizing into the D_0. So far, such a second electronic state (S_2) has never been experimentally observed in trans-stilbene but it has been seen about 0,6 eV above the S_1 origin in two closely-related molecules [178].

In order to distinguish between the two possibilities, time-resolved pump-probe measurements were conducted. The presence of a second electronic state, which in the general case would exhibit a different lifetime than S_1, would also result in a different time dependence of the ionization signal. The integrated electron yield of the major three-peak component (peaks $\epsilon_1 - \epsilon_3$, area A in Fig. 5.6a) in the photoelectron spectrum is shown in Fig. 5.8a as a function of the delay time between the pump and probe pulses. The delay time ranges between -40 ps and +40 ps in steps of 400 fs. Since both pump and probe were identical 266 nm laser pulses the measured transients are symmetric with respect to the time when the pump and the probe pulse overlap temporally (time zero). From both sides of time zero an exponential decay of the ionization signal was found , with a time constant of $\tau_{decay} = (19 \pm 1)$ ps. This is in good agreement with the 20 ps time constant reported earlier by [166] and [168], which they related to the photoisomerization of trans-stilbene via excitation of the S_1 state. This agreement confirms the assignment of the three-peak component (peaks $\epsilon_1 - \epsilon_3$) in the photoelectron spectrum to be due to the ionization via the S_1-state. In Fig. 5.8b, the corresponding
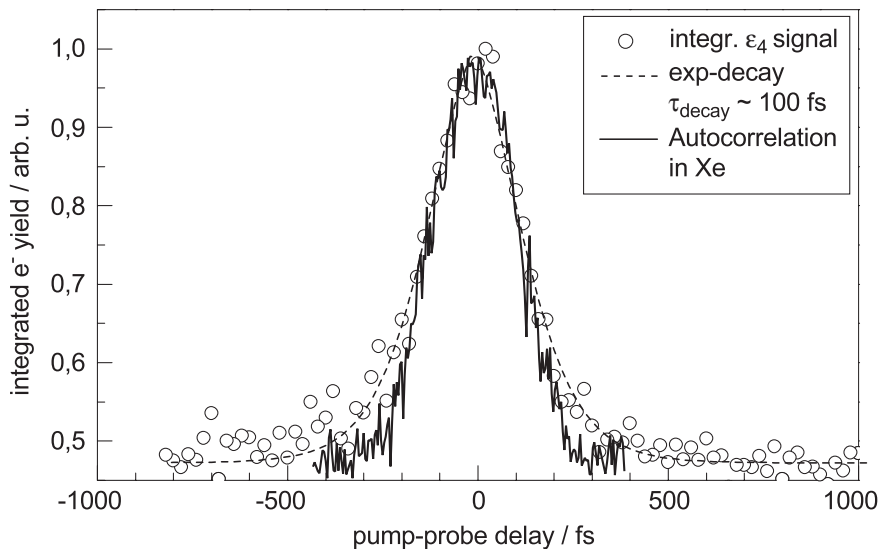
Figure 5.9: Transient integrated photoelectron yield of the component at 1,7 eV (peak ϵ_4 in Fig.5.6) for a smaller pump-probe interval in steps of 20 fs. The transient ionization signal shows a decay time on a femtosecond time scale. The data was fitted with an exponential decay convoluted with the pump-probe pulse cross-correlation. Additionally, a crosscorrelation between the pump- and probe-pulse in a static ionization cell filled with xenon was measured (solid line). There, a pronounced deviation from the data for larger pump-probe delay times is visible.

transient of the integrated electron yield of the component at 1,9 eV (peak ϵ_4, area B in Fig. 5.6a) is shown. The signal shows almost no time dependence except for a peak at time zero. To ensure that this result is no experimental artifact, the transient of peak ϵ_4 was also recorded for a smaller pump-probe interval in steps of 20 fs as shown in Fig. 5.9. In this case, the ionization signal exhibits a decay time on a femtosecond timescale, in contrast to the dynamics of the S_1-state which takes place on a picosecond timescale.

To prove that the fast dynamics observed were not due to an intensity effect, when the pump and probe pulses overlap, a crosscorrelation between the pump- and probe-pulse was measured in a static ionization cell filled with xenon, parallel to the electron transients (Fig. 5.9 solid line). There, a pronounced deviation between the two transients for larger pump-probe delay times is visible. The transient signal of the ϵ_4 peak was fitted with an exponential decay convoluted with the cross-correlation between the pump and the probe laser pulse. For this fit-function, the exponential decay component exhibits a time constant of about 100 fs, while the cross correlation term a width of 260 fs. It has to be noted that since for ionization of xenon at least three photons are needed, this results in a shorter cross-correlation function (250 fs) for the pump and the probe laser pulses than in the case of a two photon transition, if dispersion effects inside the static
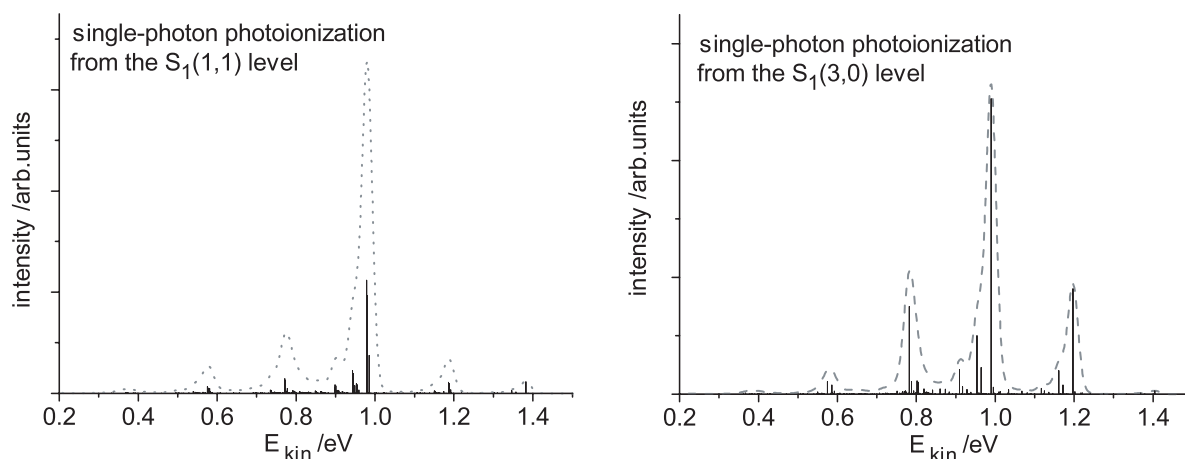
Figure 5.10: Simulation of photoelectron spectra of trans-stilbene from the $S_1(3,0)$ and the $S_1(1,1)$ levels (where the two numbers are respectively the C-C and C-H number of quanta) by a single 266nm photon. The S_1 origin is fixed at 4.00 eV in agreement with the experiment.

gas cell are not taken into account. Nevertheless, the lack of the exponential decay component in the transient of the xenon ionization provides conclusive evidence that the femtosecond time dependence of the stilbene signal is indeed not due to a coherent artifact. On this basis it can be concluded that the ϵ_4 peak is coming from a two-photon ionization very close to the origin of D_0. Its fast temporal decay, about 200 times faster than that of the $\epsilon_1 - \epsilon_3$ ones, strongly suggests it is the result of ionization through a second electronic state which lies higher in energy than S_1.

To support the above scenario, Harmonic Franck-Condon spectra have been computed in the full space of the 72 normal modes, including position- and frequency-shifts and Duschinsky mixings, by the method discussed in Ref. [180]. In the FC approximation the ionization spectra of the states $S_1(3,0)$ and $S_1(1,1)$ (in parenthesis the number of quanta on the C-C and C-H stretching, respectively) by a 266nm photon were computed. The results reported in Fig. 5.10 show that the highest bands of both spectra is at about 1.0 eV, in agreement with the experiment, corresponding to an ionization to D_0 in the same vibrational state as the S_1 initial one. By the simulation of the photoionization spectra of excited S_1 levels no band appears in the energy region of ϵ_4. The TD-DFT calculations indicate that the electronic state which can play this role is S_2 for which the computed adiabatic energy distance $S_2 - S_0$ is 4,51 eV only slightly below the 4,67 eV energy quantum delivered by a 266nm photon. These results suggest that the 266 nm photon should excite the S_2 state very close to its origin, with an oscillator strength of 0.02, much lower than the 0.93 value computed for the $S_0 \rightarrow S_1$. In Fig. 5.11, a simulation of a one-photon photoelectron spectrum with a 266nm photon of a
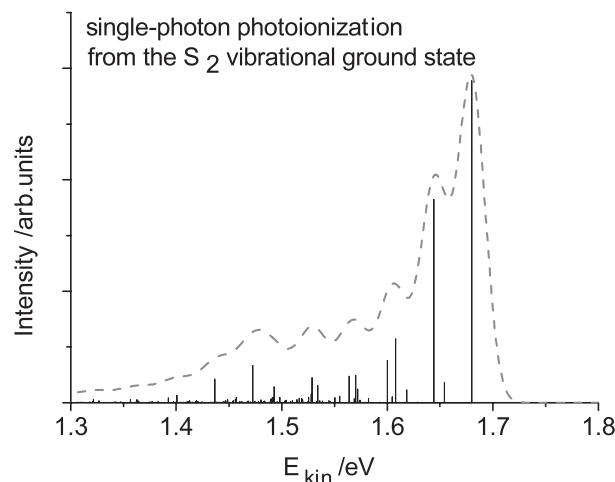
Figure 5.11: Simulation of a photoelectron spectrum of trans-stilbene from the ground vibrational S_2 level excited by a single 266nm photon.

trans-stilbene molecule lying initially in the ground vibrational state of S_2 is presented. The spectrum exhibits a peak around 1,7 eV, an energy content clearly higher than the $S_0 \rightarrow S_1$ contribution and extends only for about 0,2-0,3 eV.

5.4 Theoretical calculations on isomerization dynamics of $trans-$stilbene

The ϵ_4 peak decays with a time constant of about 100 fs. This could be due to a direct isomerization on the S_2 surface or to a nonradiative reaction to another electronic state. To investigate the plausibility of the first hypothesis, the energy profiles on the three surfaces S_0, S_1, and S_2 along the reactive $C_1 - C_1'$ torsional angle are shown in Fig. 5.12, keeping frozen all the other coordinates at the equilibrium values of the S_0 state (full lines), of the S_1 state (dash lines) and of the S_2 state (dot lines). Fig. 5.12b shows that there is a barrier to the reaction on all the three surfaces. Interestingly, the motion along the reactive coordinate requires clearly more energy (and hence is slower) on S_2 than on S_1. Since the reaction on S_1 takes place on the timescale of tens of picoseconds, it can be safely assumed that on S_2 it cannot be so fast to explain the 100 fs time decay of the ϵ_4 peak. Excluding the direct isomerization reaction on S_2, the fast decay of ϵ_4 must be addressed to a nonradiative transition, a very common and fast phenomenon in highly excited electronic states (Section 2.3.3). The characterization of the precise mechanism of such a transition is a very hard task. It could involve the S_3 state which
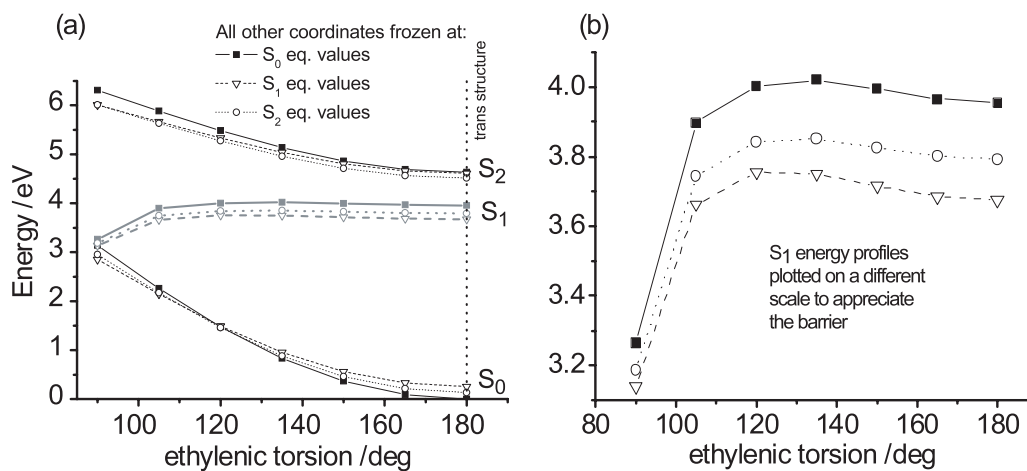
Figure 5.12: (a) Energy profiles on the S_0, S_1, and S_2 surfaces along the ethylenic torsion. All the other coordinates are fixed at the equilibrium values of: S_0(full lines, squares), S_1 (dashed lines, triangles), and S_2 (dotted lines, circles). (b) For comparison, this graph reports the profiles on S_1 to make visible the barriers.

is very close in energy to S_2 and has the right symmetry to have a conical intersection with it at C_{2h} geometries. Also, the S_1 state, at the considered excitation energies, has a vibrational states density large enough to cause a fast and irreversible $S_2 \rightarrow S_1$ decay. This considered $S_2 \rightarrow S_1$ transition could not be experimentally observed, since it would cause an undetectable signal variation of the ϵ_1 to ϵ_3 peaks of the spectrum, as a consequence of the very low population initially on S_2.

5.5 Femtosecond photoelectron spectroscopy of $cis-$stilbene

The time-of-flight photoelectron spectrum of cis-stilbene following the excitation with 266 nm laser pulses is shown in Fig. 5.13 (grey curve). This spectrum was measured using the same parameters for the excitation field as in the case of $trans-$stilbene. In Fig. 5.13 the photoelectron spectra of the two isomers are presented for comparison, where a similar structure (peaks $\varepsilon_1, \varepsilon_2, \varepsilon_3$ and ε_4) is observed for both spectra. A pronounced difference is evident in the right part of the spectrum where the contribution from peaks ε_1 and ε_2 is clearly enhanced for the cis isomer. Such a variation could be due to a significant change of the equilibrium C-C and C-H distances in the S_1 and D_0 configurations. Also, for the cis-stilbene a weak contribution in the vicinity of peak ε_4 is evident. The transient signals of the integrated electron yield (Fig. 5.14) from the
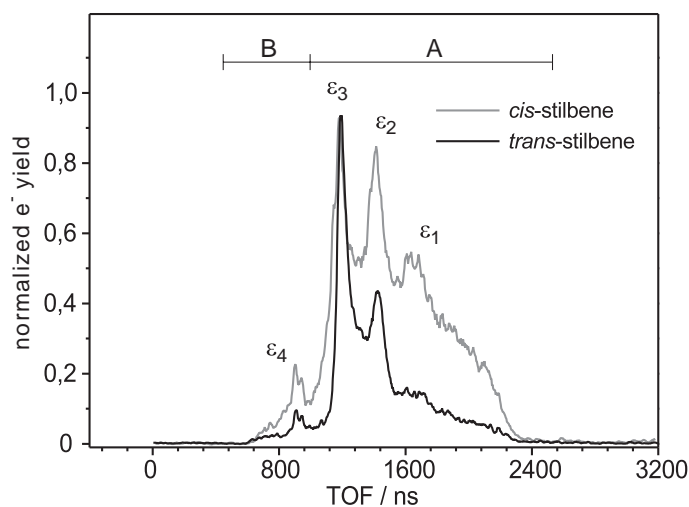
Figure 5.13: Time-of-flight photoelectron spectrum of *cis*-stilbene (gray curve) following the excitation with 266 nm femtosecond laser pulses. The corresponding spectrum of *trans*-stilbene (black curve) is also shown for comparison. Both spectra are normalized to the maximum peak height. A quantitative comparison is limited by the uncertain particle density for the two measurements.

areas A and B, as defined in Fig. 5.13, contribute to the argumentation that the ε_4 peak originates from the second excited electronic state S_2. Both transients shown in Fig. 5.14 exhibit a decay with a time constant in the femtosecond time scale (about 150 fs for area A and 80 fs for area B). As previously mentioned, the topology of the S_1 excited state and for the *cis* configuration exhibits practical no potential barrier along the isomerization reaction coordinate. This gives rise to the large difference of the decay time constants (150 fs and 19 ps) in the transients of the two stilbene isomers.

5.6   The molecule Tetrakis-Dimethylamino-Ethylene (TDMAE)

In the previous sections the dynamics following the electronic excitation of molecular stilbene in the vicinity of the $\pi\pi^\star$ resonance were investigated. The transient photoelectron spectra there exhibit an exponential decay time dependence. By the appropriate analysis of the decay time constant new information was provided, concerning the coupling mechanisms of the excited potential energy surfaces. However, no significant structural changes were observed in these measurements, like a drastic shifting of the electron peaks or new peaks appearing after specific time delays, to indicate the formation of new isomerization products ($cis \rightarrow trans, trans \rightarrow cis$).
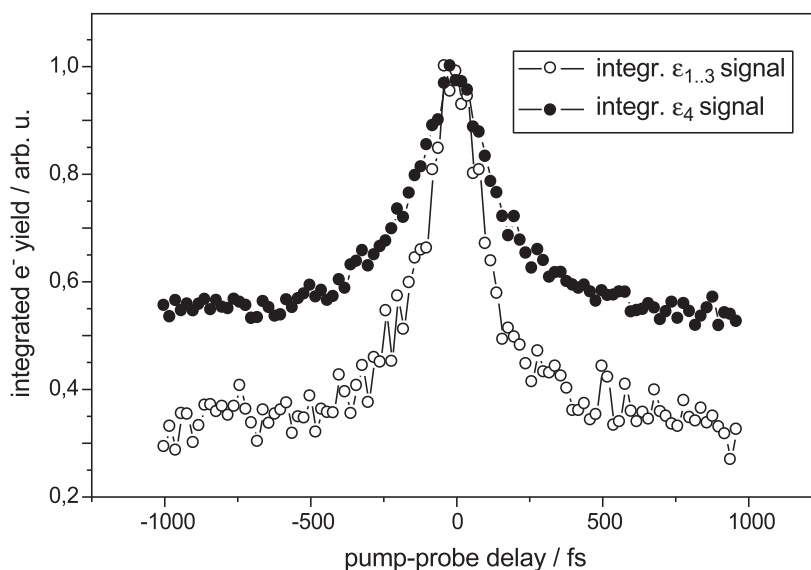
Figure 5.14: Pump-probe transient of the integrated photoelectron yield of peaks $\varepsilon_1, \varepsilon_2$ and ε_3 (filled circles) and peak ε_4 in Fig. (open circles). Both transient ionization signals shows a decay time on a femtosecond time scale with a different decay constant.

However, such effects were reported by B. Soep [181] for another ethylenic product, namely the molecule tetrakis(dimethylamino)ethylene (TDMAE) (Fig. 5.15b). The electronic structure of TDMAE consists of a central ethylene group (Fig. 5.15a) upon which four dimethylamino ($N(CH_3)_2$) moeities form symmetric π bonds. Compared to stilbene, TDMAE is not so frequently used as model in isomerization studies, due to its evidently more complex chemical structure and also because it's cis- and trans- isomers are degenerate.

TDMAE was synthesized for the first time in 1950 by R. L. Pruett [182] and attracts an increasing interest because of its property to form ferromagnetic complexes with Fullerenes [183, 184]. This extraordinary property is due to the large number of lone-pair electrons from the amino groups that are easily extracted from the molecule. This results in a remarkably low electron affinity (the adiabatic and vertical ionization potentials of TDMAE are reported at 5,36 eV and 6,11 eV respectively [185]). In the first chemiluminesence studies by H. E. Winberg [186] a (local) absorption maximum was observed at 265 nm. The complete absorption spectrum of TDMAE was then measured by Y. Nakato [185] (Fig. 5.16 a). In this graph the peak progression, labeled 1, 2, 3 originates from Rydberg transitions at low photon energies. These are superimposed with the broad absorption of the $\pi\pi^\star$ resonance, indicated by a dashed line.

The excited S_1 surface of TDMAE exhibits mainly a $\pi^\star$ valence character, but is
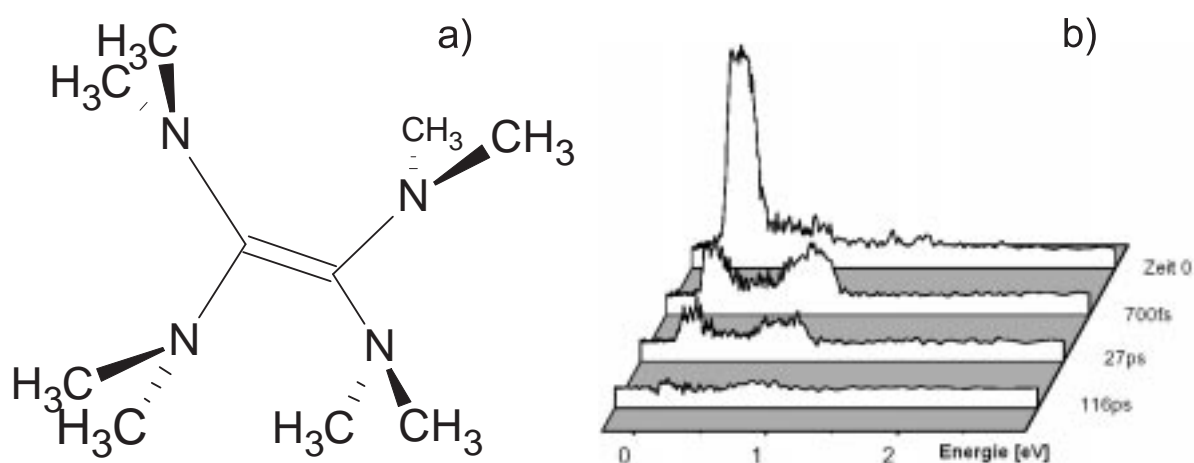
Figure 5.15: a) Chemical structure of tetrakis(dimethylamino)ethylene (TDMAE). Four dimethylamino ($N(CH_3)_2$) moeities form symmetric π bonds upon the central ethylene group. b) Photoelectron transient measurements utilizing a 266 nm pump- 800 nm probe- excitation scheme, reported by B. Soep et.al. [181]. Following the electronic excitation in the vicinity of the $\pi\pi^\star$ resonance, a clear indication for the formation of a photoproduct is observed (The electron peak at 1 eV appears after 700 fs pump-probe delay time).

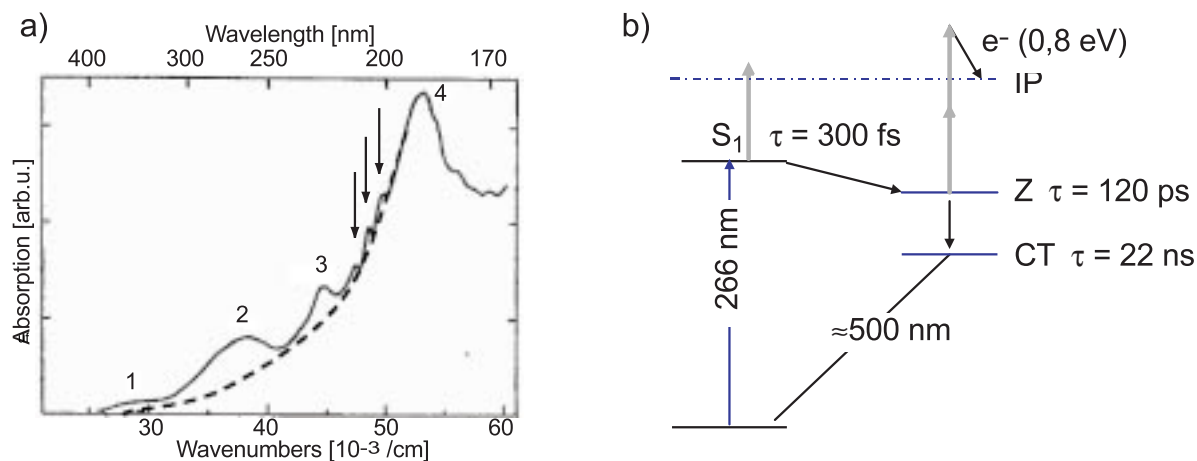**Figure 5.16:** a) The presumed absorption spectrum of TDMAE in the gas phase, adapted from Y. Nakato [185]. A Rydberg progression labeled 1, 2, 3 converges towards the IP at 5.4 eV. The contribution of the $\pi\pi^\star$ transition is indicated by a dashed line. b)Schematics of the pump probe scheme realized by B. Soep [181]. The coupling mechanisms between the excited S_1, Z and CT states are addressed in the text.

also influenced by the coupling to the embedded Rydberg manifold. As in the case of stilbene, the $\pi\pi^\star$ excitation of the central ethylenic group results in the torsional motion around the C=C axis of the molecule. Following the discussion in Ref. [181], the initially populated surface S_1 (Fig. 5.16b) is coupled to a second doubly excited (zwitterionic) state Z via a conical intersection, giving rise to a femtosecond decay of the S_1 state. The zwitterionic state Z consists of two degenerate configurations and lays energetically below the V state. State Z is further subsequent to a non-radiative decay to a lower charge-transfer-state (CT) (Fig. 5.16b) due to the interactions of the numerous lone pair electrons in the amino groups. The CT state finally fluoresces back to the ground electronic state with a rather long (22 ns) life time [181].

In the experiments by Soep et.al., femtosecond photoelectron spectroscopy was employed in order to measure the time constants of the coupling mechanisms involved in the above excitation scheme. The transients photoelectron spectra in Fig. 5.15b exhibit two major trends: a) The electron signal for kinetic energies between 0 eV and 0,8 eV is maximal when both pump- (266 nm) and probe- (800 nm) pulses overlap (time zero), and decays exponentially with a time constant of 300 fs. This is the lifetime of the initially excited S_1 state via the conical intersection funneling to Z. b) The electrons signal between 0,6 eV and 1,0 eV exhibits an up-rise time of 300 fs, followed by a slow exponential decay with a time constant of 120 ps. The later signal results from probing of the population from the Z state to the ionization continuum via absorption of two 800 nm photons (Fig. 5.16b).
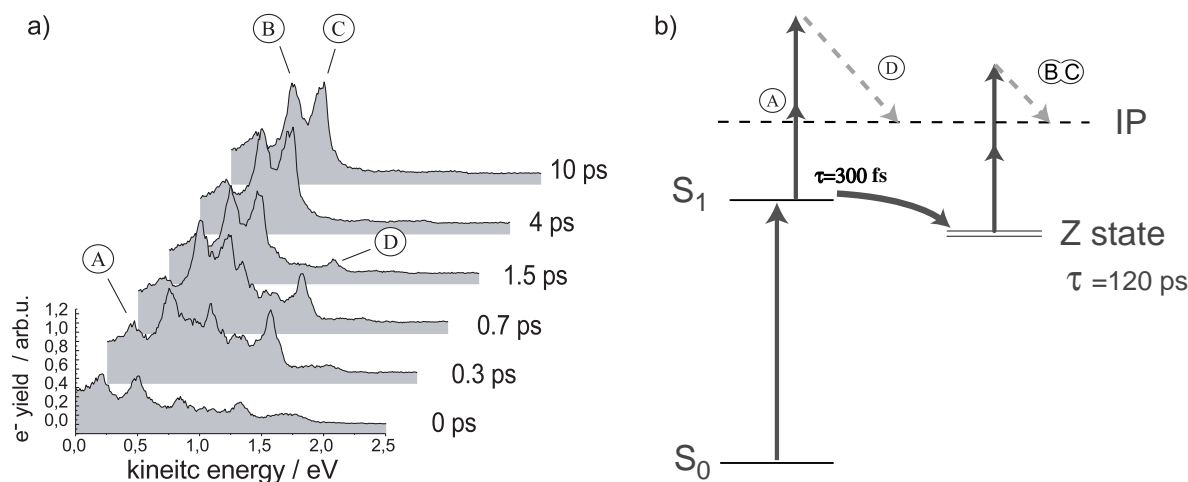
Figure 5.17: a)Transient photoelectron spectra of TDMAE utilizing a 266 nm pump- 800 nm probe excitation scheme. A clear indication of growing photoproducts (peaks B and C) is evident from the transient measurements, while peaks A and D exhibit a fast decay within a subpicosecond time range. b) Simplified energy diagram of the TDMAE excitation pump-probe scheme. The dashed arrows indicates the plausible origin of the peaks A...D observed in the transient spectra. For channel A, no dashed arrow is drawn since the one photon excitation from the S_1 state lies close to the ionization threshold. This channel gives rise to the slowest photoelectron peak A.

5.7   Femtosecond photoelectron spectroscopy of TDMAE

To use the above findings from Soep for conducting an adaptive control experiment on TDMAE, the pump-probe scheme realized in [181] was repeated. However, it has to be noted that the energy resolution of the magnetic bottle spectrometer, used for the measurements here, clearly prevails the one from the linear-TOF spectrometer utilized in the reference. Also, differences in laser field intensity and the pulse duration of the excitation pulses can lead to deviations. In order to achieve the desirable contrast of the pump-probe signal 1,8 mW of the third harmonic 266 nm and 19 mW of the fundamental 800 nm were used for the pump- and probe- pulses, respectively. The photoelectron transient spectra were recorded within a time window from -200 fs to 1500 fs, divided into steps of 50 fs. Since the decay of Z state takes place on the picosecond timescale, additional transient spectra were acquired up to a delay time of 10 ps with intervals of 500 fs. The recorded transients are shown in Fig. 5.17 together with an explanatory energy diagram of the pump-probe excitation scheme.

The slowest component of the electron spectrum (Peak A), which in the measurements by Soep was the major contribution in the early pump-probe times, appears here
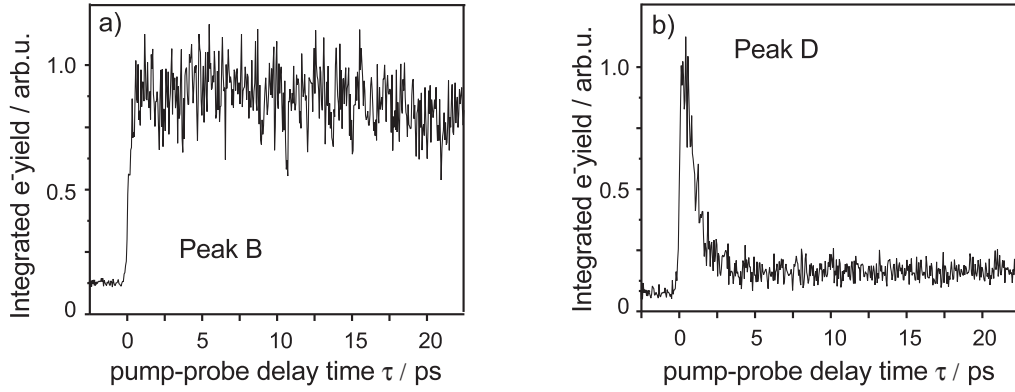
Figure 5.18: Pump-probe transients of the integrated electrons signal from peaks B (left) and D (right). The subpicosecond decay of peak D $(\tau_{decay(D)} = (830 \pm 60)fs)$ indicates a fast depopulation of the initially excited potential surface, while the evident slower up-rise $(\tau_{rise(B)} = (160 \pm 50)fs)$ and decay $(\tau_{decay(B)} = (80 \pm 10)ps)$ of peak B indicate the formation of a new photoproduct.

rather suppressed. However, it exhibits an exponential decay with a time constant of $\tau_{decay(A)} = (370 \pm 100)fs$ which matches the lifetime reported in the reference. The large statistical error in determining the time constant originates from the weak photoelectron signal to this peak. Nevertheless, the comparison can still be conclusive.

The photoelectron peaks B and C show a completely different transient behaviour, namely a rise time of $\tau_{rise(B)} = (160 \pm 50)fs$ and $\tau_{rise(C)} = (290 \pm 60)fs$ and slow decay constants $\tau_{decay(B)} = (80 \pm 10)ps$, $\tau_{decay(C)} = (130 \pm 20)ps$, respectively. The kinetic energy of these two peaks matches with the broad photoelectron contribution observed at 1 eV kinetic energy by Soep (Fig. 5.15b). The later was reported to decay with a time constant of 120 ps. Evidently, the double peak structure could not be resolved in the measurements by Soep due to the limited resolution of the linear-TOF spectrometer employed there.

Also, a fourth electron peak D is observed in the transients photoelectron spectra in Fig. 5.17a) and exhibits a transient with an decay time of $\tau_{decay(D)} = (830 \pm 60)fs$. This spectral feature was not reported in [181]. The signal of peak D is maximal at time zero, when the two pump- probe- pulses temporally overlap, but it's lifetime $\tau_{decay(D)} \neq \tau_{decay(A)}$ is different than peak A. This implies that peak D should originate either from an electronic state degenerate to S_1, presumably from the embeded Rydberg manifold, or from a component of the wavepacket generated on the S_1, which undergoes a decay different than the $S_1 \rightarrow Z$.
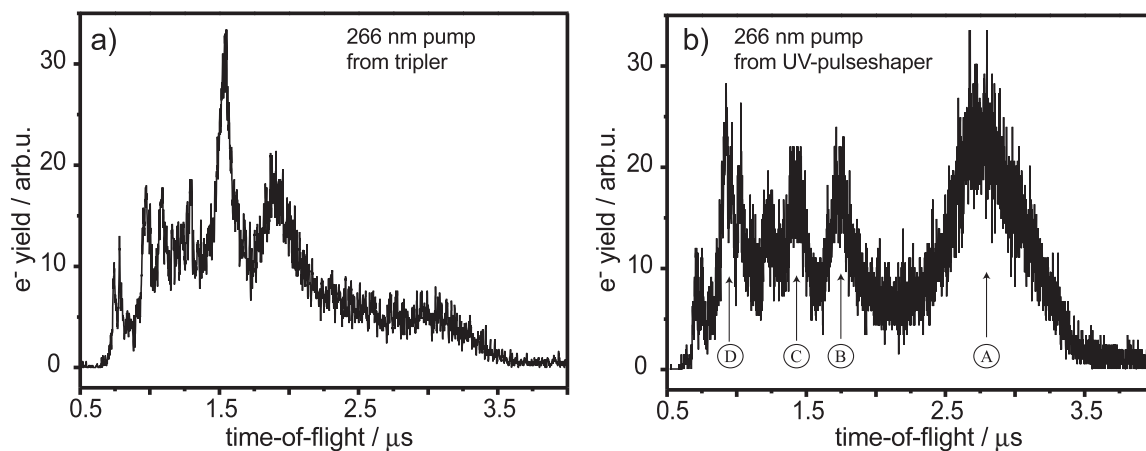
Figure 5.19: Photoelectron spectra of TDMAE resulting from a 266 nm pump- 800 nm probe excitation. In spectrum a) a pump pulse generated by frequency upconversion in the Tripler was used, while for spectrum b) the 266 nm pulses from the UV-pulseshaping setup, without modulating the spectral phase in the LCD, were employed.

5.8   Adaptive control of the $\pi\pi^{\star}$ excitation in TDMAE

One striking difference between the transient spectra presented above and those reported by Soep [181] is the remarkably low amplitude of the slowest photoelectron peak A. This deviation was previously addressed to differences in the exact parameters of the employed laser fields. In Fig. 5.19 the photoelectron spectra measured for a fixed 1,5 ps delay time are presented. Graph a) was acquired with the 266 nm pulses from the tripler (Section 3.2.2) while for b) the pulse-shaped 266nm field, described in Section 3.2.5, was employed. The shaped UV pulses in b) were relative broad (500 fs) although a constant zero spectral phase function was applied to the LCD. This is due to the uncompensated dispersion of the second harmonic field used for the frequency mixing. In Fig. 5.19b, peak A appears to be the dominant feature as in the measurements by Soep [181]. This contributes to the assumption that the amplitude of this peak is sensitive to the temporal characteristics of the 266 nm pump- pulse. Therefore, peak A was chosen as target for an optimization experiment.

The electron-signal registered in the time-of-flight window from 2,5 μs to 3,5 μs was integrated using the Boxcar-integrator and implemented as feedback for the evolutionary algorithm. In this experiment, the 266 nm pump-pulse shape was modulated, while the probe- 800 nm pulses were not altered. Also, the delay-time was constant at 1,5 ps. It has to be noted, that the pump-probe delay time is not affected by the phase applied to LCD. It is rather defined by the time distance between the probe 800 nm and the
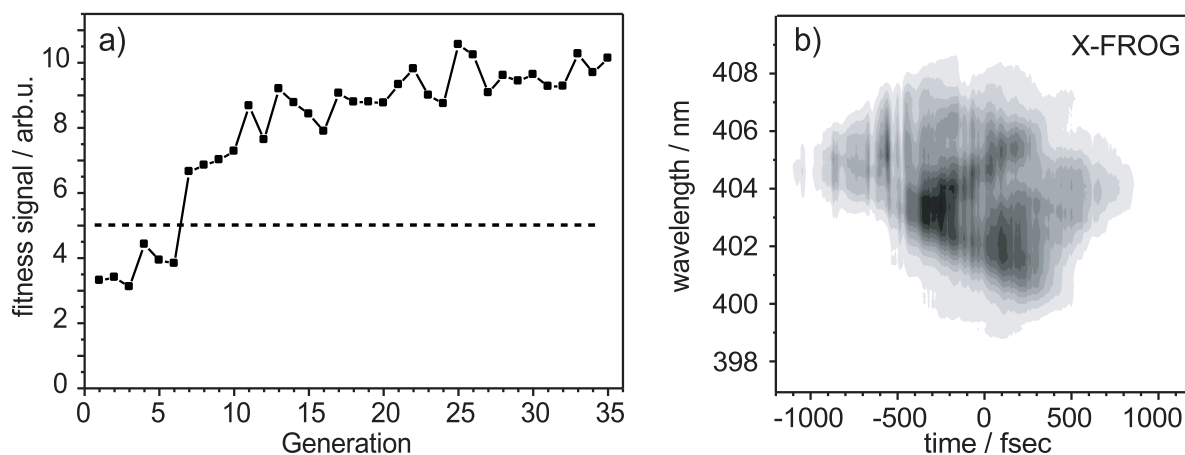
Figure 5.20: a)Optimization of the fitness signal as a function of the evolutionary algorithm iteration number. The dashed line indicates the signal corresponding to unmodulated pulses. b) X-FROG trace of the optimal 266 nm laser pulse found by the evolutionary algorithm. The X-FROG signal is measured by difference frequency mixing of the 266 nm pulse with a reference 800 nm pulse. The spectrum of the resulting downconverted 400 nm field is measured as a function of the delay between the 266 and 800 nm pulses.

broad 400 nm pulse, used for the 266 nm pulse-shaping. In Fig. 5.20, the fitness signal is plotted as a function of the algorithm iteration number. In the end of the optimization an increase of the fitness value by a factor 2 was achieved. Also, in Fig. 5.20b the X-FROG trace of the optimal 266 nm pulses is depicted, measured by difference frequency mixing of the 266 nm pulse with a reference 800 nm pulse. After the optimization, the energy of the 266 nm pulses was slightly lower (99%) than that of the unmodulated pulse. To ensure that the fitness signal increase is due to the optimized pump-pulses and not to an unlike variation of the pump-probe delay time, transients of the fitness signal were recorded with the optimal and the unmodulated pulse-shapes (Fig. 5.21). Evidently, the fitness signal at the (previously fixed) 1,5 ps delay time is double with the optimal pulse shape.

Both transients in Fig. 5.21 were fitted with an exponential decay function convoluted with the cross-correlation function of the pump-probe pulses. Interestingly, the exponential decay components of the two curves have completely different time constants, $\tau_{optimal} = (910 \pm 50)fs$ and $\tau_{unmodulated} = (530 \pm 70)fs$ for optimal and unmodulated pulse-shape, respectively. This pronounced difference signifies a switching between the coupling mechanisms that transfer population from the excited S_1 state towards different electronic configurations. Subsequently, the excitation with optimally shaped pump-pulses allows for the prolonged propagation of the generated wavepacket upon the S_1 potential surface.
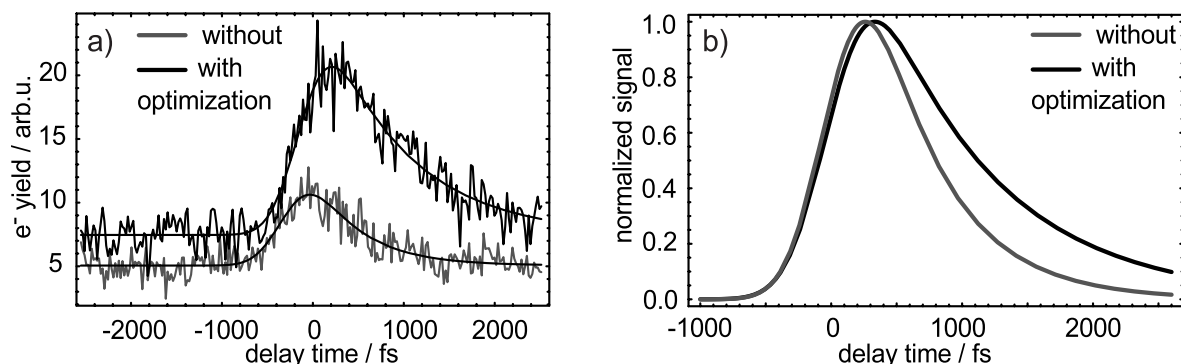
Figure 5.21: a)Transient measurements of the fitness signal as a function of the pump-probe delay time. It is evident that for the fixed delay time 1,5 ps the optimal pulse shape resulted in doubling of the fitness signal. b) The normalized transients exhibit different exponential decay time constants, $\tau_{optimal} = (910 \pm 50)fs$ and $\tau_{unmodulated} = (530 \pm 70)fs$ with and without optimization, respectively.

5.9   Conclusion

In this chapter the possibility of employing modulated 266 nm laser pulses to control the $\pi\pi^\star$ excitation of ethylene-like molecules was investigated. The internal conversion dynamics (isomerization) following the $\pi\pi^\star$ transition of C=C double bonds have attracted intense scientific interest in the field of femtochemistry because of its important role in biological processes. The spectroscopic method employed here was femtosecond photoelectron spectroscopy, an emerging powerful technique already applied to the study of excited dynamics of polyatomic molecules. First the molecule stilbene was studied, one of the most famous molecules in isomerization dynamics studies. The simplicity of its chemical structure, with two phenyl moeities on each side of a central ethylene bond, constitutes stilbene a rather attractive case also for theoretical calculations. Although no adaptive control experiment was possible on this molecule, a number of new spectroscopic data involving the second excited electronic state S_2 were acquired. Then, the molecule tetrakis(dimethylamino)ethylene (TDMAE) was investigated. TDMAE has a much more complex chemical structure than stilbene. Nevertheless, the previously reported studies on the dynamics of the molecule by B. Soep et.al. [181] served as a starting point for conducting a successful optimization experiment on the wavepacket propagation upon the $(\pi\pi^\star)$ S_1 excited potential surface.

6 Laser activation of a Metallocene Catalyst

6.1 Introduction

Since their discovery, synthetic materials play an increasingly important role in modern economy and daily life. Among others, the production of the polymer polyethylene (PE) constitutes a major activity of the modern chemical industry [188]. The polymerization reaction of ethylene was accidentally discovered in 1933 by Reginald Gibson and Eric Fawcett who carried out an experiment to react ethylene with benzaldehyde under extreme pressure and temperature conditions. A small amount of white, waxy solid was found in the reaction vessel, which Fawcett identified as a polymer of ethylene. The industrial exploitation of this discovery was, however, limited by the extreme temperature and pressure conditions necessary for the reaction, reflecting to a rather high production cost. A solution to this problem was proposed in 1953 by Karl Ziegler. He discovered that polymerization of ethylene is possible under moderate temperature and pressure conditions by employing the organometallic catalyst ($TiCl_4Cl,AlR_3$). Supported also by the work of the italian researcher Giulio Natta, they have established an entire class of the so-called Ziegler-Natta catalysts. Their findings triggered a succession of exciting discoveries in modern chemistry [189, 190] with an enormous impact on reducing the production cost of PE and other olefine polymers. The PE formed under high pressure and temperature conditions, the so-called *low density polyethylene* (LDPE), exhibits a complex structure, low density and a crystallization factor of 40–50%. Its characteristic feature is the numerous branches along the polymer chain (Fig. 6.1) that results in a remarkable flexibility and a low density of the polymer [189]. The catalytic Ziegler-Natta polymerization results rather in higher molecular weights, eventhough the lower temperature and pressure conditions employed. By use of this so-called *coordinative catalysis* method, in contrast to LDPE, the polymer chains formed are longer and more linear, with an enhanced crystallization factor of (60–80 %) and a higher density. This product
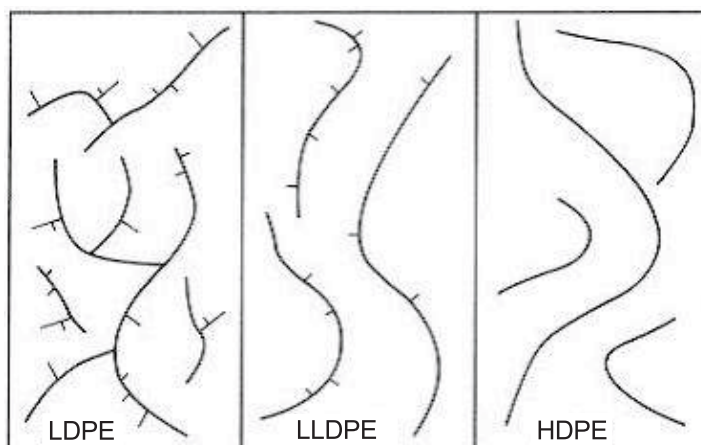
Figure 6.1: Classification of the polyethylenes based on the degree of branching of their polymer chain, resulting from the different production methods: low density polyethylene (LDPE), linear low density polyethylene (LLDPE), high density polyethylene (HDPE) [189].

is known as *high density polyethylene* (HDPE). Also, by copolymerization of ethylene with other olefins like buten it is possible to enhance the formation of side chains.

A substantial disadvantage of the first generation Ziegler catalysts ($TiCl_4Cl$, AlR_3) was that they exhibit not only one but many different active centers, upon which a polymerization reaction can be initiated. For instance, depending on the position on the $MgCl_2$ host matrix, Ti experiences a different chemical environment and by that a different catalytic action. As a result, a non uniform polymer is formed, consisting of many macromolecules of various molecular weight. This problem was resolved by introducing the so-called *metallocene* catalysts that exhibit only a single and rather well defined catalytic center (*single site* catalysts). The catalytic center of a metallocene is a metal atom from the 4th column of the periodic table (usually Zr or Ti), sandwiched between two aromatic cyclopentadienyl (Cp) rings. In certain cases, the two rings are bridged with each other. This structure results in an effective shielding of the catalytic center from its chemical environment and allows for a uniform catalytic activity and the formation of well defined polymer products. Both, the bridging of the aromatic rings as well as the nature of the ligands attached to the central metal atom have a strong influence on the catalytic ability of the metallocene. For instance, the choice of the specific ligand attached determines the formation of atactic, isotactic or syndiotactic polymers. Synthetic materials of great technical importance, like Polyamid, Polyester, Polycarbon and other polyolefins, are produced today by means of metallocene catalysts with improved mechanical and thermal properties.

Metallocene catalysts are customarily activated by use of special molecular complexes known as methylaluminoxan (MAO). The development of MAO was initiated in 1970 by Kaminsky and Sinn [191,192] and still constitutes a subject of intense research in modern chemistry [193,194]. MAO consists of successive Al and O atom chains. One of the major roles of MAO in the metallocene activation is the cleavage of a methyl group from the central metal atom by one of its free valence electrons. The greatest disadvantage of MAO activators is their high cost (their price is two orders of magnitude higher than Ziegler-Natta catalysts). The production of MAO is expensive and dangerous since it explodes following contact with air and reacts strongly with humidity. Up to now, these technical drawbacks have restricted the wide industrial application of metallocene catalysts. However, modern polymer research is oriented towards finding alternative methods for metallocene activation.

In this concept, we investigated the possibility of activating a metallocene catalyst by utilizing intense femtosecond laser radiation. This project was conducted in collaboration with the company BASF A.G. The original idea was to employ specially tailored laser pulses to cleave one of the methyl groups, attached to the central metal atom of the metallocene and to activate the catalyst. Similar control schemes have been previously demonstrated by our group in photodissociation reactions of organometallic [19, 20] as well as polyhalogenated molecules [195]. The model catalyst used for the present investigation was bis-(cyclopentadienyl)-zircon-dimethyl, $(Cp)_2Zr(CH_3)_2$ the structure and catalytic action of which is summarized in Fig. 6.2. A plausible description of polyolefine chain buildup was first proposed in 1960 by Cossee and is still accepted as the most probable scenario [196, 197]. Following the cleavage of one methyl group (Fig. 6.2 step 1→2) the activated cation has 14 valence electrons and a coordination position, upon which the olefin monomer (in this case ethylene) is bound via its π−electrons (step 3). In the created four-center geometry (Fig. 6.2, step 4) the remaining methyl group loses its σ bonding with the Zr center and crosses to the β-position of ethylene (step 5). In this way a monoalkylzircon cation is created, which realized a further insertion reaction with ethylene, eventually leading to the formation of a long polymere chain. In this mechanism, the free cooredination position moves from one side to the other of the metallocene center [193,194]. The termination of the polymer buildup finally is realized by protonation and thermal splitting of the active center [197].
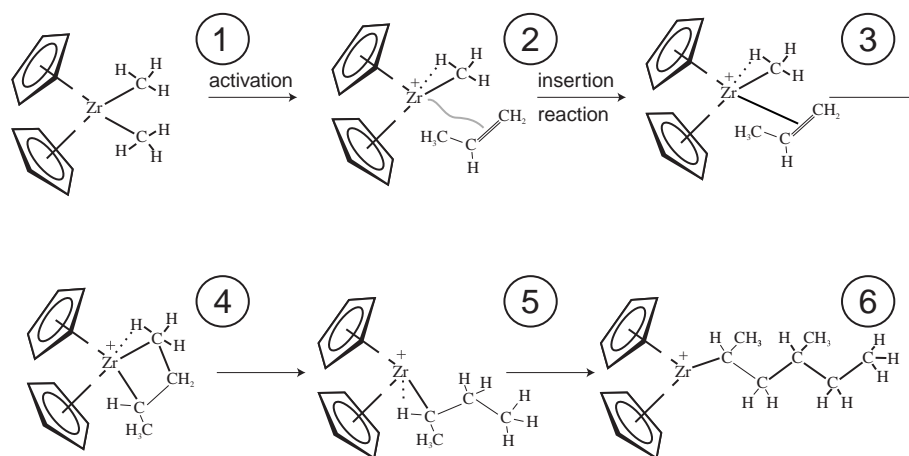
Figure 6.2: Activation and catalytic action of the metallocene bis-(cyclopentadienyl)-zircon-dimethyl ($(Cp)_2Zr(CH_3)_2$). 1) In the precursor of the investigated metallocene catalyst two methyl groups are attached as ligands to the central Zr metal atom. 2) By selective cleavage of one methyl group the catalyst is activated and a successive formation of a polyethylene chain 3-6 is initiated.

6.2 Intensity dependence of metallocene photofragmentation

To study the photofragmentation of the metallocene $(Cp)_2Zr(CH_3)_2$ a molecular sample was commercially purchased by Sigma-Aldrich with a purity of $> 98\%$, and without further purification the molecule was brought into the gas phase by means of the effusive beam method (Section 3.4). The 800 nm laser pulses from the Ti:Sapphire laser system were employed for the excitation. They were focused by means of a 300 mm quartz lens and the laser field intensity was regulated by inserting reflective neutral density filters into the laser beam path. The generated photofragments were detected with the reflectron mass spectrometer and recorded by the TDA card.

In Fig. 6.3a, the mass-spectrum resulting from the excitation with 116 μJ laser pulses is depicted. Three groups of photofragments are observed in the regions: 251–257 amu, 231–238 amu, and 216–222 amu. The fragments resulting from cleavage of one- and two- methyl groups are assigned to the peaks at 236 *amu* and 221 *amu*, respectively. Accordingly, the ionized $(Cp)_2Zr(CH_3)_2$ parent molecule (no fragmentation) corresponds to the peak at 251 amu. In the spectral areas of all three masses a similar 7 side-peak pattern is visible, as depicted in Fig. 6.3b. This structure can be explained on the basis of the naturally occurring isotopes of Zr, the relative weight (reference values) of which
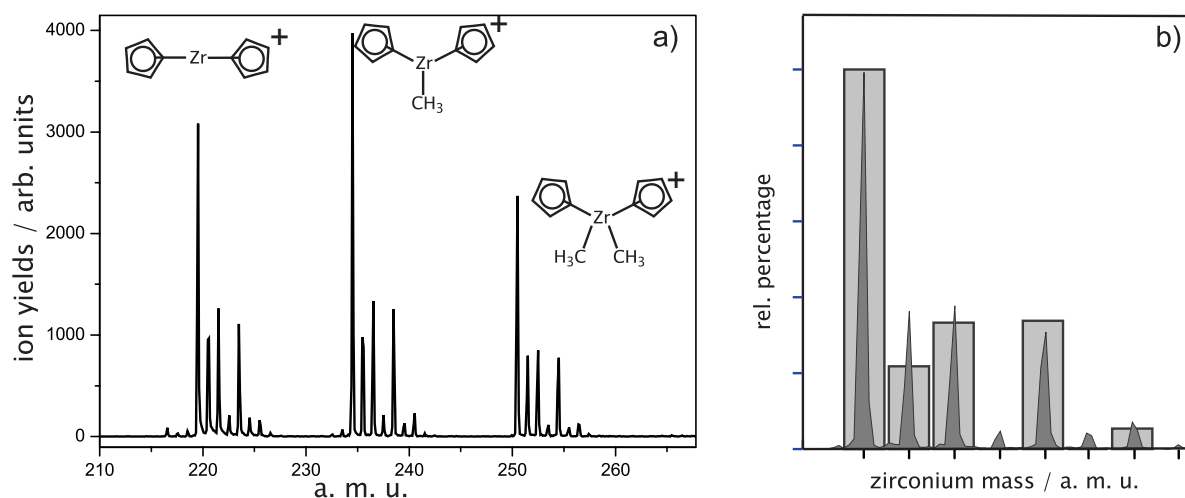
Figure 6.3: a) Mass spectrum of the metallocene Bis-(Cyclopentadienyl)-Zircon-Dimethyl $((Cp)_2Zr(CH_3)_2)$. The three groups of peaks observed correspond to the ionization of the molecule as well as to the two main fragments following the loss of one and two methyl groups. b) The side peak structure within each group is mainly due to the natural isotopes of Zr, the relative weight (literature values) is presented with a shaded bar diagram

is shown with shaded bars in Fig. 6.3b). For higher laser intensities the metallocene is subject to severe fragmentation and lighter masses were also observed in the spectrum.

The main goal of this project was to enhance the production of the $(Cp)_2Zr(CH_3)$ fragment in expense of the lighter $(Cp)_2Zr$ fragment. The corresponding ion yields were recorder as a function of the laser pulse energy employed for the excitation. The two signals exhibit practically an identical intensity dependence (Fig. 6.4a), while the ratio of the two remains practically constant within a 10 % range. Due to the saturation of the transition, the slope of both photofragmentation signals in Fig. 6.4a reduces for higher laser pulse energies.

6.3 Pump-probe transients of metallocene photofragmentation

In the next experiment, the photofragmentation of the metallocene was investigated utilizing a pump-probe scheme, where two identical 800 nm femtosecond pulses were employed for the excitation. The ion yields of to the $(Cp)_2Zr(CH_3)$ and $(Cp)_2Zr$ fragments were recorded as a function of the pump-probe delay time. A time-window of $\pm 600~fs$ was scanned in time intervals of 20 fs. The results of the above measurements are summarized in Fig. 6.5. The central peak of the transients corresponds to the time
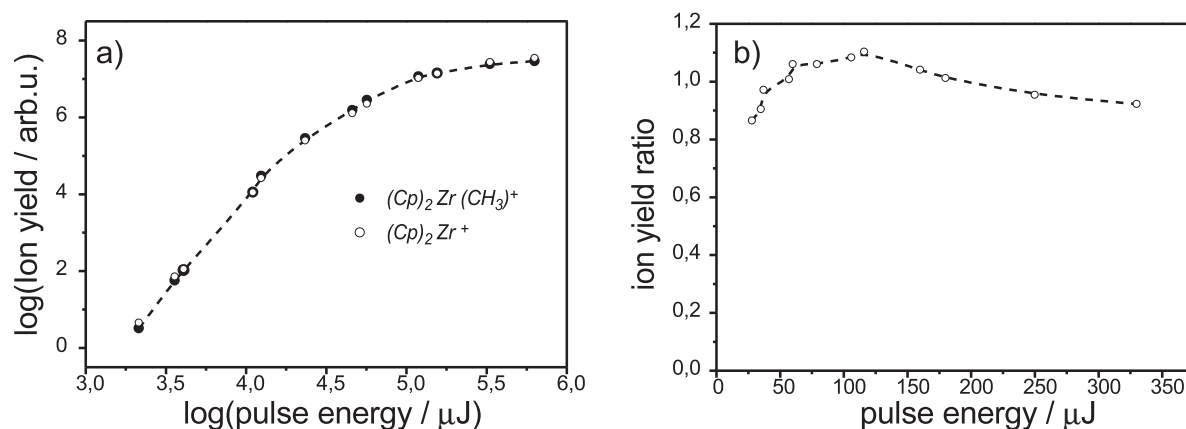
Figure 6.4: Intensity dependence of the photofragmentation. a) The ionization signals of the $(Cp)_2Zr(CH_3)_+$ (filled circles) and $(Cp)_2Zr)_+$ (open circles) fragment is plotted as function of the pulse energy of the excitation laser field. b) The ratio of the above ionization signals is plotted as function of the laser pulse energy.

when the two laser pulses perfectly overlap. Apart from a small side peak structure no particular dynamical processes are implied by the transient signals. The two photofragmentation signals exhibit practically the same behaviour, with their ratio fluctuating within a range of 15 %.

6.4 Adaptive control of catalyst activation

In the previous sections two simple mechanisms for controlling the photofragmentation of the metallocene $(Cp)_2Zr(CH_3)_2$ were addressed. By varying the intensity of a single excitation pulse, or by using a pair of two identical laser pulses and appropriately delaying one with respect to the other, no sufficient control was achieved with respect to selectively cleaving one CH_3 group of the metallocene catalyst without effecting the second methyl group. As a next step, the technique of adaptive femtosecond pulse shaping was applied. In this optimization experiment, the goal was to enhance the ratio of the generated $(Cp)_2Zr(CH_3)^+$ versus the $(Cp)_2Zr^+$ photofragment. Among the different isotopes of Zr the molecular fragments including the 90 amu isotope were selected for the optimization. Maximization of the $(Cp)_2Zr(CH_3)^+$ /$(Cp)_2Zr)^+$ ratio with shaped 800 nm pulses was achieved within 60 generations of the evolutionary algorithm, to yield the product distribution shown in Fig. 6.6b. The mass spectrum acquired with unmodulated pulses is shown in Fig. 6.6a. The selectivity over the two photodissosiation channels is now evident. By optimizing the spectral phase of the femtosecond pulses the $(Cp)_2Zr(CH_3)^+$ /$(Cp)_2Zr^+$ ratio was increased from around 1,15 to 1,95. The
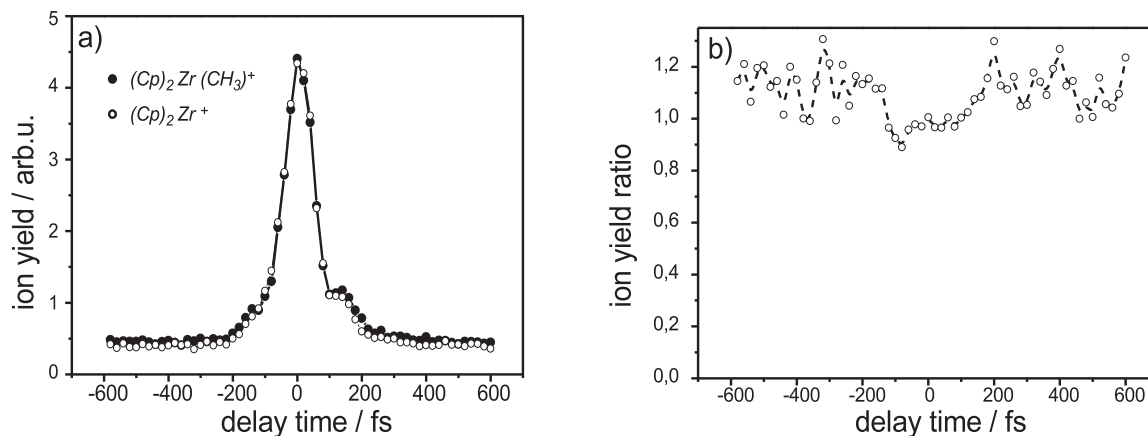
Figure 6.5: Pump-probe measurements a) Normalized transients of the ionization signals of the $(Cp)_2Zr(CH_3)^+$ (open circles) and $(Cp)_2Zr^+$ (filled circles) fragment. b) The ratio of the above ionization signals is plotted as a function of the delay time between the pump- and probe- pulses.
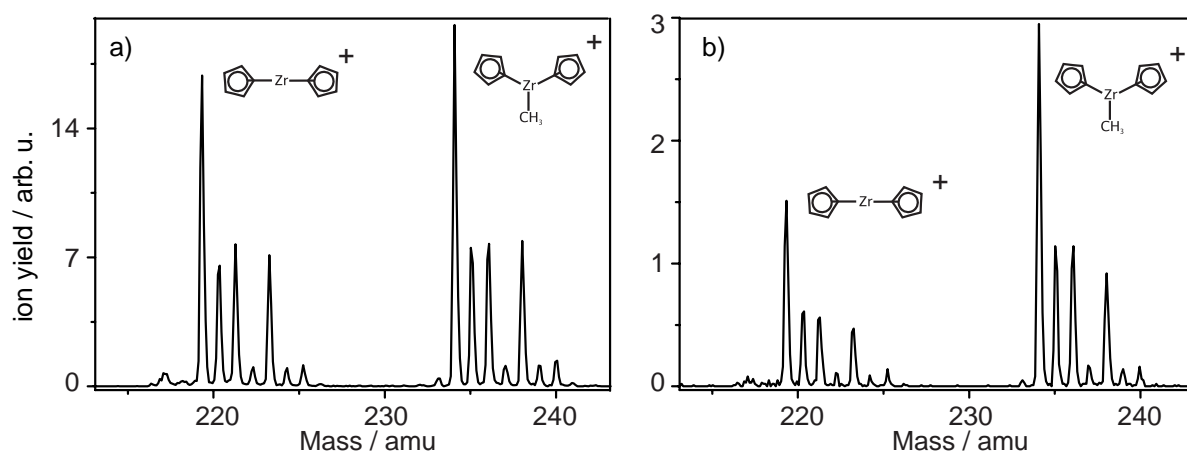
Figure 6.6: Comparison of the photoproduct yield for excitation a) with an unodulated laser pulse and b) with the optimized laser pulse. An optimal ratio $(Cp)_2Zr(CH_3)^+/(Cp)_2Zr^+$ of over 1,95 is achieved in expense of the total $(Cp)^2Zr(CH_3)^+$ ion yield, which has decreased by almost a factor 5.
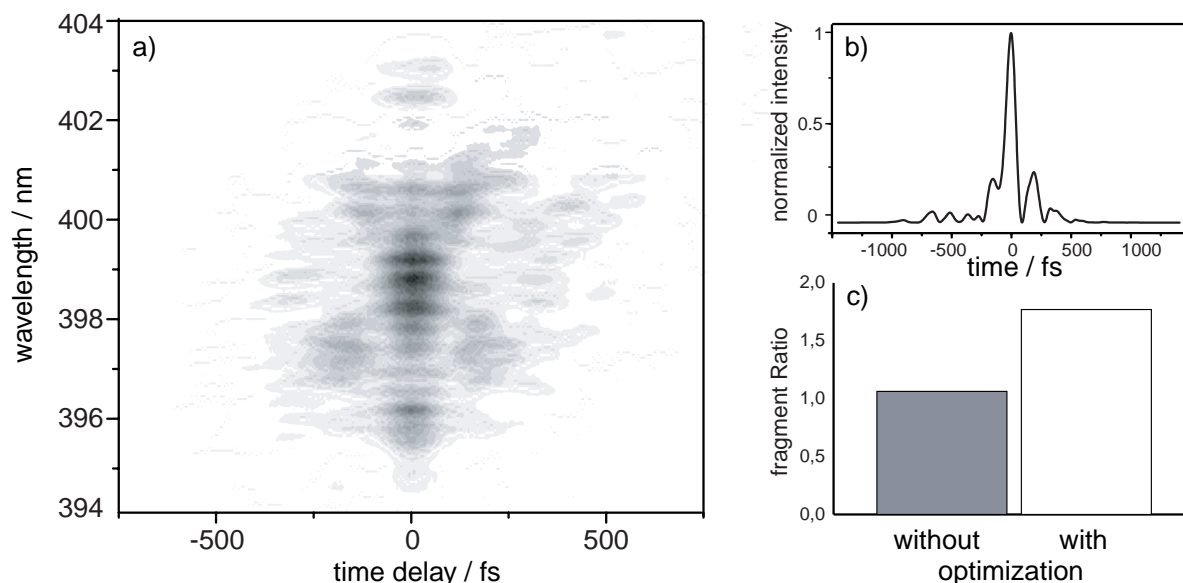
Figure 6.7: Summary of the $(Cp)_2Zr(CH_3)^+/(Cp)_2Zr^+$ ratio optimization. a) The FROG trace of the optimal laser pulse, b) The intensity profile of the optimal laser pulse after analyzing the measured FROG trace, c) Bar diagram of the measured photoproduct ratio following excitation with an unmodulated laser pulse (shaded block) and a pulse with optimized spectral phase (empty block).

optimal laser pulse (Fig. 6.7a) and b)) is a rather long laser pulse with several components distributed over a time window of almost 500 fs. This spreading of the pulse energy resulted in a substantial decrease of the maximum laser field intensity. Due to the high nonlinearity of the intensity dependence of the ionization signal (Fig. 6.4a)), this translated to the decrease of the total ion yield.

6.5   Conclusion

In this chapter, the possibility of employing femtosecond laser pulses as an alternative method for activating a metallocene molecular catalyst was investigated. Experiments were performed on the model catalyst $(Cp)_2Zr(CH_3)_2$, where the selective cleavage of one methyl-ligand attached to the central Zr atom induced a catalytic coordination position on the molecule. In this context, the generation of the $(Cp)_2Zr(CH_3)^+$ and $(Cp)_2Zr^+$ photofragments were monitored as a function of various parameters of the excitation laser field. Selective cleavage of only one of the two methyl ligands constitutes a nontrivial control problem since both ligands are completely symmetric with respect to the active Zr center. This purpose was rather served by means of an adaptive optimization scheme where the spectral phase of an 800 nm femtosecond laser pulse was

optimized. By means of an evolutionary optimization strategy a substantial increase of the $(Cp)_2Zr(CH_3)^+/(Cp)_2Zr^+$ photofragment ratio was achieved. This proof-of-principle experiment demonstrates the applicability of femtosecond laser pulses as a novel tool for catalyst activation. Similar activation schemes realized inside a dense olefine environment (condensed phase experiments) could potentially provide a commercial application of this technique.

7 Summary

The subject of this work has been the investigation of dynamical processes that occur during and after the interaction of matter with pulses of femtosecond laser radiation. The experiments presented here were performed in the gas phase and involve one atomic and several model molecular systems. Absorption of femtosecond laser radiation by these systems induces an electronic excitation, and subsequently their ionization, photofragmentation or isomerization. The specific adjustment of the excitation laser field properties offers the possibility to manipulate the induced electronic excitation and to influence the formation of the associated photoproducts.

From the perspective of the employed spectroscopic methods, the development of photoelectron spectroscopy and its implementation in laser control experiments has been of particular interest in this thesis. This technique allows for a most direct and intuitive observation of electronic excitation dynamics in atomic as well as in complex polyatomic molecular systems. The propagation of an intermediate electronic transient state, associated to the formation of a particular photoproduct, can be interrogated by means of its correlation to a specific state of the atomic or molecular continuum. Such correlations involve the autoionization of the transient state, or by means of a second probe laser field, a structural correlation, as summarized by the Koopman's theorem (section 2.4.1).

The technique of adaptive femtosecond quantum control has been the subject of development in our group for many years. The basic method, by which the temporal profile of near-infrared laser pulses at a central wavelength of 800 nm, can be adjusted, is a programmable femtosecond pulse-shaper that comprises of a zero dispersion compressor and a commercial liquid crystal modulator (LCD). This experimental arrangement was realized prior to this thesis and served as a starting point to extend the pulse-shaping technique to the ultraviolet spectral region. This technological development was realized for the purposes of the experiments presented in Chapter 5. It involves a combination of the LCD-pulse-shaper with frequency up-conversion techniques on the basis of producing specifically modulated laser pulses of central wavelength 266 nm. Furthermore,

the optical method X-FROG had to be developed in order to characterize the often complex structure of generated ultraviolet pulses. In the adaptive control experiments presented in this work, the generated femtosecond laser pulses could be automatically adjusted by means of specifically addressing the 128 independent voltage parameters of the programmable liquid-crystal modulator. Additionally a machine learning algorithm was employed for the cause of defining laser pulse-shapes that delivered the desired (optimal) outcome in the investigated laser interaction processes.

In Chapter 4, the technique of feedback-controlled femtosecond pulse shaping was combined with time-of-flight mass spectroscopy as well as photoelectron spectroscopy in order to investigate the multiphoton double ionization of atomic calcium. A pronounced absolute enhancement of the double ionization yield was obtained with optimized femtosecond laser pulses. On the basis of the measured photoelectron spectra and of the electron optimization experiments, a non-sequential process was found, which plays an important role in the formation of doubly charged Calcium ions.

Then in Chapter 5, the dynamics following the $\pi\pi^{\star}$ excitation of ethylene-like molecules were investigated. In this context, the model molecule stilbene was studied by means of femtosecond photoelectron spectroscopy. Due to the simplicity of its chemical structure, stilebene is one of the most famous models used in experimental as well as theoretical studies of isomerization dynamics. From the time-resolved experiments described in that chapter, new spectroscopic data involving the second excited electronic state S_2 of the molecule were acquired. The second ethylenic product was the molecule tetrakis (dimethylamino) ethylene (TDMAE). Due to the presence of numerous lone pair electrons on the four dimethylamino groups, TDMAE exhibits a much more complex structure than stilbene. Nevertheless, previously reported studies on the dynamics of TDMAE provided vital information for planning and conducting a successful optimization control experiment of the wavepacket propagation upon the $(\pi\pi^{\star})$ S_1 excited potential surface of the molecule.

Finally, in Chapter 6 the possibility of employing femtosecond laser pulses as an alternative method for activating a metallocene molecular catalyst was addressed. By means of an adaptive laser control scheme, an optimization experiment was realized. There, the target was the selective cleavage of one methyl-ligand of the model catalyst $(Cp)_2Zr(CH_3)_2$, which induces a catalytic coordination position on the molecule. The spectroscopic studies presented in that chapter were performed in collaboration to the company BASF A.G. and constitute a proof-of principle attempt for a commercial application of the adaptive femtosecond quantum control technique.

Zusammenfassung

Das Thema der hier vorgestellten Arbeit umfasst die Untersuchung von dynamischen Prozessen, die während der Wechselwirkung von Femtosekunden Laserpulsen mit Atomen und Molekülen stattfinden. Die entsprechenden Experimente sind in der Gasphase durchgeführt worden, wobei ein Atom- und mehrere Molekül-Modellsysteme untergesucht wurden. Die Absorption von Femtosekunden-Laserstrahlung induziert die elektronische Anregung der quantumsmechanischen Systeme und eventuell deren Ionisation, Photofragmentnation oder Isomerisierung. Die gezielte Einstellung der Laserfeldeigenschaften bietet die Möglichkeit, diese Prozesse zu beeinflussen, beziehungsweise die Formung von entsprechenden Photoprodukten zu steuern.

Im Hinblick auf die verwendeten spektroskopischen Methoden wurde besonderes Interesse auf die Entwicklung von Photoelektronen-Spektroskopie und in deren Einsatz zur Durchführung von laserinduzierten Kontrollexperimente gelegt. Photoelektronen-Spektroskopie ermöglicht die direkte und intuitive Beobachtung elektronischer Anregungsdynamik in Atomen sowie in komplexen mehreratomaren Molekülsystemen. Die zeitliche Entwicklung von angeregten elektronischen Zuständen ist oft bei der Formung von bestimmten Photoprodukten assoziiert. Die Dynamik kann mittels der Korrelation des sich entwickelnden Zustandes zu den Kontinuumzuständen des Atom- oder Molekül-Systems untersucht werden. Das Detektionsverfahren umfasst die Autoionization oder, mittels eines zweiten Laserpulses, die Weiteranregung des Systems ins Kontinuum. Denn, die Beobachtung der entsprechenden Strukturänderungen des Systems erfolgt mittels der Korrelation des zwischenangeregten Zustand zu den verschiedenen Kontinuumzuständen (Koopman Theorem).

Seit mehreren Jahren wurde die Methode der adaptiven Femtosekunden-Pulsformung in unserer Gruppe entwickelt. Die anfängliche experimentelle Anordnung besteht aus einer Kombination von einem Flüssig-Kristall-Modulator (LCD) und einen Null-Dispersions-Kompressor. Damit ist es möglich, das zeitliche Profil von Laserpulsen im Infrarot (800 nm) Spektralbereich automatisch zu modulieren. Diese Entwicklungsarbeit stand bereits

zu Verfügung vor dem Anfang der vorgestellten Dissertation. Hier wurde die Erweiterung dieser Methode in den ultravioletten Spektralbereich vorgestellt (Kapitel 5). Es umfasst eine Kombination von dem bestehenden LCD-Pulsformer und einem Verfahren zur Frequenzkonversion, das die Erzeugung von modulierten Laserpulsen mit eine Wellenlänge 266 nm ermöglicht. Die entsprechende Charakterisierungsmethoden (X-FROG) wurden ebenfalls entwickelt. Die Femtosekunden-Laserpulse können automatisch moduliert werden durch die entsprechende Einstellung der 128 unabhängigen Spannungsparametern des LCD-Modulators. Zusätzlich wurden die optimale Parameter für die Kontrolle eines bestimmten Anregungsprozess mittels eines Machine-Learning Algorithmus gefunden.

In Kapitel 4 wurde die Mehrphoton-Doppleionization von Calciumatomen untersucht. Dabei wurde die Methode der adaptiven Pulsformung zusammen mit time-of-flight Massenspektroskopie und Photoelektronenspektroskopie eingesetzt. Das absolute Signal der Doppleionization konnte verdoppelt werden durch die Anregung mit bestimmten komplexen Pulsformen. Gerade bei den Optimierungexperimenten an Photoelektronenspektra konnte ein "non-sequential" Prozess entdeckt werden, der eine wichtige Rolle bei der Doppleionization von Calcium spielt.

In Kapitel 5 wurde die Dynamik von $\pi\pi^\star$ Anregungsprozessen von Ethylenähnlichen-Moleküle untersucht. Im diesen Zusammenhang wurde das Modelmolekül Stilbene mittels Photoelektronenspektroskopie weiteruntersucht. Wegen seiner einfachen Struktur ist Stilbene eines der meistbenutzten Moleküle für Untersuchungen zur Photoisomerisierungsdynamik. Gerade bei den hier dargestellten zeitaufgelösten Messungen wurde neu spektroskopische Information über den zweiten angeregten elektronische Zustand S_2 entdeckt. Das zweite untersuchte Molekül ist Tetrakis (Dimethylamino) Ethylen (TDMAE). Wegen den zahlreichen "Lone-Pair" Elektronen an seinen Dimethylamino Gruppen ist die gesamte Struktur des Moleküls deutlich komplexer im Vergleich zu Stilbene. Allerdings, ausgehend von gegebenen spektroskopischen Informationen aus der Literatur konnte ein erfolgreiches Kontrollexperiment an der Wellenpackets-Propagation des $\pi\pi^\star$ Anregungsprozesses (auf dem S_1 Zustand) geplant und durchgeführt werden.

In Kapitel 6 wurde schlielich die Möglichkeit erforscht, einen Metallocene-Katalysator mittels Femtosekunden-Laserpulsen zu aktivieren. Das Kotrollschema der adaptiven Pulsformung wurde dabei eingesetzt, um eine der zwei identischen Methylgruppen des Moleküls selektiv abzuspalten, was zur Aktivierung des Katalysators führt. Diese spektroskopische Untersuchung wurde in Kollaboration mit der Firma BASF A.G. durchgeführt. Es stellt einen Grundlagenversuch der industriellen Anwendung der adaptiven Quantumskontrollemethode dar.

Bibliography

[1] G. Porter
Flash photolysis and spectroscopy, an new method for the study of free radical reactions,
Proc. R. Soc. London A **200**, 284 (1950).

[2] C. V. Shank
Investigation of ultrafast phenomena in the femtosecond time domain,
Science **233**, 1276–1280 (1986).

[3] D. E. Spence ,J. M. Evans , W. E. Sleat, W. Sibbett,
Regeneratively initiated self-mode-locked Ti-Sapphire Laser,
Opt. Lett. **16**, 1762–1764 (1991).

[4] S. L. Shapiro,
Ultrashort Light Pulses,
Verlag, Berlin, Heidelberg, New York (1977).

[5] J. Herrmann and B. Wilhelmi,
Lasers for Ultrashort Light Pulses,
Akademie-Verlag, Berlin, (1987).

[6] T. Baumert, R. Thalweiser, G. Gerber,
Femtosecond 2-Photon ionization spectroscopy of the B-State of Na_3 Clusters,
Chem. Phys. Lett. **209**, 29–34 (1993).

[7] A. H. Zewail
*Femtochemistry: ultrafast dynamics of the chemical bond I & II, vol 3 of World Scientific
    series in the 20th century chemistry,*
World Scientific Publishing Co. Pte. Ltd., Singapore (1994).

[8] A. H. Zewail
Femtochemistry: Atomic-Scale Dynamics of the Chemical Bond,
J. Phys. Chem. A **104**, 5660–5694 (2000).

[9] H. E. Edgerton ,E. Jussim, G. Kayafas,
Stopping Time: The Photographs of Harold Edgerton,
H.N. Abrams, New York (1987).

[10] T. Baumert, M. Grosser, R. Thalweiser, and G. Gerber
Femtosecond time-resolved molecular multiphoton ionization: The Na_2 system,
Phys. Rev. Lett **67**, 3753-3756 (1991).

[11] N.Bloembergen and A.H.Zewail
*Energy redistribution in isolated molecules and the question of mode-selective laser chem-
    istry revisited. New experiments on the dynamics of collisionless energy redistribution
    in molecules possibilities for laser-selective chemistry with subpicosecond pulses,*
J. Phys. Chem. **88**, 5459–5465 (1984).

[12] A. M. Weiner, D. E. Leaird, J. S. Patel, and J. R. Wullert
      Programmable shaping of femtosecond optical pulses by use of 128-element liquid-crystal phase modulator,
      IEEE J. Quant. Elect. **28**, 908–920 (1992).

[13] T. Brixner and G. Gerber,
      Femtosecond polarization pulse shaping,
      Optics Letters **26**, 557 (2001).

[14] A. P. Peirce, M. Dahleh, and H. Rabitz
      Optimal control of quantum-mechanical systems: Existence, numerical approximation, and applications,
      Phys. Rev. A **12**, 4950–4964 (1988).

[15] D. Yelin, D. Meshulach, Y. Silberberg
      Adaptive femtosecond pulse compression,
      Opt. Lett. **22**, 1793–1795 (1997).

[16] C. J. Bardeen, V. V. Yakovlev, K. R. Wilson, S. D. Carpenter, P. M. Weber, W. S. Warren,
      Feedback quantum control of molecular electronic population transfer,
      Chem. Phys. Lett. **280**, 151–158 (1997).

[17] T. Brixner, G. Gerber,
      Quantum control of gas-phase and liquid-phase femtochemistry,
      Chem Phys. Chem. **4** 418–438 (2003).

[18] T. Brixner, T. Pfeifer, G. Gerber, M. Wollenhaupt and T. Baumert,
      Quantum control of atomic and electron dynamics with tailored femtosecond laser pulses,
      In P. Hannaford (Ed.), *Volume on Femtosecond Laser Spectroscopy of Kluwer Series on Progress in Lasers*, Chapter 9, 418–438, Kluwer Academic Publishers, Dordrecht (2004).

[19] A. Assion, T. Baumert, M. Bergt, T. Brixner, B. Kiefer, V. Seyfried, M. Strehle and G. Gerber,
      Control of chemical reactions by feedback-optimized phase-shaped femtosecond laser pulses,
      Science **282**, 919–922 (1998).

[20] M. Bergt, T. Brixner, B. Kiefer, M. Strehle, and G. Gerber,
      Controlling the femtochemistry of $Fe(CO)_5$,
      J. Phys. Chem. A **103**, 10381-10387 (1999).

[21] R. Bartels, S. Backus, E. Zeek, L. Misoguti, G. Vdovin, I.P. Christov, M.M. Murnane, H.C. Kapteyn,
      Shaped-pulse optimization of coherent emission of high-harmonic soft X-rays ,
      Nature **406**, 164–166 (2000).

[22] T. Pfeifer, D. Walter, C. Winterfeldt, C. Spielmann and G. Gerber,
      Adaptive engineering of coherent soft x-rays,
      In *Ultrafast Phenomena XIV, Springer Series in Chemical Physics*, Springer, Berlin (2004).

[23] D. Oron, N. Dudovich, D. Yelin, Y. Silberberg,
      Narrow-band coherent anti-stokes Raman signals from broad-band pulses,
      Phys. Rev. Lett (**88**), 063004 (2002).

[24] T.C. Weinacht, P.H. Bucksbaum,
Using feedback for coherent control of quantum systems,
J. Opt. B **4**, R35–R52 (2002).

[25] E. Hertz, G. Nersisyan, N. A. Papadogiannis and D. Charalambidis,
Control of vibrational ionization branching through feedback-optimized tailored femtosec-
    ond laser pulses,
J. Chem. Phys. **118**, 595–599 (2003).

[26] H. Rabitz and W. Zhu,
Optimal control of molecular motion: Design, implementation, and inversion,
Acc. Chem. Res. **33**, 572–578 (2000).

[27] J. Paye,
The chronocyclic representation of ultrashort light pulses,
IEEE J. Quantum Electron. **28**, 2262–2273 (1992).

[28] J. Paye and A. Mignus,
Space-time Wigner functions and their application to the analysis of a pulse shaper,
J. Opt. Soc. Am. B **12**, 1480–1490 (1995).

[29] H. O. Bartelt, K. H. Brenner and A. W. Lohmann,
The Wigner distribution function and its optical production,
Opt. Commun. **32**, 32–38 (1980).

[30] K. H. Brenner and K. Wódkiewicz
The time-dependent physical spectrum of light and the Wigner distribution function,
Opt. Commun. **43**, 103–106 (1982).

[31] E. Wigner
On the quantum correction for thermodynamic equilibrium,
Phys. Rev. **40**, 749–759 (1932).

[32] M. Göppert-Mayer
Elementary processes with two quantum jumps,
Ann. Physik **9**, 273–94 (1931).

[33] F. H. M. Faisal,
Theory of Multiphoton Processes,
Plenum Press, New York (1987).

[34] P. Mulsed, S. Uryupin, R. Sauerbrey, B. Wellegehausen,
Ponderomotive potential and dynamical Stark shift in multiphoton ionization,
Phys. Rev. A **48**, 4547–4550 (1993).

[35] K. Burnett, V. C. Reed and P. L. Knight,
Atoms in ultra-intense laser fields,
J. Phys. B: At. Mol. Opt. Phys. **26** 561–598 (1993).

[36] P. Avan, C. Cohentannoudji, J. Dupontroc, C. Fabre,
Effect of high-frequency irradiation on dynamical properties of weakly bound electrons,
J. Phys. **37** 993–1009 (1976).

[37] M. D. Perry, A. Szoke, and K. C. Kulander,
Resonantly enhanced above-threshold ionization of helium,
Phys. Rev. Lett. **63**, 1058-1061 (1989).

[38] H. Helm, N. Bjerre, M. J. Dyer, D. L. Huestis, and M. Saeed,
     Images of photoelectrons formed in intense laser fields,
     Phys. Rev. Lett. **70**, 3221-3224 (1993).

[39] R. R. Freeman, P. H. Bucksbaum, H. Milchberg, S. Darack, D. Schumacher, and M. E.
     Geusic,
     Above-threshold ionization with subpicosecond laser pulses,
     Phys. Rev. Lett. **59**, 1092-1095 (1987).

[40] M. P. de Boer, H. G. Mueller,
     A systematic study of AC Stark shifts in xenon at super-high laser intensities,
     J. Phys. B **27**, 721–732 (1992).

[41] G. N. Gibson, R. R. Freeman, T. J. McIlrath,
     *Verification of the dominant role of resonant enhancement in short-pulse multiphoton
     ionization,*
     Phys. Rev. Lett. **69**, 1904-1907 (1992).

[42] P. Agostini, F. Fabre, G. Mainfray, G. Petite, N. K. Rahman,
     Free-Free Transitions Following Six-Photon Ionization of Xenon Atoms,
     Phys. Rev. Lett. **42**, 1127-1130 (1979).

[43] L. V. Keldysh
     Ionization in the field of a strong electronmagnetic wave,
     Sov. Phys. JETP **6**4, 1191–1194 (1965).

[44] E. Mevel, P. Breger, R. Trainham, G. Petite, P. Agostini, A. D. Migus, J. P. Chambaret,
     A. Antonetti
     Atoms in Strong Optical Fields: Evolution from Multiphoton to Tunnel Ionization,
     Phys. Rev. Lett. **70**, 406–409 (1993).

[45] L. F. DiMauro and P. Agostini,
     Advances in Atomic, Molecular and Optical Physics 35, p.79,
     B. Bederson and H. Walther, Academic Press, San Diego (1995).

[46] P. Lambropoulos,
     Mechanisms for Multiple Ionization of Atoms by Strong Pulsed Lasers,
     Phys. Rev. Lett. **55**, 2141-2144 (1985).

[47] K. Boyer, C.K. Rhodes,
     Atomic Inner-Shell Excitation Induced by Coherent Motion of Outer-Shell Electrons,
     Phys. Rev. Lett. **54**, 1490–1493 (1985).

[48] M. Born and J.R. Oppenheimer,
     Zur Quantentheorie der Molekeln,
     Ann. Phys. (Leipzig) **8**4, 457–484 (1927).

[49] R. Englman, J. Jortner,
     Energy gap law for radiationless transitions in large molecules,
     Mol. Phys. **18**, 145–164 (1970).

[50] M. Bixon, J. Jortner,
     Electron transfer via bridges,
     J. Chem. Phys. **107**, 1470–1482 (1997).

[51] H. Nagae, M. Kuki, J. Zhang, T. Sashima, Y. Mukai, Y. Koyama,

Vibronic coupling through the in-phase, C=C stretching mode plays a major role in the 2A(g)(-) to 1A(g)(-) internal conversion of all-trans-beta-carotene,
J. Phys. Chem. A , **1**04, 4155–4166 (2000).

[52] H. A. Jahn and E. Teller,
Proc. Roy. Soc. Lond. Ser. A. **1**61, 220–235, (1937).

[53] F. Bernardi, M. Olivucci, M. A. Robb,
Potential energy surface crossings in organic photochemistry,
Chem. Soc. Rev. 321–328 (1996).

[54] M. Klessinger,
Conical intersections and the mechanism of singlet photoreactions,
Angew. Chem. Int. Ed. **3**4, 549–551 (1995).

[55] W. Lichten,
Molecular wave functions and inelastic atomic collisions,
Phys. Rev. **1**64, 131–142 (1967).

[56] F. T. Smith,
Diabatic and adiabatic representations for atomic collision problems,
Phys. Rev. **1**79, 111–123 (1969).

[57] B. Balzer, S. Hahn and G. Stock,
Mechanism of a photochemical funnel: A dissipative wave-packet dynamics study,
Chem. Phys. Lett. **3**79, 351–358 (2003).

[58] J. W. Perry, N. F. Scherer, A. H. Zewail,
Picosecond pump probe multiphoton ionization of isolated molecules - IVR and coherence,
Chem. Phys. Lett. **1**03, 1–8 (1983).

[59] A. Assion, M. Geisler, J. Helbing, V. V. Seyfried, T. Baumert,
Femtosecond pump-probe photoelectron spectroscopy: Mapping of vibrational wave-packet motion,
Phys. Rev. A **5**4, R4605–R4608 (1996).

[60] S. Grafe, D. Scheidel, V. Engel, N. E. Henriksen, K. B. Moller,
Approaches to wave packet imaging using femtosecond ionization spectroscopy,
J. Phys. Chem. A **1**08, 8954–8960 (2004).

[61] J. J. Sakurai,
Modern Quantum Mechanics,
Addison Wesley, New York, 1985.

[62] C. Cohen-Tannoudji, B. Diu, F. Laloe,
Quantummechanics,
Walter de Gruyter, New York, 1997.

[63] A. Stolow
Femtosecond Time-Resolved Photoelectron Spectroscopy of Polyatomic Molecules,
Annu. Rev. Phys. Chem. **5**4, 89–119 (2003).

[64] S. A. Rice
New ideas for guiding the evolution of a quantum system,
Science **2**58, 412–413 (1992).

[65] T. Baumert, and G. Gerber,

Fundamental interaction of molecules (Na$_2$, Na$_3$) with intense femtosecond laser pulses,
Isr. J. Chem. **3**4, 103-114 (1994).

[66] M. Dantus,M. J. Rosker and A. H. Zewail,
Real-time femtosecond probing of transition-states in chemical reactions 1,
Chem. Phys. **8**7, 2395–2397 (1987).

[67] J. L. Herek, A. Mateny and A. H. Zewail,
Femtosecond control of an elementary unimolecular reaction from the transition-state region,
Chem. Phys. Lett. **2**28, 15–25 (1994).

[68] D. J. Tannor and S. A. Rice,
Control of selectivity of chemical reaction via control of wavepacket evolution,
J. Chem. Phys. **8**3, 5013–5018 (1985).

[69] D. J. Tannor, R. Kosloff and S. A. Rice,
Coherent pulse sequence induced control of selectivity of reactions: Exact quantum mechanical calculations,
J. Chem. Phys. **8**5, 5805–5820 (1986).

[70] P. Brumer and M. Shapiro,
Control of Unimolecular Reactions Using Coherent Light,
Chem. Phys. Lett. **126**, 541–564 (1986).

[71] M. Shapiro, J. W. Hepburn, and P. Brumer,
Simplified Laser Control of Unimolecular Reactions: Simultaneous (ω_1, ω_3) Excitation,
Chem. Phys. Lett. **149**, 451–454 (1988).

[72] M. Shapiro and P. Brumer,
Coherent Chemistry: Controlling Chemical Reactions with Lasers,
Acc. Chem. Res. **22**, 407–413 (1989).

[73] Chen Ce and D. S. Elliott,
Measurements of optical-phase variations using interfering multiphoton ionization processes,
Phys. Rev. Lett. **6**5, 1737–1740 (1990).

[74] Chen Ce, Yi-Yian Yin, and D. Elliott,
Interference between optical transitions,
Phys. Rev. Lett. **6**4, 507–510 (1990).

[75] A. D. Bandrauk, J. M. Gauthier, and J. F. McCann,
Laser control of predissociation by (2 + 4)-photon interference,
Chem. Phys. Lett. **2**00, 399–405 (1992).

[76] E. Charron, A. Giusti-Suzor, and F. H. Mies,
2-color coherent control of H_2^+ Photodissociation in intense laser fields,
Phys. Rev. Lett. **7**1, 692–695 (1993).

[77] L. C. Zhu, V. Kleiman,X. N. Li,S-P Lu, K. Trentelman, R. J. Gordon,
Coherent laser control of the product distribution obtained in the photoexcitation of HI,
Science **2**70, 77–80 (1995).

[78] L. Zhu, J. Fiss, K. Suto, R. Wada, T. Seideman, R. J. Gordon,
Effect of resonances on the coherent control of the photoionization and photodissociation of HI and DI,

Phys. Rev. Lett. **79**, 4108–4111 (1997)

[79] T. Nakajima and P. Lambropoulos,
Manipulation of the line-shape and final products of autoionization through the phase of the electric-fields,
Phys. Rev. Lett. **70**, 1081–1084 (1993).

[80] E. Dupont, P. B. Corkum, Liu Hu, M. Buchanan, and Z. R. Wasilewski,
Phase-controlled currents in semiconductors,
Phys. Rev. Lett. **7**4, 3596–3599 (1995).

[81] B. Sheehy, B. Walker, and L. F. DiMauro,
Phase-control in the 2-color photodissociation of HD+,
Phys. Rev. Lett. **7**4, 4799–4802 (1995).

[82] S. Cavalieri, R. Eramo and L. Fini,
Phase-controlled quantum interference in two-color atomic photoionization,
Phys. Rev. A **55**, 2941–2944 (1997).

[83] D. Xenakis, N. E. Karapanagioti, C. Fotakis, and D. Charalambidis,
Control of third harmonic generation through the phase of an additional third harmonic field,
Opt. Commun. **152**,83–88 (1998).

[84] E. Papastathopoulos, D. Xenakis, D. Charalambidis,
Phase-sensitive ionization through multiphoton-excitation schemes involving even numbers of photons,
Phys. Rev. A **59**, 4840–4842 (1999).

[85] D. Meshulach and Y. Silberberg,
Coherent quantum control of two-photon transitions by a femtosecond laser pulse,
Nature **396**, 239–242 (1998).

[86] D. Meshulach and Y. Silberberg,
Coherent quantum control of multiphoton transitions by shaped ultrashort optical pulses,
Phys. Rev A **60**, 1287–1292 (1999).

[87] N. Dudovich, B. Dayan, S. Faeder, Y. Silberberg,
Transform-limited pulses are not optimal for resonant multiphoton transitions,
Phys. Rev. Lett. **86**, 47–50 (2001).

[88] P. Lacovara, L. Esterowitz und M. Kokta,
Growth, Spectroscopy and Lasing of Titanium-doped Sapphire,
IEEE J.of Quant. Elect. QE **21**, 1614–1618 (1985).

[89] P.F. Moulton,
Spectroscopic and laser characteristics of Ti-Al2O3,
J. Opt. Soc. Am. B- Optical Physics **3**, 125–133 (1986).

[90] T. Brabec, C. Spielmann, P. E. Curley and F. Krausz
Kerr lens mode locking,
Opt. Lett **17**, 1292–1294 (1992).

[91] D. Strickland und G. Mourou
Compression of amplified chirped optical pulses,
Opt. Commun. **56**, 219–221 (1985).

[92] P. Maine, D. Strickland, P. Bado, M. Pessot und G. Mourou
Generation of Ultrahigh Peak Power Pulses by Chirped Pulse Amplification,
IEEE J. Quantum Electron. **2**4, 398–403 (1988).

[93] A. Assion,
Femtosekunden-zeitaufgelöste Untersuchungen molekularer Dynamik in schwachen und starken Laserfeldern,
Dissertation, Universität Würzburg (1998).

[94] C. P. J. Barty, G. Korn, F. Raksi, C. Rose-Petruck, J. Squier, A. C. Tien, K. R. Wilson, V. V. Yakovlev und K. Yamakawa
Regenerative pulse shaping and amplification of ultrabroadband optical pulses,
Opt. Lett. **21**, 219–221 (1996)

[95] R. L. Sutherland
Handbook of Nonlinear Optics, volume 52 of Optical Engineering,
Marcel Dekker Inc., New York, 1st edition, (1996).

[96] R. W. Boyd
Nonlinear Optics,
Academic Press, San Diego, 1st edition, (1992).

[97] J.A. Armstrong, N. Bloembergen, J. Ducuing und P.S. Pershan,
Interactions between Light Waves in a Nonlinear Dielectric,
Phys. Rev. **127**, 1918–1939 (1962)

[98] A. Yariv und P. Yeh
Optical Waves in Crystals,
Wiley and Sons, New York, (1984).

[99] C. Froehly, B. Colombeau, and M. Vampouille,
Progress in Optics XX,
E. Wolf ed., North-Holland, Amsterdam, (1983).

[100] J. Heritage, R. Thurston, W. Tomlinson, and A. Weiner,
Spectral Windowing of Frequency-Modulated Optical Pulses in a Grating Compressor,
Appl. Phys. Lett. **47**, 87–89 (1985).

[101] A. Weiner, J. Heritage, and E. Kirschner,
High Resolution Femto-Second Pulse Shaping,
J. Opt. Soc. Am. B **5**, 1563–1572 (1988).

[102] T. Brixner,
Kohärente Kontrolle von Photodissoziationsreaktionen mit optimal geformten ultrakurzen Laserpulsen,
Diplomarbeit, Universität Würzburg (1998).

[103] V. Seyfried,
Beobachtung und Kontrolle molekularer Dynamik durch Femtosekundenlaserpulse,
Dissertation, Universität Würzburg (1998).

[104] I. Z. Kozma, P. Baum, S. Lochbrunner, E. Riedle,
Widely tunable sub-30 fs ultraviolet pulses by chirped sum frequency mixing,
Opt. Express **1**1, 3110–3115 (2003).

[105] P. Nürnberger,
Formung und Charakterisierung von Femtosekunden-Laserimpulsen im Ultravioletten,

Diplomarbeit, Universität Würzburg (2004).

[106] D. J. Kane and R. Trebino,
Single-Shot Measurement of the Intensity and Phase of an Arbitrary Ultrashort Pulse by Using Frequency-Resolved Optical Gating,
Optics Letters **18**, 823–825 (1993).

[107] R. Trebino, K. DeLong, D. Fittinghoff, J. Sweetser, M. Krumbugel, and B. Richman,
Measuring Ultrashort Laser Pulses in the Time-Frequency Domain Using Frequency-Resolved Optical Gating,
Rev. Sci. Instrum. **6**8, 3277–825 (1997).

[108] J. C. Diels and W. Rudolph,
Ultrashort Laser Pulse Phenomena,
Academic Press, San Diego, (1996).

[109] J. Diels, J. Fontaine, I. McMichael, and S. Simoni,
Control and Measurement of Ultra-short Pulse Shapes (in Amplitude and Phase) with Femtosecond Accuracy,
Appl. Opt. **2**4, 1270–1282 (1985).

[110] J. Fienup,
Phase Retrieval Algorithms: A Comparison,
Appl. Opt. **2**1, 2758–2769 (1982).

[111] K. W. DeLong und R. Trebino
Improved ultrashort pulse-retrieval algorithm for frequency-resolved optical gating,
J. Opt. Soc. Am. A **11**, 2429–2437 (1994).

[112] A. Levi and H. Stark,
Image Recovery: Theory and Applications,
H. Stark ed., Academic, San Diego, Calif., (1987), pp. 277–320.

[113] M. R. Fettermann, D. Goswami, D. Keusters, W. Yang, J.-K. Rhee, and W. S. Warren,
Ultrafast Pulse Shaping: Amplification and Characterization,
Optics Express **3**, 366–375 (1998).

[114] W. C. Wiley and I. H. McLaren,
Time-of-flight mass spectrometer with improved resolution,
Rev. Sci. Instr. **26**, 1150–1157 (1955).

[115] U. Boesl, R. Weinkauf, and E.W. Schlag,
Reflectron time-of-flight mass-spectrometry and laser excitation for the analysis of neutral, ionized molecules and secondary fragments,
Int. J. Mass. Spectrom. Ion Processes **112**, 121–166 (1992).

[116] B. A. Mamyrin, V. I. Karatev, D. V. Shmikk, and V. A. Zagulin,
Mass-Reflectron a new non magnetic time-of-flight high-resolution mass-spectrometer,
Zhurnal Eksperimentalnoi i teoreticheskoi Fiziki **6**4, 82–89 (1973).

[117] B. A. Mamyrin,
Laser assisted reflectron time-of-flight mass-spectrometry,
Int. J. Mass Spectrom. Ion Processes **131**, 1–19 (1994).

[118] B. Kiefer,
Femtosekunden-Experimente an $Fe(CO)_5$ in der Gasphase
Diplomarbeit, Universität Würzburg, Physikalisches Institut (1997).

[119] P. Kruit, F. H. Read,
Magnetic field paralleliser for 2π electronspectrometer and electron image magnifier,
J. Phys. E: Sci. Instrum. **16**, 313–324 (1983).

[120] O. Cheshnovsky, R. E. Smalley,
Magnetic time of flight photoelectron spectrometer for mass-selected negative cluster ions,
Rev. Sci. Intrum. **58**, 2131–2137 (1987).

[121] M. J. Nandor, M. A. Walker and L. D. Van Woerkom
Angular distributions of high-intensity ATI and the onset of the plateau,
J. Phys. B **31**, 4617–4629 (1998).

[122] V. Schyja, T. Lang, and H. Helm,
Channel switching in above-threshold ionization of xenon,
Phys. Rev. A **57**, 3692-3697 (1998)

[123] C.E. Moore.
Atomic Energy Levels,
U. S. National Bureau of Standards Circular No. 467, (1949).

[124] G. Scoles,
Atomic and molecular beam methods,
Oxford Univ. Press, New York (1988).

[125] D. R. Herschbach,
Molecular Dynamics of Elementary Chemical Reactions (Nobel Lecture)
Anfew. Chem. Int. Ed. Engl. **26**, 1221–1243 (1987).

[126] Y. T. Lee,
Molecular-beam studies of elementary chemical processes,
Science **236** 793–798 (1987).

[127] J. C. Polanyi,
Some concepts in reaction dynamics,
Science **236** 680–690 (1987).

[128] W. Demtröder and H. J. Foth,
Molekülspektroskopie in kalten Düsenstrahlen,
Phys. Bl. **43**, 7 (1987).

[129] D. R. Miller
Free Jet Sources. In: Atomic and Molecular Beam Methods
Oxford Univ. Press, New York, (1988)

[130] R. S. Judson and H. Rabitz,
Teaching Lasers to Control Molecules,
Phys. Rev. Lett. **68**, 1500–1503 (1992).

[131] T. Baumert, T. Brixner, V. Seyfried, M. Strehle, G. Gerber
Femtosecond pulse shaping by an evolutionary algorithm with feedback,
App. Phys. B **65**, 779–782 (1997).

[132] T. Brixner, A. Oehrlein, M. Strehle and G. Gerber
Feedback-controlled femtosecond pulse shaping,
App. Phys. B **70**, S119–S124 (2000).

[133] I. Rechenberg

Evolutionsstrategie,
Friedrich Frommann Verlag, Stuttgart, (1973).

[134] H. P. Schwefel,
Numerische Optimierung von Computer-Modellen mittels Evolutionsstrategien,
Birkhäuser Verlag, Basel, (1977).

[135] H. P. Schwefel,
Evolution and optimum seeking,
Wiley, New York, (1995).

[136] I. S. Aleksakhin, I. P. Zapesochny, and V. V. Suran,
Double multiphoton ionization of strontium atom,
JETP Lett. **26**, 11–13 (1977).

[137] A. L'Huillier, L. A. Lompre, G. Mainfray, and C. Manus,
Multiply Charged Ions Formed by Multiphoton Absorption Processes in the Continuum,
Phys. Rev. Lett. **48**, 1814-1817 (1982).

[138] T. S. Luk, H. Pummer, K. Boyer, M. Shahidi, H. Egger, and C. K. Rhodes,
*Anomalous Collision-Free Multiple Ionization of Atoms with Intense Picosecond Ultra-
violet Radiation,*
Phys. Rev. Lett. **51**, 110-113 (1983).

[139] D. Feldmann and K. H. Welge,
*Two- and three-photon resonant ionisation of strontium: energy and angular distribution
of the electrons,*
J. Phys. B: At. Mol. Phys. **15**, 1651–1662 (1982).

[140] D. Feldmann, J Krautwald, S L Chin, A von Hellfeld and K H Welge,
Multiphoton ionisation of strontium creating Sr^+ and Sr^{2+},
J. Phys. B: At. Mol. Phys. **15**, 1663–1670 (1982).

[141] P Agostini and G Petite,
Multiphoton ionisation of calcium with picosecond pulses,
J. Phys. B: At. Mol. Phys. **17**, L811–L816 (1984).

[142] L. F. DiMauro, D. Kim, M. W. Courtney, and M. Anselment,
Nonresonant multiphoton ionization of calcium atoms in an intense laser field,
Phys. Rev. A **3**8, 2338–2346 (1988).

[143] Dalwoo Kim, S. Fournier, M. Saeed, and L. F. DiMauro
Magnesium atoms in an intense nonresonant laser field,
Phys. Rev. A **4**1, 4966-4973 (1990).

[144] P. Lambropoulos, X. Tang, P. Agostini, G. Petite, and A. L'Huillier
Multiphoton spectroscopy of doubly excited, bound, and autoionizing states of strontium,
Phys. Rev. A **3**8, 6165-6179 (1988).

[145] S. L. Chin, K. X. He, F. Yergeau,
1st *reported observation of multiply charged ions of alkaline atoms by multiphoton ion-
ization,*
J. Opt. Soc. Am. B **1**, 505–505 (1984).

[146] N. B. Delone, V. V. Suran, B. A. Zon,
Multiphoton ionization of atoms,
S. L. Chin, P. Lambropoulos, Academic Press, Orlando (1984).

[147] D. N. Fittinghoff, P. R. Bolton, B. Chang and K. C. Kulander,
      Observation of nonsequential double ionization of helium with optical Tunneling,
      Phys. Rev. Lett. **69**, 2642–2645 (1992).

[148] B. Walker, B. Sheehy, L. F. DiMauro, P. Agostini, K. J. Schafer and K. C. Kulander,
      Precision measurement of strong field double ionization of helium,
      Phys. Rev. Lett. **73**, 1227–1230 (1994).

[149] J. Ullrich, R. Moshammer, R. Drner, O. Jagutzki, V. Mergel, H. Schmidt-Bcking and L.
      Spielberger
      Recoil-ion momentum spectroscopy,
      J. Phys. B: At. Mol. Opt. Phys. **30**, 2917–2974 (1997).

[150] J. Ullrich, R. Moshammer, A. Dorn, R. Drner, L. Ph. H. Schmidt and H. Schmidt-Bcking
      Recoil-ion and electron momentum spectroscopy: reaction-microscopes
      Rep. Prog. Phys. **66** 1463–1545 (2003).

[151] Th. Weber, H. Giessen, M. Weckenbrock, G. Urbasch, A. Staudte, L. Spielberger, O.
      Jagutzki, V. Mergel, M. Vollmer and R. Dörner
      Correlated electron emission in multiphoton double ionization,
      Nature **405**, 658–661 (2000).

[152] E. Luc-Koenig, A. Bolovinos, M. Aymar, S. Assimopoulos, A. Jimoyiannis and P. Tsek-
      eris
      $3dnl - J = 3(E)$ *Autoionizing levels of calcium - observation by laser optogelvanic spec-
      troscopy and theoretical analysis,*
      Z. Phys. D **32**, 49–59 (1994).

[153] M. Sukharev, E. Charron, and A. Suzor-Weiner,
      Phys. Rev. A **66**, 053407 (2002) .

[154] R. A. Mathies, C. H. Brito Cruz, T. W. Pollard, and C. V. Shank,
      *Direct observation of the femtosecond excited-state cis-trans isomerization in Bacteri-
      orhodopsin,*
      Science **2**40, 777–779 (1988).

[155] M. C. Nuss, W. Zinth, W. Kaiser, E. Kölling, and D. Oesterhelt
      *Femtosecond spectroscopy of the first events of the photochemical cycle in bacteri-
      orhodopsin,*
      Chem. Phys. Lett. **1**17, 1–7 (1985).

[156] P. Hamm, M. Zurek, T. Rschinger, H. Patzelt, D. Oesterhelt, and W. Zinth,
      *Femtosecond spectroscopy of the photoisomerisation of the protonated Schiff base of all-
      trans retinal,*
      Chem. Phys. Lett. **263**, 613–621 (1996).

[157] G. Schneider, R. Diller, and M. Stockburger,
      *Photochemical quantum yield of bacteriorhodopsin from resonance raman-scattering as a
      probe for photolysis,*
      Chem. Phys. **131**, 17–29 (1989).

[158] L. Song, M.A. El-Sayed, and J.K. Lanyi,
      *Protein catalysis of the retinal subpicosecond photoisomerization in the primary process
      of bacteriorhodopsin photosyntheis,*
      Science **261**, 891–894 (1993).

[159] T. Kobayashi, K. Yokota, S. Nagakura
Photoelectron Spectra of the cis− and trans−Isomers of Some Ethylene Derivatives,
Bull. Chem. Soc. Japan **48**, 412–415 (1975).

[160] M. Takahashi, K. Kimura,
ZEKE Photoelectron Spectra of trans−Stilbene in the S_1 State,
J. Phys. Chem. **99**, 1628–1632 (1995).

[161] J. M. Smith, J. L. Knee,
Threshold ionization spectroscopy of the low frequency vibrational modes of styrene and trans−stilbene cations,
Laser Chem. **14**, 131–141 (1994).

[162] P. Felker, A. H. Zewail,
Rates of Photoisomerization of trans−strilbene in isolated and solvated molecules - Experiments of the deuterium-isotope effect and RRKM behavior,
J. Phys. Chem. **89**, 5402–5411 (1985).

[163] G. Orlandi, W. Siebrand,
Model for direct Photoisomerization of Stilbene,
Chem. Phys. Lett. **30**, 352–354 (1975).

[164] P. Tavan, K. Schulten,
Phantom photo-chemical singlet-state of stilbene and its diphenylpolyene relative,
Chem. Phys. Lett **56**, 200–204 (1978).

[165] J. Quenneville, T. J. Martínez,
Ab initio study of cis-trans photoisomerization in stilbene and ethylene,
J. Phys. Chem. A **107**, 829–837 (2003).

[166] J.A. Syage, P. M. Felker, A. H. Zewail,
Picosecond dynamics and photoisomerization of stilbene in supersonic beams .II. Reaction rates and potential energy surface,
J. Chem. Phys. **81**, 4706–4723 (1984).

[167] J. S. Baskin, L. Banares, S. Pedersen, A. H. Zewail,
Femtosecond real-time probing of reactions .20. Dynamics of twisting, alignment, and IVR in the trans-stilbene isomerization reaction ,
J. Phys. Chem. **100**, 11920–11933 (1996).

[168] B. I. Greene, R. M. Hochstrasser and R. B. Weissmann,
Picosecond dynamics of the photoisomerization of trans−stilbene under collision-free conditions,
J. Chem. Phys. **71**, 544–545 (1979).

[169] B. I. Greene, R. C. Farrow,
Subpicosecond time resolved multiphoton ionization - Excited state dynamics of cis−stilbene under collision-free conditions,
J. Chem. Phys. **78**, 3336–3338 (1983).

[170] H. Petek, K. Yoshihara, Y. Fujiwara, L. Zhe,J. H. Penn, J. H. Frederick,
Is the nonradiative decay of S_1 cis−-stilbene due to the dihydrophenanthrene isomerization channel - Suggestive evidence from photophysical measurements on $1, 2 − diphenylcycloalkenes,$
J. Phys. Chem. **94**, 7539–7543 (1990).

[171] J. Frederick, Y. Fujiwara, J. Penn, K. Yoshihara and H. Petek,
Models for stilbene photoisomerization: Experimental and theoretical studies of the excited-state dynamics of $1, 2 - diphanylcycloalkenes$,
J. Phys. Chem. **9**5, 2845–2858 (1991).

[172] J. A. Syage, P. M. Felker, A. H. Zewail,
Picosecond dynamics and photoisomerization of stilbene in supersonic beams. I. Spectra and mode assignments,
J. Chem. Phys. **81**, 4685–4705 (1984).

[173] T. Takeuchi, T. Tahara,
Vibrational coherence of S_1 $trans-stilbene$ in solution observed by 40-fs-resolved absorption spectroscopy: comparison of the low-frequency vibration appearing in the frequency-domain and time-domain spectroscopies,
Chem. Phys. Lett **326**, 430–438 (2000).

[174] S. P. Kwasniewski, L. Claes, J.–P. François, M. S. Deleuze,
High level theoretical study of the structure and rotational barriers of trans-stilbene,
J. Chem. Phys. **118**, 7823–7836 (2003).

[175] L. Gagliardi, G. Orlandi, V. Molina, P. Å. Malmqvist, B. Roos,
Theoretical study of the lowest B-1(U) states of trans-stilbene,
J. Phys. Chem. A **106**, 7355–7361 (2002).

[176] J. Bernstein,
Spectroscopic evidence for existence of multiple transitions in low-energy absorption-band of $trans-stilbene$,
Spectrochim Acta **29**A, 147–149 (1973).

[177] A. Yogev, L. Margulies,
Polarized absorption and emission-spectra of $4, 4'-dimethylstilbene$,
Israel J. Chem. Phys. **16**, 258–263 (1977).

[178] G. Hohlneicher, R. Wrzal, D. Lenoir, R. Franck,
Two-photon spectra of stiff stilbenes: A contribution to the assignment of the low lying electronically excited states of the stilbene system ,
J. Phys. Chem. A **103**, 8969–8975 (1999).

[179] R. Improta, F. Santoro, C. Dietl, E. Papastathopoulos and G. Gerber,
Time dependent DFT investigation on the two lowest B-1(u) states of the trans isomer of stilbene and stiff-stilbenes,
Chem. Phys. Lett **387**, 509–516 (2004).

[180] A. Peluso, F. Santoro, G. Del Re,
Vibronic coupling in electronic transitions with significant Duschinsky effect,
Int. J. Quantum Chem. **63**, 233–244 (1997).

[181] B. Soep, J.M. Mestdagh, S. Sorgues, J.P. Visticot
Femtosecond to nanosecond relaxation time scales in electronically excited tetrakis(dimethylamino)ethylene: identification of the intermediates,
Eur. Phys. J. D **14**, 191-203 (2001).

[182] R.L.Pruett, J.T. Barr, K.E. Rapp, C.T. Bahner, J.D. Gibson, R.H. Lafferty Jr.
Reactions of polyfluoro olefins. II. Reactions with primary and secondary amines,
J. Am Chem. Soc. **72**, 3646-3650 (1950).

[183] P.W. Stephens, D. Cox, J.W. Lauher, L. Mihaly, J.B. Wiley, P.M. Allemand, A. Hirsch, K. Holczer, Q. Li, J.D. Thompson, F. Wudl
Lattice structure of the fullerene ferromagnet TDAEC60,
Nature **3**55, 331-332 (1992).

[184] B. Narymbetov, A. Omerzu, V.V. Kabanov, M. Tokumoto, H. Kobayashi, D. Mihailovic
Origin of ferromagnetic exchange interactions in a fullerene organic compound,
Nature **407**, 883-885 (2000).

[185] Y. Nakato, M. Ozaki, H. Tsubomura
Ionization energies and Rydberg states of tetraaminoethylenes,
Bull. Chem. Soc. Jap. **45**, 1299-1305 (1972).

[186] H. E. Winberg, J. R. Downing, D. D. Coffman
The chemiluminescence of tetrakis(dimethylamino)ethylene,
J. Am. Chem. Soc. **87**, 2054-2055 (1965).

[187] M. Hori, K. Kimura, H. Tsubomura
The electronic spectrum and the chemiluminescence of tetrakis(dimethylamino)ethylene (TDAE),
Spectrochim. Acta A **2**4, 13971404 (1968).

[188] S. D. Ittel, L. K. Johnson and M. Brookhart
Late-metal catalysts for ethylene homo- and copolymerization,
Chem. Rev. **100**, 1169–1203 (2000).

[189] K. Whiteley, T. G. Heggs, H. Koch, R. L. Mawer, W. Immel,
"Polyolefins" in Ullmann's Encyclopedia of Industrial Chemistry, 6th Edt.,
Wiley-VCH, (2000).

[190] L. L. Böhm
Katalysatoren, Verfahren und Produkte: Entscheidende Elemente jeder Polyolefin-Technologie,
DECHEMA e. V., Hg., DECHEMA-Jahrestagungen'95, Kurzfassungen, Band III, (1995).

[191] A. Behr,
"Ziegler Processes" in Ullmann's Encyclopedia of Industrial Chemistry, 6th Edt,
Wiley-VCH, (2000).

[192] W. Kaminsky,
"Metallocenes" in Ullmann's Encyclopedia of Industrial Chemistry, 6th Edt,
Wiley-VCH, (2000).

[193] A. E. Hamielec, J. P. B. Soares,
Polymer Reaction Engineering - Metallocene Catalysts,
Prog. Polym. Sci. **2**1, 651–706 (1996).

[194] J. P. B. Soares, A. E. Hamielec,
Metallocene/Alumoxane Catalysts for Olefin Polymerization. A Review,
Polymer Reaction Engineering 3, **2**, 131–200 (1995).

[195] N. H. Damrauer, C. Dietl, G. Krampert, S. H. Lee, K. H. Jung and G. Gerber,
Control of bond-selective photochemistry in CH_2BrCl using adaptive femtosecond pulse shaping,
Eur. Phys. J. D **2**0, 71–76 (2002).

[196] L. Resconi, L. Cavallo, A. Fait, F. Piemontesi,
       Selectivity in Propene Polymerization with Metallocene Catalysts,
       Chem. Rev. **1**00, 1253–1345 (2000).

[197] J. Huang, G. L. Rempel,
       *Ziegler-Natta Catalysts for Olefin Polymerization: Mechanistic Insights from Metallocene
       Systems,*
       Prog. Polym. Sci. **2**0, 459–526 (1995).

Acknowledgements

Curriculum vitae

Persönliche Daten

Name:	Evangelos M. Papastathopoulos
Wohnort:	Hauptstr. 1a, 97218 Gerbrunn
geboren am:	06. Dezember 1977 in Athen
Staatsangehörigkeit:	griechisch
Familienstand:	ledig

Schulausbildung

09.1987 – 07.1990	33 Grundschule in Pireaeus
09.1990 – 07.1993	9 Gymnasium in Pireaeus
09.1993 – 07.1995	Zannio'sches Experimentelles Lyzeum

Studium der Physik

09.1995 – 09.1999	Universität Kreta, Heraklion Kreta, Griechenland, **B.S. in Physik (Ptyhion)**
09.1999 – 09.2001	Universität Kreta - F.O.R.T.H Institut Heraklion Kreta, Griechenland, **Master in Physik** Fachbereich: Laserphysik Diplomarbeitstitel : *Phase control experiments utilizing the second harmonic laser field*
seit 09.2001	Bayerische Julius-Maximilians-Universität Würzburg Promotion bei Prof. Dr. G. Gerber

Berufsweg

seit 01/2001	wissenschaftlicher Mitarbeiter der Universität Würzburg

Würzburg, den 17. Januar 2005

Evangelos Papastathopoulos